UNIVERSIDADE ESTADUAL DE CAMPINAS
Instituto de Física Gleb Wataghin

ISADORA NEME RIBEIRO

Exploring Superconductivity via Magnetic Resonance

Explorando Supercondutividade via Ressonância Magnética

CAMPINAS
2025

ISADORA NEME RIBEIRO

Exploring Superconductivity via Magnetic Resonance

Explorando Supercondutividade via Ressonância Magnética

Thesis presented to the Gleb Wataghin Institute of Physics of the University of Campinas in partial fulfillment of the requirements for the degree of MASTER OF PHYSICS, in the area of PHYSICS.

Tese apresentada ao Instituto de Física Gleb Wataghin da Universidade Estadual de Campinas como parte dos requisitos exigidos para a obtenção do título de MESTRA EM FÍSICA, na Área de FÍSICA.

Orientador: RICARDO RODRIGUES URBANO

ESTE TRABALHO CORRESPONDE À VERSÃO FINAL DA TESE DEFENDIDA PELA ALUNA ISADORA NEME RIBEIRO E ORIENTADA PELO PROF. DR. RICARDO RODRIGUES URBANO.

CAMPINAS
2025

Ficha catalográfica
Universidade Estadual de Campinas (UNICAMP)
Biblioteca do Instituto de Física Gleb Wataghin
Lucimeire de Oliveira Silva da Rocha - CRB 8-9174

R354e
Ribeiro, Isadora Neme, 1998-
Exploring superconductivity via magnetic resonance / Isadora Neme Ribeiro. – Campinas, SP : [s.n.], 2025.

Orientador: Ricardo Rodrigues Urbano.
Dissertação (mestrado) – Universidade Estadual de Campinas (UNICAMP), Instituto de Física Gleb Wataghin.

1. Supercondutividade. 2. Ressonância magnética nuclear. 3. Sistemas eletrônicos fortemente correlacionados. I. Urbano, Ricardo Rodrigues, 1974-. II. Universidade Estadual de Campinas (UNICAMP). Instituto de Física Gleb Wataghin. III. Título.

Informações complementares

Título em outro idioma: Explorando supercondutividade via ressonância magnética
Palavras-chave em inglês:
Superconductivity
Nuclear magnetic resonance
Strongly correlated electron systems
Área de concentração: Física
Titulação: Mestra em Física
Banca examinadora:
Ricardo Rodrigues Urbano [Orientador]
Iakov Veniaminovitch Kopelevitch
Herculano da Silva Martinho
Data de defesa: 23-04-2025
Programa de Pós-Graduação: Física

Objetivos de Desenvolvimento Sustentável (ODS)
Não se aplica

Identificação e informações acadêmicas do(a) aluno(a)
- ORCID do autor: https://orcid.org/0009-0005-5460-9203
- Currículo Lattes do autor: http://lattes.cnpq.br/9609203612942814

- Prof. Dr. Ricardo Rodrigues Urbano (IFGW/ UNICAMP) - Presidente e Orientador

- Prof. Dr. Iakov Veniaminovitch Kopelevitch (IFGW/ UNICAMP)

- Prof. Dr. Herculano da Silva Martinho (Universidade Federal do ABC)

A ata da defesa com as respectivas assinaturas dos membros encontra-se no SIGA/Sistema de Fluxo de Dissertação/Tese e na Secretaria do Programa da Unidade.

Aos meus pais e à Dona Victória.

ACKNOWLEDGEMENTS

First of all, I would like to thank my parents, Edson and Barbara, and my brother Fred for the unconditional and essential support throughout these 2 years (and my whole life, actually). Your love, advice and encouraging words made me regain my strength every time I thought I couldn't bounce back from bad days. I will forever be grateful for your presence in my life, won't ever forget everything you did for me, and I hope this work makes you all proud of me. For my parents specifically: I know the sacrifices you pulled through my entire life, and specially after I left home. I carry it deeply in my heart and am grateful for it, and I hope I can return some of it from now on. I love you so much.

I want to specially thank my advisor, Ricardo Urbano, for the unmatched support both in my undergraduate research and my Master degree. Our discussions in Physics and your stories always pushed me to learn even more about the never-ending field of condensed-matter physics and NMR. Thank you for always believing in me, even when I couldn't. This made such a difference during undergrad and gave me the needed confidence to pursuing my dream of becoming a Physicist. I also want to thank Prof. Pascoal Pagliuso, Prof. Eduardo Granado, Prof. Cris Adriano and Prof. Carlos Rettori for their support, advice, encouraging words and conversations during coffee time. You have all inspired me a lot to continue in the path of scientific career, and I hope to be an excellent physicist just like you.

To my lab colleagues, who became such good friends throughout the years: Adriele, Ana, Davi, Denise, Derick, Fernando, Henrique, Jean, Jéssica, Laiza, Maria Helena, Natália, Otávio, Paulo, Rodolfo Carvalho, Rodolfo Tartaglia, thank you for all the coffees after lunch, all the cakes and gossip, and all the times you've helped me transfer LHe. I am so grateful and honoured to have such excellent lab friends, and I have no doubt you will have a brilliant career ahead of you. Shoutout to Davi and Paulo for the patience and help in the lab, all the valuable lessions, tips and tricks. I hope one day to be like this for my future lab mates as well.

To my friends in Unicamp: Amanda, Bruna Guissi, Flávia, Gabi Delavald, Gabriel Aguiar, Gabriel Reis, Guga, Marcos, Marina Raboni, Marina Ripper, Mayara, Pedro Pinho, Priscila, Rafael Reis, Ruela, and so many others who crossed my path since I started my undergrad studies, thank you from the bottom of my heart. Our friendship means so much to me, and you have helped me through tough times more than I can say. Thank you for all the laughs, the advise, the lending ear and for the help in difficult courses as well. I will never forget you.

A special thanks to Caique and Picolé. We got close during the Covid-19 pandemic, and you were always there for me whenever I had trouble understanding something in Physics or when I needed to vent. Your help since this period was essential for me to pursue my dream to graduate and become a physicist. I hope to, one day, know about Physics as much as both of you do. I have no doubt you will have an amazing future in whichever career you choose. Thank you for all the help in Physics, the laughs, the silly jokes and the advices.

I want to also thank the Cryogenic department, specially Milton and Gustavo, for providing the necessary LHe for NMR experiments throughout these years and in tough times. I would also like to thank Isabel for cleaning up our workspace.

Lastly, I acknowledge CAPES (Coordenação de Aperfeiçoamento de Pessoal de Nível Superior, grant 88887.822484/2023-00) and FAPESP (Fundação de Amparo à Pesquisa do Estado de São Paulo, grant 2017/10581-1) for the finantial support in this work. This study was financed in part by the Coordenação de Aperfeiçomento de Pessoal de Nível Superior - Brasil (CAPES) - Finance Code 001.

Não há caminho fechado para quem se propõe a lutar.

(Rodney William)

ABSTRACT

The main goal of the present work was to enhance my expertise in the Nuclear Magnetic Resonance (NMR) technique, especially in the field of superconductivity, and to be able to characterize two distinct types of superconductors — the BCS MgB_2 and the unconventional $BaFe_{1.91}Co_{0.09}As_2$ — both single crystalline samples. The reason for these choices was mainly because these superconductors are well known and were widely studied since their discovery.

For MgB_2 single crystals, some novel and compelling results were observed. In bulk magnetization data, the superconducting transition was observed at 36 K near zero field (25 Oe), however it was suppressed for increasing magnetic field, being undetectable for $H \geq 3$ T. There was no presence of superconducting hysteresis loop observed as well. For the Knight shift data, acquired by NMR, one observed the onset of superconductivity at ≈ 18 K, only the Knight shift increased rather than decreased below T_c. The superconducting state can also be observed by the broadening of the NMR line, from 4 kHz (60 K) to 7 kHz (4.3 K). Furthermore, from the NMR spectra in different orientations ($H \| c$ and $H \perp c$) and at 4.2 K, we could calculate the quadrupolar frequency for our sample. By comparing it to published values on both single and polycrystalline samples in the normal state, we can assume there is no significant changes in the lattice parameters of MgB_2 in the superconducting state, as expected. Moreover, from the spin-lattice relaxation rate data, two peaks were observed: one below 39 K and the other around 20 K. This is most likely a first-time observation of two Hebel-Slichter peaks by NMR in MgB_2 single crystals, associated with both superconducting gaps, σ and π.

Finally, for $BaFe_{1.91}Co_{0.09}As_2$ single crystals, we could observe typical superconducting characteristics on both magnetization and Knight shift experiments. The key aspects were the decrease in magnetization due to diamagnetic shielding (and thus the critical temperature was obtained for both zero field and 7 T), as well as the hysteresis superconducting loop in 4 K. In the NMR data, a decrease in Knight shift below T_c and a broadening of the line indicate the superconducting transition. At last, the spin-lattice relaxation rate data point to a SDW transition at 20 K (exactly where the NMR line starts to become too broad and featureless), a small dip at 18 K and then another increase at 16 K, marking the onset of superconductivity and the coexistence of SC and SDW states.

RESUMO

O principal objetivo deste trabalho foi aprimorar meu conhecimento na técnica de Ressonância Magnética Nuclear (RMN) como estudante, especialmente na área de supercondutividade, e ser capaz de caracterizar diferentes tipos de supercondutores: MgB_2 (BCS) e $BaFe_{1,91}Co_{0,09}As_2$ (não convencional), ambos em amostras monocristalinas. A escolha desses materiais se deu principalmente pelo fato de serem supercondutores bem conhecidos e amplamente estudados desde sua descoberta.

Para os monocristais de MgB_2, foram observados alguns resultados novos e interessantes. Nos dados de magnetização em volume, a transição supercondutora foi observada a 36.0(5) K em campo próximo de zero (25 Oe), sendo suprimida com o aumento do campo magnético, tornando-se indetectável para $H \geq 3$ T. Também não foi observada a presença de um loop de histerese supercondutor. Nos dados de *Knight shift*, obtidos por RMN, observou-se o início da supercondutividade por volta de 18 K, mas, ao invés de diminuir abaixo de T_c, o *Knight shift* aumentou. O estado supercondutor também pôde ser observado pelo alargamento da linha de RMN, de 4 kHz (a 60 K) para 7 kHz (a 4,3 K). Além disso, a partir dos espectros de RMN em diferentes orientações ($H \| c$ e $H \perp c$) e a 4.2 K, foi possível calcular a frequência quadrupolar da nossa amostra. Comparando-a com os valores publicados tanto para amostras monocristalinas quanto policristalinas no estado normal, podemos assumir que não há mudanças significativas nos parâmetros de rede do MgB_2 no estado supercondutor, como era esperado. Ademais, nos dados da taxa de relaxação spin-rede, foram observados dois picos: um em 35 K e outro abaixo de 18 K. Esta é, muito provavelmente, a primeira observação de dois picos de Hebel-Slichter por RMN em monocristais de MgB_2, associados aos dois gaps supercondutores, σ e π.

Por fim, para os monocristais de $BaFe_{1,91}Co_{0,09}As_2$, foi possível observar características típicas da supercondutividade tanto nos experimentos de magnetização quanto nos de *Knight shift*. Os principais aspectos foram a diminuição da magnetização devido à blindagem diamagnético (e, assim, a temperatura crítica foi obtida tanto para campo zero quanto para 7 T), bem como o ciclo de histerese supercondutor a 4 K. Nos dados de RMN, a diminuição do *Knight shift* abaixo de T_c e o alargamento da linha indicam a transição supercondutora. Por fim, os dados da taxa de relaxação spin-rede apontam para uma transição SDW a 20 K (exatamente onde a linha de RMN começa a se tornar muito larga e sem estrutura), uma leve queda a 18 K e, em seguida, um novo aumento a 16 K, marcando o início da supercondutividade e a coexistência dos estados supercondutor (SC) e de onda de densidade de spin (SDW).

LIST OF FIGURES

CONTENTS

1 INTRODUCTION

In this thesis, we have studied the physical properties of conventional and unconventional superconductors by means of solid state nuclear magnetic resonance (NMR), by measuring NMR parameters such as Knight shift and spin-lattice relaxation time, T_1. The main motivations lie in the detailed information gathered through NMR that are hardly accessed by other experimental techniques, and in my wish, as a physicist, to specialize in this technique and the subject of superconductivity. Therefore, two key materials were chosen for this study: MgB_2 and Co-doped $BaFe_2As_2$. These compounds were largely studied after they were discovered as superconductors, consequently a lot of information about their physical properties and high quality single crystals are now available. This leads to better and reliable NMR experiments results, and allows one to explore both anisotropy effects and quadrupolar interactions.

1.1 A brief Historical Background on Superconductivity

Superconductivity is a quite fascinating physical phenomenon that sparks a lot of interest in the scientific community ever since its discovery in 1911 by H. Karmelingh Onnes [1]. He observed a sharp drop in the resistivity of Hg at a critical temperature T_c when studying the conductivity of metals in lower temperatures. For this discovery, Onnes was awarded a Nobel prize in 1913. Later, in 1933, the Meissner-Ochsenfeld effect was discovered in superconductors: it is the screening of magnetic field from the interior of a superconductor during its transition as the temperature is cooled below T_c [2]. This is a key characteristic that differs superconductors from perfect conductors used in classical Electrodynamics models.

After such discoveries, phenomelogical theories were proposed to describe superconductivity: i) the London equations (1935), focused on the behaviour of electric and magnetic fields in the interior of superconductors [3], i.e., the Meissner effect, and the ii) Ginzburg-Landau theory (1950), which describes the behavior of superconducting electrons in the intermediate region between normal and superconducting domains [4]. Although successful theories, the explanation for *why* a material superconduct was achieved by the Bardeen-Cooper-Schrieffer (BCS) theory in 1957, which proposed that electrons can pair under certain conditions through electron-phonon interactions, and these Cooper pairs are the charge carriers in this case [5]. For this groundbreaking discovery, the trio of physicists were awarded the Nobel prize in 1972. These theories will be discussed in Chapter 2.

However, the questions on this topic were not closed indefinitely, as in 1979 a new class of superconductors was discovered: the so called heavy fermion compounds [6]. The superconductivity in these compounds arise from the $4f$ electrons in the rare earth metals, and their pairing mechanism is not explained by electron-phonon interaction. Moreover, in their phase diagrams, the superconductivity is always in the vicinity of an antiferromagnetic phase, which seems quite antagonic since magnetism usually opposes, or does not favour, superconductivity. The same happens for cuprate (discovered in 1986, [7][1]) and Fe-based superconductors(FeSC), discovered in 2008, [8]. One can see in Figure 1.1 the different classes of superconductors, the year they where discovered and their T_c. Another class of unconventional superconductors is the organic superconductors, first discovered in 1980 by Klaus Bechgaard and Denis Jérome in $(\mathrm{TMTSF})_2\mathrm{PF}_6$, with $T_c = 0.9$ K at an applied pressure of 12 kbar.

It is important to highlight the discovery of YBCO superconductors, shortly found after the discovery of cuprate superconductors, as its critical temperature (92 K) is above the temperature of liquid nitrogen (77 K). It then became more feasible to implement superconductors in technological applications due to the low cost production of liquid nitrogen when compared to liquid helium. Achieving superconductivity at ambient conditions would revolutionize numerous technologies, including power grids, magnetic levitation and magnetic resonance imaging (MRI), by eliminating energy losses in electrical transmission and enabling highly efficient electronic devices. Recent advances, particularly in hydrogen-rich materials under extremely high pressure, have brought scientists closer to this goal, though practical, stable, and scalable room-temperature superconductors remain a major challenge. Currently, the highest T_c for ambient pressure is for Hg-Ba-Cu-O systems, 130 K [9], whereas for extremely high pressures (170 GPa), it is 250 K for LaH_{10} [10].

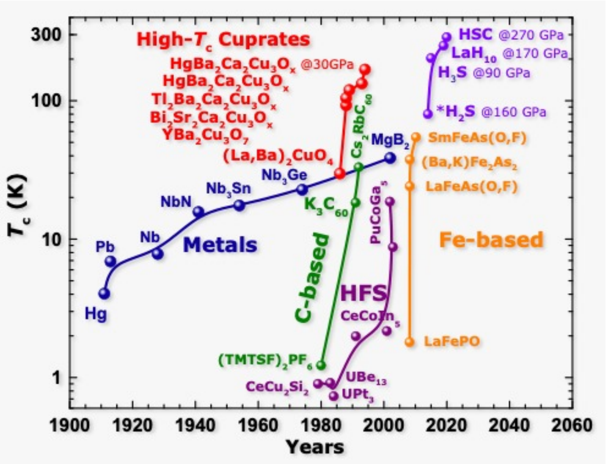

Figure 1.1: Critical temperature T_c as function of their discovery years for distinct classes of superconductors. Courtesy of Prof. Urbano.

Now, for the sake of chronological order, I will briefly outline the physics of MgB_2, whose superconducting properties were discovered in 2001 and are the subject of this thesis,

---

[1] Bednorz and Müller were awarded the Nobel prize in 1987 for their fascinating discovery.

before I further discuss the unconventional superconductivity of Fe-based superconductors, also subject of this work. Magnesium diboride is by no means an ordinary superconductor: despite being a BCS superconductor, it has two superconducting gaps. This is the first observation of two-gap superconductivity and has sparkled great interest of the scientific community at the time. Moreover, it has a T_c of 39 K, the highest among intermetallic compounds at that point, which raised questions whether it was another unconventional class of superconductors being discovered.

The evidences in favor of conventional superconductivity lies mainly on the observation of the isotope effect in these compounds: when grown with ^{10}B instead of ^{11}B, the T_c of Magnesium diboride increases by 1 K [11, 12]. This is not observed in substituting Mg isotopes, indicating that the superconductivity lies on B electronic bands. This is further supported by photoemission, scanning tunneling microscopy and neutron scattering experiments [13–15], by the form of the temperature dependency of the gap energy, consistent with the BCS theory.

Despite the initial excitement over this discovery, growing MgB_2 is no simple task. Elemental Mg has a high vapor pressure and MgB_2 decomposes rather than melts, making simple crystal growth to be near unmanageable. A way to avoid this is reacting B with Mg vapor at around 900° to produce powder samples [16]. Nonetheless, probing powder samples through nuclear magnetic resonance yields the following problem: for samples as anisotropic as MgB_2, the random orientation of the powder in regards to the magnetic field results in several NMR lines, or a very broad peak, instead of a clear, narrow resonance peak. Hence, shortly after its discovery, MgB_2 was studied by NMR, but the polycrystalline samples available soon proved themselves troublesome. Moreover, measuring and calculating spin-lattice relaxation times was complex, and only one study was able to prove the existence of the Hebel-Slichter coherence peak in MgB_2, a signature expected for BCS superconductors.

Regardless of the difficulties faced, after a while MgB_2 single crystals were finally grown using high pressure, high temperature methods [17]. This opened a door for first time studies on the anisotropic magnetic properties, as well as NMR experiments with proper alignment of the crystal with respect to the magnetic field. There is only one NMR study on MgB_2 single crystals so far. However, the authors claimed no reliable data on Knight shift were obtained in the superconducting phase. It is in light of this scenario that this study is inspired: to shed a new light onto the superconducting state of MgB_2 single crystals by using NMR, and establish a comparison with what is known for polycrystalline samples. The samples used in this thesis were grown and characterized by Prof. Dr. Raquel Ribeiro in the group of Prof. Paul Canfield from Ames Laboratory, IA.

Now, let us go back to FeSC, whose discovery in 2008 took the whole community by storm [8], given that Fe atoms are strongly magnetic, and one would expect magnetism to be antithetical to superconductivity. Moreover, the BCS theory is not sufficient to explain superconductivity in these compounds, and a large body of scientific evidences point in the

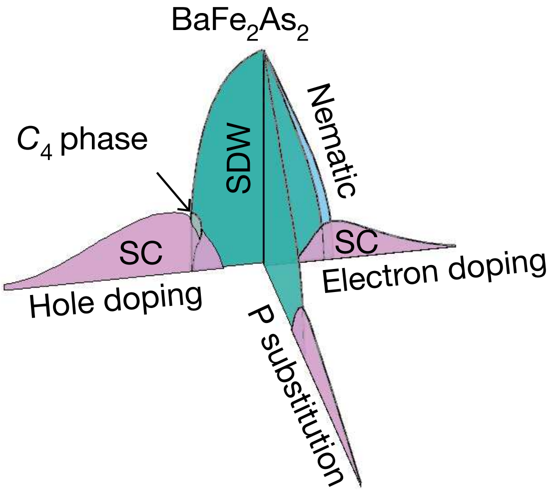

Figure 1.2: Phase diagram for $BaFe_2As_2$. Image extracted from Ref. [23].

direction of spin fluctuations playing the role of mediators in the electron pairing [18–22].

Another surprising feature of such materials is the different ways in which the presence of multiple atomic orbitals can manifest in unconventional superconductivity, giving rise to a rich landscape of gap structures that share the same dominant pairing mechanism [23]. Due to the multi-orbital character of these materials, the Hund's interaction plays the most relevant role in determining the electronic correlations in the normal state [24]. Another distinguishing feature of FeSC is the orbital differentiation: although multiple orbitals are subjected to the same interaction, they experience different degrees of correlation [25–30]. It is this correlated normal state that gives rise to superconductivity and also other electronic ordered states in these compounds.

The vast majority of family of FeSC compounds order magnetically (see example in Figure 1.2). Specifically the 122-family (for example $BaFe_2As_2$) exhibit a spin-density wave phase of stripe-type below a critical temperature of 134 K. It is the observation of magnetic fluctuations at the stripe-type wave vectors that has been widely interpreted as evidence for magnetic fluctuations playing a key role in the pairing interaction. It is by suppressing the antiferromagnetic (AFM) phase, either by applying pressure or chemical substitution, that superconductivity arises [31]. Lastly, another important aspect of the FeSC phase diagrams is a structural transition from tetragonal to orthorrombic phase at T_s, which occurs either at the same temperature or anticipating the magnetic transition.

1.2 What is the role of NMR in studying Superconductivity?

The 50's were certainly an exciting decade for condensed matter physics and the theory of superconductivity. It started off with the discovery of the isotope effect [32, 33] and the paper by Ginzburg and Landau on superconductivity [4]. Later on, the paper by Abrikosov [34] made a groundbreaking discovery on the type-II superconductors, not known until then, and the penetration of magnetic field in a very specific manner. This bypasses the difficulty imposed by the Meissner effect on superconductors, which a magnetic field is expelled from the material, allowing for the study of superconductors using techniques such as nuclear magnetic resonance (NMR). In 1957 as well, we finally have the BCS paper presenting a successful microscopic theory of superconductivity. Finally, the decade ended in 1959 with Gor'kov's work that brought together the Ginzburg-Landau and BCS theories, showing that the former is a limiting form of the latter, and that the order parameter of the GL theory ψ is proportional to the BCS energy gap parameter, Δ.

All of these discoveries and theoretical advances needed an experimental backup, and that's where NMR, among other techniques, come into the picture. Charles Slichter played a central role in NMR studies in the 50's by studying relaxation times in Al [35]. He was inspired by a talk by Bardeen in 1954 on the electron-phonon theory giving rise to an energy gap. Slichter noticed that in alkali metals, it is the electrons with energies close to the Fermi level that contribute the most to the mechanism for spin-lattice relaxation in a metal. Therefore, the presence of such a gap would produce a major effect on the temperature dependency of T_1, the longitudinal (or spin-lattice) relation time.

This was not an easy task, however. At that point, type-II superconductors have not been discovered yet and the type-I ones presented the Meissner effect: the shielding of magnetic field mitigates the polarization of spins, from which NMR information is acquired. Slichter and his student Hebel proceeded by performing a series of magnetic field cycling, where the polarization happened in the normal state. Since a sufficiently strong magnetic field suppresses superconductivity, one could start with a field intense enough to bring the sample into its normal state, allowing the nuclei to be polarized. Lowering the field to zero would then demagnetize the nuclei, reducing their spin temperature to a level much lower than the lattice temperature while restoring the sample's superconducting state. In this state, the nuclear spin temperature gradually increases toward the lattice temperature. Finally, raising the magnetic field back to a strong value would return the sample to its normal state, enabling observation of the final nuclear polarization. By analyzing the final signal's strength as a function of the time the sample remains superconducting, one could determine the spin–lattice relaxation rate in the superconducting state.

After obtaining such T_1 results, Slichter and Hebel shared them with Bardeen. They expected T_1 to be longer in the superconducting state than that at the same temperature in the normal state, because an energy gap would suppress excitations. However, they found that the relaxation rate at the lowest temperature was twice as fast as it would be at the same temperature. The only explanation was an enhancement of the density of states near the edge of the gap, which Bardeen agreed to be reasonable.

Furthermore, in 1962, the experimental observation of type-II superconductivity[2] in Nb [36] and Nb_3Sn, Nb_3Al, V_3Ga and V_3Si [37] lifted the spirits for the NMR commu-

---

[2] through the observation of negative surface energy at an interface between normal and superconducting

nity: now one can access the superconducting state by the vortex (or intermediate) state, where the magnetic flux penetrates the sample in the form of fluxoids. This regime arises when the applied magnetic field is greater than a lower critical field H_{c1} but less than an upper critical field H_{c2}. Such fluxoid lattice produces a characteristic NMR line shape: the highest frequency corresponds to nuclei closer to the vortex core. In the case of a square fluxoid lattice, the lowest frequency corresponding to nuclei in the center of the vortex core, and the absorption spectrum has the greatest intensity for nuclei between two nearest neighbour vortices (see Figure 1.3). One can use this information to also study how T_1 (longitudinal) and T_2 (transverse) relaxation times vary locally within the vortex lattice. [38].

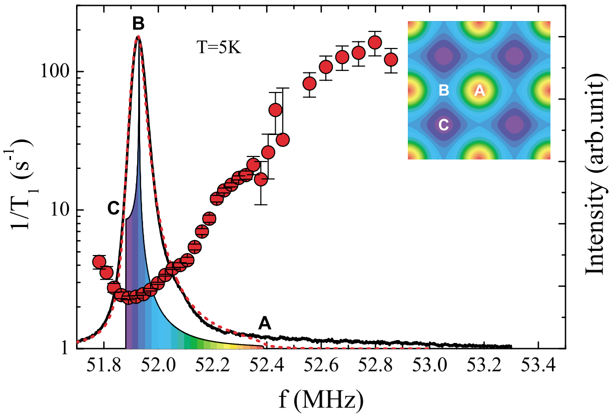

Figure 1.3: ^{205} Tl-NMR spectrum (solid line) at 5 K for $Tl_2Ba_2CuO_6$. The intensity is plotted in a linear scale. The red dotted line represents the simulation spectrum convoluted with Lorentzian broadening function. The red filled circles show the frequency dependence of T_1^{-1} at the Tl site. Inset: the image of the field distribution in the vortex square lattice; center of vortex core (A), saddle point (B), and center of vortex lattice (C). Image extracted from Ref. [39]

Therefore, the NMR resonance line in the superconducting state should then be a direct convolution of a Lorentzian line shape and the internal magnetic field distribution due to the vortex lattice. Moreover, a careful spectral analysis should provide relevant information on the superconducting state.

The Pairing State and NMR

An important information to obtain by means of NMR is the pairing state of a superconductor. For a BCS superconductor, the wave functions correspond to electron pairs of zero total spin S and zero orbital angular momentum L. Nonetheless, other pairing states are possible if there are other pairing mechanisms involved. For instance, in high-T_c cuprates, the pairing mechanism is based on spin fluctuations, and the pairing state is believed to be $S = 0, L = 2$ [40]. However, it must be noted that knowledge of the pairing state does not predict the pairing mechanism by itself.

The way NMR determines the spin state is by measuring the shift of the NMR frequency relative to that of a reference material. For weakly paramagnetic materials such as

---

metals.

metals, the polarization of the electron spins produces a shift named Knight shift, after its discoverer Walter Knight [41]. An example is illustrated in Figure 1.4a. Such shift is proportional to the spin susceptibility for one-component systems, and by measuring the Knight shift one gets information on the temperatures dependency of the spin susceptibility of the system ($K \propto \chi_s(0)$). For $S = 0$, the spin susceptibility vanishes at $T = 0$, whereas for $S = 1$, it does not [42]. An example of this is the nonvanishing spin contribution of Co and Ga shifts in $\mathrm{PuCoGa_5}$ reported by Curro et al. [43], a heavy fermion (unconventional) superconductor (Figure 1.4b).

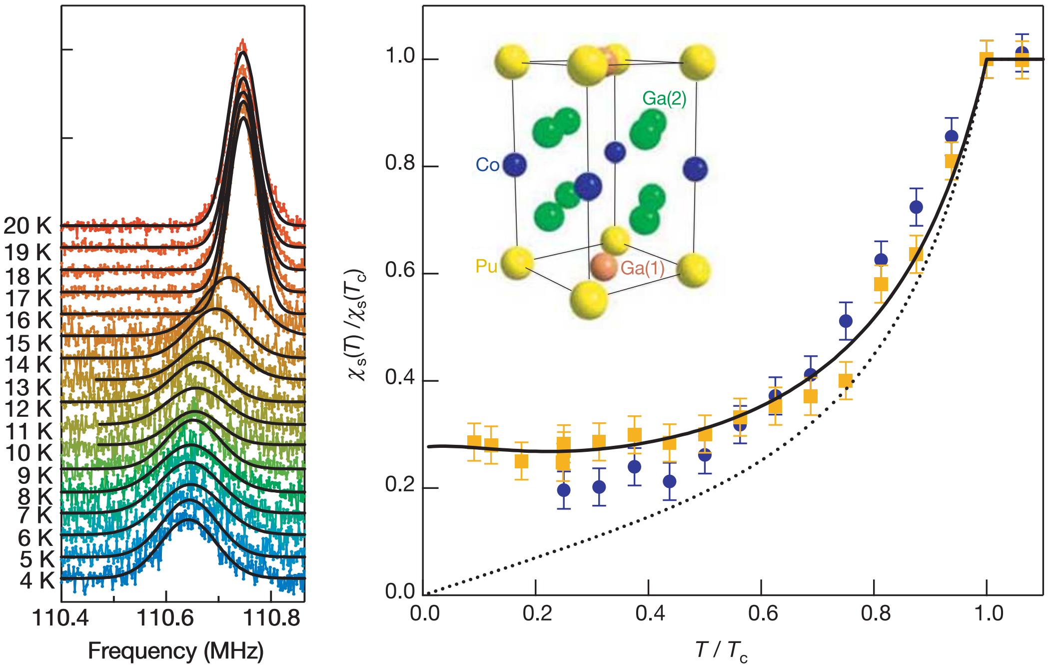

(a) (b)

Figure 1.4: a) NMR spectra of ^{71}Ga at 8 T at a series of temperatures through $T_c \approx 16$ K. The spectra have been offset vertically for clarity. Solid lines are gaussian fits. b) Normalized spin susceptibility in the superconducting state. The ^{59}Co and ^{71}Ga data, as well as the calculations for pure d-wave (dotted line) and dirty d-wave (solid line) gap functions are shown. Images extracted from Ref. [43]

Apart from the Knight shift, the spin-lattice relaxation rate further corroborates to identify the pairing state. For $L = 0$, $1/T_1$ is expected to have a coherence peak just below T_c, similar to what was reported for Al. At lower temperatures, $1/T_1$ varies exponentially as a function of $-\Delta/T$. For $L \neq 0$, no such peak is observed due to lifetime effects that broaden the electron energy levels, and one gets a power law T-dependence of $1/T_1$: typical of a d-wave is a T^3 dependence below T_c for point nodes, whereas T^5 is expected for line nodes. One can see such difference in Figure 1.5 for heavy fermion $\mathrm{PuCoGa_5}$.

In conclusion, one can see the relevance of the GL equations as well as the BCS theory, which paves the way for studying superconductivity through type-II SC. This allowed NMR physicists to join the party of extraordinary beauty of superconductivity and contribute to its advances using this powerful experimental technique.

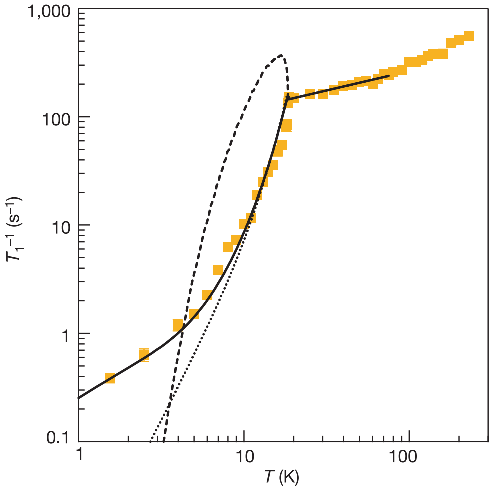

Figure 1.5: The spin-lattice relaxation rate in the normal and superconducting states, $1/T_1$ for the ^{69}Ga as well as the calculations for the BCS isotropic s-wave (dashed line), pure (dotted line) and dirty (solid line) d-wave gap functions. Image extracted from Ref. [43]

Thesis Structure

Chapter 2 presents the theory of conventional superconductivity, beginning with the general characteristics of superconductors and progressing through phenomenological models, including the London and Ginzburg-Landau theories. The chapter concludes with the BCS theory. Chapter 3 introduces the fundamentals of nuclear magnetic resonance (NMR), covering nuclear spins in a magnetic field, spin echoes, the Bloch equations and their solutions, and the principles of resonance measurement in the laboratory. Chapter 4 outlines the methodology and experimental setup, detailing the SQUID-VSM system and the NMR spectrometer. Chapter 5 presents experimental results on MgB_2, discussing the findings in the context of its two-gap superconductivity. Finally, Chapter 6 explores the experimental results of Co-doped $BaFe_2As_2$, following a brief theoretical introduction.

2 CONVENTIONAL SUPERCONDUCTIVITY

Superconductivity is a physical phenomenon with highly interesting properties. It is a state that arises in certain materials below a critical temperature T_c, which presents both perfect conductivity and perfect diamagnetism. The latter is of utmost importance, since it cannot be explained through Maxwell equations and classic Electromagnetism (explained in further detail below).

It was discovered in 1911 by H. Kamerlingh Onnes when studying the effects of low temperatures in resistivity [1]. He observed that, when the temperature was around 4 K, the resistivity of mercury (Hg) dropped abruptally to extremely low values ($R \approx 10^{-5}\Omega$). Later on, this remarkable property was observed on other metals, such as Al, Sn and Pb. Due to his ground breaking discovery, Onnes was awarded the Nobel prize in 1913.

On the other hand, the property of perfect diamagnetism was only discovered years later, in 1933, by Meissner and Ochsenfeld [2]. They observed that when a superconductor is in its normal state and a magnetic field is applied, it behaves as a paramagnet. However, once the temperature goes below T_c, there is an immediate expulsion of the magnetic field, which can now only enter the superconductor a couple of nm. This phenomenon can be seen in Figure 2.1. That effect is not explained by the Faraday's law or any other Maxwell equation, thus being a quantum effect. Furthermore, this immediate repulsion of magnetic field (the Meissner-Ochsenfeld effect) is what differs between a superconductor and the perfect conductor used as model in classic Electrodynamics.

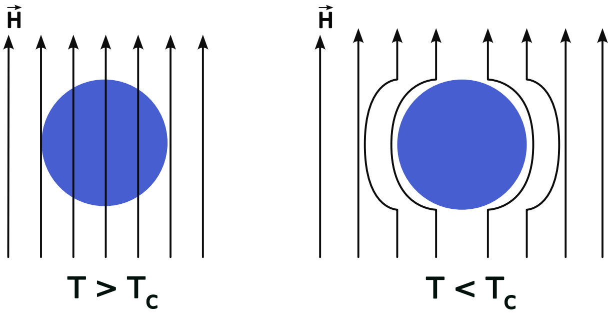

Figure 2.1: The immediate screening from the interior of the superconductor happens as soon as the superconducting transition occurs.

A quick note on the Meissner Effect

To detect experimentally the Meissner effect, one can perform magnetization experiments as a function of temperature. Two different protocols must be performed: ZFC and FC. ZFC stands for *zero field cooling*, and means that first the sample will be cooled to a low temperature (lower than T_c) in zero magnetic field. When the low temperature is achieved, the magnetic field will be turned on. Since the sample is in its superconducting state, the field will not be able to penetrate the sample (see Figure 2.2a). On the other hand, FC means *field cooling*, which means that the magnetic field will be turned on whilst the sample is in room temperature. Afterwards, the temperature will be cooled below T_c, so the material enters the superconducting state with an applied magnetic field. That means that the field, that was once inside the sample, will be immediately screened from it, as shown in Figure 2.2b. This showcases exactly how the perfect diamagnetism works: it is not only diamagnetic when you turn on the field and it is in its superconducting state, but it will expel the field that was penetrating the sample before the superconducting transition.

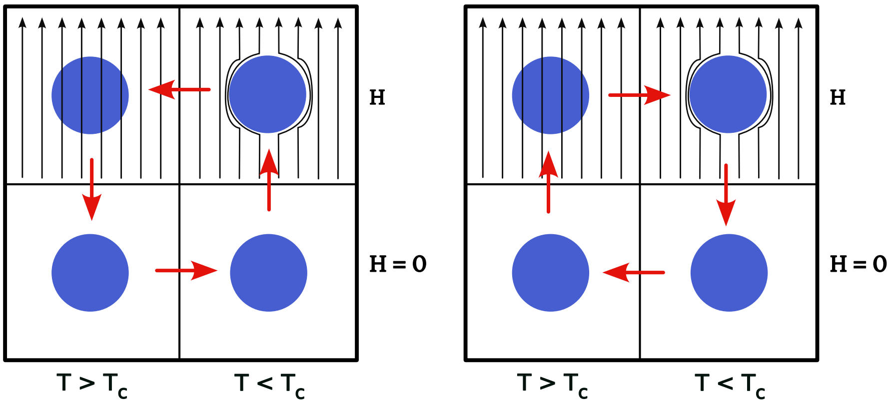

(a) (b)

Figure 2.2: Behavior of a superconductor when either a) ZFC b) or FC is performed.

The presence of the Meissner effects implies there is a **critical field** H_c, above which the superconductivity is destroyed. It is related to the free energy difference between normal and superconducting states, in field zero:

$$\frac{H_c^2(T)}{8\pi} = f_n(T) - f_s(T) = F_s(T) \tag{2.1}$$

where F$_s(T)$ is the condensation energy of the superconducting state.

Empirically, $H_c(T)$ can be approximated by a parabolic law:

$$H_c(T) \approx H_c(0)[1-(T/T_c)^2] \tag{2.2}$$

2.1 Phenomenological Theories

The following content of this chapter will be based on Reference [44].

2.1.1 The London Theory

In 1935, Fritz and Heinz London proposed a phenomenological theory on superconductivity [3]. They proposed two equations that would explain the behavior of electric and magnetic fields inside a supercondutor:

$$\boldsymbol{E} = \frac{\partial}{\partial t}(\Lambda \boldsymbol{J_s}) \tag{2.3}$$

$$\boldsymbol{h} = -c\nabla \times (\Lambda \boldsymbol{J_s}) \tag{2.4}$$

where

$$\Lambda = \frac{4\pi\lambda^2}{c^2} = \frac{m}{n_s e^2} \tag{2.5}$$

is a phenomenological parameter, λ is the penetration depth (explained below) and n_s is the density of superconducting electrons. Equation 2.3 describes a perfect conductor: the electric field accelerates the superconducting electrons, rather than simply sustaining their speed. The second London equation 2.4 can be combined to the Maxwell equation $\nabla \times h = 4\pi J/c$ to get the following result:

$$\nabla^2 \boldsymbol{h} = \frac{\boldsymbol{h}}{\lambda^2} \tag{2.6}$$

Equation 2.6 states that a magnetic field is screened from the superconductor with a penetration depth λ: therefore, it describes the Meissner effect.

A more quantum motivation for the London equations can be seen by using a vector potential $\boldsymbol{A}$, given by F. London [45]. Since the canonical momentum is given by $\boldsymbol{p} = (mv + e\boldsymbol{A}/c)$, and the net momentum is zero when the applied field is zero, one arrives at the following relation for the average velocity (in the absence of field):

$$\langle \boldsymbol{v}_s \rangle = \frac{-e\boldsymbol{A}}{mc} \tag{2.7}$$

Taking n_s as the superconducting electrons density and that their wavefunction is in a "rigid" ground state (i.e., it retains the property $\langle p \rangle = 0$), the superconducting current density is:

$$\boldsymbol{J_s} = n_s e \langle \boldsymbol{v}_s \rangle = \frac{-n_s e^2 \boldsymbol{A}}{mc} = \frac{-\boldsymbol{A}}{\Lambda c} \tag{2.8}$$

Taking the time derivative on both sides yields Equation 2.3, whereas taking the curl yields 2.4. Therefore, Equation 2.8 contains both London equations in a compact form. Note that Equation 2.8 is not gauge-invariant; it only works for a particular choice of $\boldsymbol{A}$, which is the London gauge. It satisfies the following conditions:

1. $\nabla \cdot \boldsymbol{A} = 0$;
2. the normal component of $\boldsymbol{A}$ over the surface is related to any supercurrent through the surface by 2.8;
3. $\boldsymbol{A} \to 0$ in the interior of bulk samples.

2.1.2 Ginzburg-Landau Theory

In 1950, Vitaly Ginzburg and Lev Landau took yet another step towards the theory of superconductivity. They proposed another phenomenological theory [4], this time focused on understanding the behaviour of the superconducting electrons, introducing a complex pseudowavefunction ψ as an order parameter in Landau's theory of second order phase transitions. ψ describes de superconducting electron and relates to the density of superconducting electrons by $n_s = |\psi(x)|^2$. Moreover, this wave function can be written in terms of a phase in the following manner:

$$\psi(\boldsymbol{x}) = |\psi(\boldsymbol{x})|e^{i\phi} = \sqrt{n_s}e^{i\phi} \tag{2.9}$$

Although not fully appreciated when it first came out, the GL theory soon proved to the a quite ingenious way of describing the macroscopic quantum-mechanical nature of the superconducting state, which is crucial for understanding its unique electrodynamic properties. Even though it has some limitations such as only valid near T_c (Landau's theory is valid only in the neighborhood of the transition) and neither ψ or $\boldsymbol{A}$ can vary too rapidly, it is an astonishing theory capable of dealing with spatially inhomogeneous superconductivity.

The basic postulate of the GL theory is that, if the order parameter ψ is small and varies slowly in space, the free energy density f can be expanded in a series:

$$f = f_{n0} + \alpha|\psi|^2 + \frac{\beta}{2}|\psi|^4 + \frac{1}{2m^*}\left|\left(\frac{\hbar}{i}\nabla - \frac{e^*}{c}\boldsymbol{A}\right)\psi\right|^2 + \frac{h^2}{8\pi} \tag{2.10}$$

Note that, evidently, when $\psi \to 0$, this is the normal state free energy: $f_{n0} + h^2/8\pi$, where $f_{n0}(T) = f_{n0}(0) - \gamma T^2/2$. Thus, the three remaining terms describe the Superconductivity effects.

In the absence of fields and gradients, we have:

$$f_s - f_n = \alpha|\psi|^2 + \frac{1}{2}\beta|\psi|^4 \tag{2.11}$$

which can be seen as a series expansion in powers of $|\psi|^2$. β must be positive, in order not to have $|\psi|^2$ arbitrarily large. Therefore, two cases arise:

- $\alpha > 0$: the minimum of the free energy occurs at $|\psi|^2 = 0 \Rightarrow$ normal state (Figure 2.3a);
- $\alpha < 0$ (Figure 2.3b)

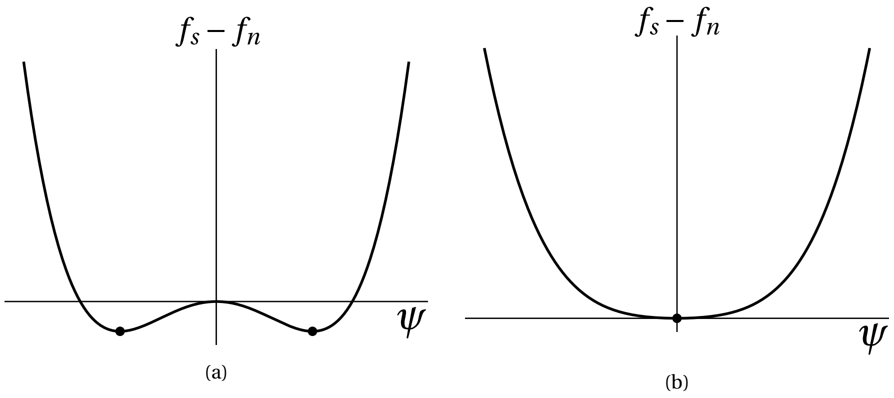

Figure 2.3: Ginzburg-Landau free-energy functions for a) $T > T_c$ $(\alpha > 0)$ and for b) $T < T_c$ $(\alpha < 0)$. Heavy dots indicate equilibrium positions.

In order to obtain the GL equations, one must first minimize f_s in regards to ψ^*:

$$\frac{\partial f_s}{\partial \psi^*} = 2\alpha\psi + \frac{\beta^4}{2}|\psi|^3 = 0 \tag{2.12}$$

Solving this equation yields:

$$\psi(2\alpha + 2\beta|\psi|^2) = 0 \Rightarrow 2\alpha + 2\beta|\psi|^2 = 0 \tag{2.13}$$

Therefore, one gets the following relation for the order parameter:

$$|\psi|^2 = -\frac{\alpha}{\beta} \equiv \psi_0^2, T < T_c, \alpha < 0 \tag{2.14}$$

Substituting ψ_0^2 back into Equation 2.11 yields:

$$f_s - f_n = -\frac{\alpha^2}{2\beta} = -\frac{H_c^2}{8\pi} \tag{2.15}$$

using the definition of the thermodynamical critical field H_c.

To obtain the second GL equation, one must minimize f_s now in regards to $\boldsymbol{A}$:

$$\frac{\partial f_s}{\partial A} = -\frac{e^{*2}}{1m^*c^2}\left[\psi^*\left(\frac{i\hbar c}{e^*}\nabla + \boldsymbol{A}\right)\psi - \psi\left(\frac{i\hbar c}{e^*}\nabla - \boldsymbol{A}\right)\psi^*\right] + \frac{1}{4\pi}\nabla \times (\nabla \times \boldsymbol{A}) = 0 \tag{2.16}$$

Using Ampère's Law: $\nabla \times \boldsymbol{A} = \frac{4\pi}{c}\boldsymbol{J_s}$:

$$\boldsymbol{J_s} = -\frac{e^{*2}}{2m^*c}\left[\frac{i\hbar c}{e^*}(\psi^*\nabla\psi - \psi\nabla\psi^*) + (\psi^*\boldsymbol{A}\psi - \psi\boldsymbol{A}\psi^*)\right] \tag{2.17}$$

which yields, when substituting $\psi = \sqrt{n_s}e^{i\phi}$:

$$\boldsymbol{J_s} = -\frac{e^*\hbar}{2m^*}|\psi|^2\left(\nabla\phi + \frac{e^*}{\hbar c}\boldsymbol{A}\right) \tag{2.18}$$

which describes the behavior of the supercurrent.

We have finally arrived at the Ginzburg-Landau differential equations:

$$\alpha\psi + \beta|\psi|^2\psi + \frac{1}{2m^*}\left(\frac{\hbar}{i}\nabla - \frac{e^*}{c}\boldsymbol{A}\right)^2\psi = 0 \tag{2.19a}$$

$$\boldsymbol{J_s} = \frac{e^*}{m^*}|\psi|^2\left(\hbar\nabla\phi - \frac{e^*}{c}\boldsymbol{A}\right) \tag{2.19b}$$

Furthermore, the parameters follow the relations near criticality:

$$\alpha(t) = \alpha'(t-1), \alpha\text{'} > 0,\ t = T/T_c \tag{2.20a}$$

$$|\psi|^2 \propto (1-t) \tag{2.20b}$$

To make these considerations quantitative, we take a look at the last term of Equation 2.10:

$$\frac{1}{2m^*}\left|\left(\frac{\hbar}{i}\nabla - \frac{e^*}{c}\boldsymbol{A}\right)\psi\right|^2 + \frac{h^2}{8\pi} \tag{2.21}$$

The first term is the energy associated with gradients in the order parameter, whereas the second one is the kinetic energy associated with supercurrent. In the London gauge, ϕ is constant, thus the term is simply

$$K_{sc} = \frac{e^{*2}A^2|\psi|^2}{2m^8c^2} \tag{2.22}$$

Equating this to the energy density for a superconductor in the London theory ($A^2/8\pi\lambda_{\text{eff}}^2$), one gets:

$$\lambda_{\text{eff}}^2 = \frac{m^*c^2}{4\pi|\psi|^2e^{*2}} \tag{2.23}$$

which agrees with the usual definition for the London penetration depth, apart from the starred numbers (the explanation for these will be covered in the next section; no need to worry about it now).

With these definitions, we can now write down the parameters of the Ginzburg-Landau theory:

$$|\psi|^2 \equiv n_s = \frac{m^*c^2}{4\pi e^{*2}\lambda_{\text{eff}}^2} \tag{2.24a}$$

$$\alpha(T) = -\frac{e^{*2}}{m^*c^2}H_c^2(T)\lambda_{\text{eff}}^2(T) \tag{2.24b}$$

$$\beta(T) = \frac{4\pi e^{*4}}{m^{*2}c^4H_c^2(T)\lambda_{\text{eff}}^4(T)} \tag{2.24c}$$

Furthermore, the theory also introduced a new parameter, now called the **coherence length**. We can obtain it by exploring further the Equation 2.19a, considering the one-dimentional case without any fields ($\boldsymbol{A} = 0$) and introducing a normalized wave function $\Psi = \psi/\psi_0$:

$$\frac{\hbar^2}{2m^*|\alpha|}\frac{d^2\Psi}{dx^2} + \Psi - \Psi^3 = 0 \tag{2.25}$$

$$\xi^2(T) = \frac{\hbar^2}{|2m^*\alpha(T)|} \propto \frac{1}{1-t} \tag{2.26}$$

which caracterizes the spatial extent over which $\psi(\boldsymbol{r})$ can vary without undue energy increase. Thus, it provides a measure for how far superconducting correlations persist in space.

To calculate its value, one must susbtitute the value of α from Equation 2.24b into the definition of ξ:

$$\xi(T) = \frac{\Phi_0}{2\sqrt{2}\pi H_c(T)\lambda_{\text{eff}}(T)} \tag{2.27}$$

where $\Phi_0 = hc/e^*$ is the fluxoid quantum (explained in the next section).

Moreover, the ratio of the two characteristic lengths is called the Ginzburg-Landau parameter:

$$\kappa = \frac{\lambda}{\xi} \tag{2.28}$$

For typical classic superconductors at the time, $\lambda \approx 500$ Åand $\xi \approx 3000$ Å, thus $\kappa \ll 1$. In this case, there is a positive surface energy associated with the boundary between normal and superconducting states. Such surface energy favours the formation of domain patters in the intermediate state: it is energetically favorable to be subdivided into normal and superconducting state rather than being fully one or another. The sizes of such domains vary between the coherence length ξ and the sample size.

There are a handful of achievements the Ginzburg-Landau (GL) theory has accomplished, extending the scope of the London theory. Namely:

1. nonlinear effects of fields strong enough to change n_s;
2. the spatial variation of n_s;
3. handling the intermediate state (when $H \approx H_c$) - see Figure 2.4.

Type-I and Type-II Superconductors

In 1957, Alexei A. Abrikosov published a remarkable paper [34] investigating what would happen if instead κ was large, i.e., $\xi < \lambda$. This would lead to a negative surface energy

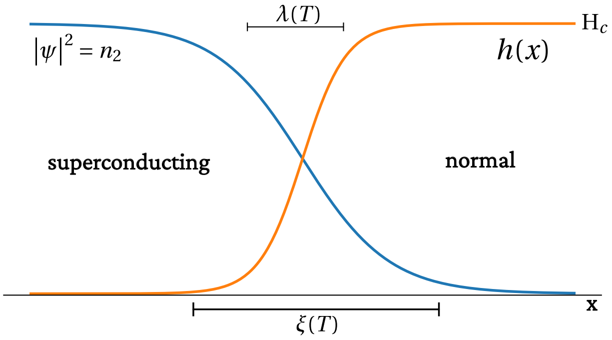

Figure 2.4: Interface between normal and superconducting domains in the intermediate state.

(instead of positive one explained above), which limits the process of subdivision into domains to the size of ξ. Since this is radically different from the previous behaviour, Abrikosov named these "type-II superconductors", and predicted the breakpoint between the types to be at $\kappa = 1/\sqrt{2}$:

- $\kappa < 1/\sqrt{2} \Rightarrow$ type-I superconductor;
- $\kappa > 1/\sqrt{2} \Rightarrow$ type-II superconductor.

The difference between type-I and type-II in terms of ξ and λ can be seen in Figure 2.5:

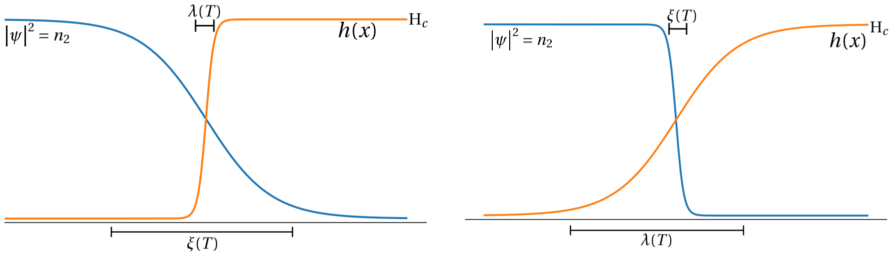

(a) $\kappa \ll 1$ (b) $\kappa \gg 1$

Figure 2.5: Schematic diagram of variation of h and ψ in a domain wall. a) Refers to a type-I superconductor, whereas b) is the case for a type-II.

For the $\kappa \gg 1$, he discovered the magnetic flux didn't penetrate the sample through a discontinuous breakdown of superconductivity at H_c, but rather was continuosly increased above a lower critical field H_{c1} until an upper critical field H_{c2}, above which the superconductivity is destroyed. Since $H_{c2} = \sqrt{2}\kappa H_c$, the diamagnetic cost of keeping the magnetic field out is less than for type-I, therefore making it possible to have high-field superconducting magnets (widely used nowadays especially in NMR).

The state between fields H_{c1} and H_{c2} is called the **mixed** or **Schubnikov phase**, and the magnetic flux does not penetrate in a laminar flux, but in a regular array of flux tubes, each carrying a quantum of flux.

$$\Phi_0 = \frac{hc}{2e} = 2.07 \times 10^{-7} \mathrm{G\,cm}^2 \tag{2.29}$$

Within each tube, there is a vortex of supercurrents that concentrates the flux toward the vortex center. The most favorable configuration of such vortex arrays is a triangular one.

2.2 Microscopic Theory: Bardeen-Cooper-Schrieffer

After such prolific advances were made in the field of superconductivity, one question still persisted: What essentially makes electrons superconduct? No one still had that answer, but in the beginning of the '50s, that started to change.

In 1950, E. Maxwell published the discovery of the isotope effect in mercury (Hg) [32]. Around the same time, Reynolds and his peers carried out a more specific study on the isotope effect of Mercury, varying the atomic mass further to strengthen their thesis [33]. They realized that for elements with different isotopes, which is the case for Hg, the critical temperature changed with the isotopic mass. More specifically, they obey the following relation:

$$T_c \propto M^{-\alpha} \tag{2.30}$$

where $\alpha \approx 1/2$ for most metals and M is the atomic mass.

At almost the same time as Maxwell and Reynolds, Herbert Fröhlich introduced the idea that the electron-phonon interaction was responsible for creating an attractive force between electrons, which made them superconduct. In his paper [46], Fröhlich realised that electrons can have an attractive interaction mediated by lattice vibrations. He proved it through the isotope effect: The dependence of the critical temperature on the atomic mass is the same as the Debye frequency (the maximum frequency of the lattice vibrations in a solid), $\omega_D \propto M^{-1/2}$. He was the first to suggest that superconductivity was caused by the electron-phonon interaction. This was an essential discovery to pave the way for the BCS theory to rise.

In the following sections, the BCS theory will be explained and a more palpable approach to the mathematics of it will be adopted, for the sake of keeping this reading interesting. In addition to reference [44], reference [47] will also be used to construct such sections.

Cooper Instability

Let us start with the concept of Cooper instability. He introduced the idea in 1956 [48], and proved that the ground state of a normal metal was unstable at zero temperature. In this condition, the material prefers to be in the superconducting state. He further suggested that the instability was caused precisely by the scattering between pairs of electrons, and that the scattering potential is the exchange of phonons:

$$V_s(\boldsymbol{q},\omega) = \frac{v_q}{\epsilon(\boldsymbol{q},\omega)} + \frac{2\omega\lambda M_q^2}{\epsilon(\boldsymbol{q})^2[\omega^2 - \omega_\lambda(\boldsymbol{q})^2]} \tag{2.31}$$

The first term is the Coulomb repulsion between the two electrons. The second term is the electron-phonon interaction. It is, on the average, weaker than the Coulomb interaction. However, the denominator can be small and negative as long as $\omega < \omega_D$, making the second term larger as a whole. The idea is that a material can superconduct if the energy of the electron-phonon interaction is relatively larger; the electrons must possess a wave function which selects a frequency inside the range pointed above, thus creating an attractive energy.

To proceed with the calculations, we will replace the previous potential by a simpler model[1]:

$$V_s(\boldsymbol{q},\omega) = \begin{cases} -V_0 & \text{for } |\xi_q| < \omega_D, \\ 0 & \text{for } |\xi_q| > \omega_D \end{cases} \tag{2.32}$$

where ξ_q is the energy of an electron with momentum $\boldsymbol{q}$ and $V_0 > 0$. Therefore, the potential is constant and attractive for energies up to the Debye energy ω_D.

In Cooper's model, the free-electron model is assumed. In the zero temperature limit, the Fermi surface has a sharp step in energy, and the electrons are allowed to have such attrative interaction. We assume a mutual scattering process, where the electrons possess equal and opposite moments $\boldsymbol{k}$ and $-\boldsymbol{k}$ and spins $\uparrow$ and $\downarrow$.

Now, consider a double scattering event. This is the scattering in the second Born approximation, and the dashed line represents the interaction of Equation 2.32. The two electrons start with momentum $\boldsymbol{k}$ and $-\boldsymbol{k}$, and a momentum transfer $\boldsymbol{q}$ leaves them with (opposite) momentums $(\boldsymbol{k}+\boldsymbol{q})$ and $--(\boldsymbol{k}+\boldsymbol{q})$. The moments $\pm\boldsymbol{k_I}$ in the figure are the intermediate states of the scattering, whereas $\pm\boldsymbol{k'}$ are the final ones.

After some calculations, one arrives at the following effective scattering in the first and second Born approximations:

$$V_{\text{eff}} = -V_0\left[1 - N_F V_0 \ln\left(\frac{\xi}{\omega_D}\right)\right] \tag{2.33}$$

The term $-N_F V_0 \ln(\xi/\omega_D)$ is the vertex correction which results from the additional scattering between electrons. If we consider a sum of $n+1$ diagrams, there will be n contributions of:

$$-V_0\left[-N_F V_0 \ln\left(\frac{\xi}{\omega_D}\right)\right]^n \tag{2.34}$$

The summation of such terms yields to the effective potential:

---

[1] The initial BCS calculations were performed with this potential

$$V_{\text{eff}} = -V_0 \sum_{N=0}^{\infty} \left[-N_F V_0 \ln\left(\frac{\xi}{\omega_D}\right)\right]^n \tag{2.35}$$

$$= -\frac{V_0}{1 + N_F V_0 \ln(\xi/\omega_D)} \tag{2.36}$$

Note that the potential has a pole at:

$$\xi_0 = \omega_D \exp[-1/N_F V_0], \tag{2.37}$$

which is sufficient to cause the instability. The electrons near the Fermi energy will interact with their pair on the opposite side of the Fermi sea. The mutual scattering produces a pole in the scattering amplitude, which makes the electrons bind as pairs. This happens to all the electrons in the Fermi energy, hence a phase transition occurs.

Furthermore, seeing the instability as a function of temperature, one can see that the effective potential has an energy denominator of the form:

$$V_{\text{eff}} = -\frac{V_0}{1 + N_F V_0 \ln\left(\sqrt{\xi^2 + (k_B T)^2}/\omega_D\right)} \tag{2.38}$$

At zero energy ($\xi = 0$), V_{eff} becomes singular when the temperature is lowered to the T_c:

$$k_B T_c = \omega_D \exp\left[-\frac{1}{N_F V_0}\right] \tag{2.39}$$

This correctly predicts the form of the transition temperature for the BCS theory:

$$k_B T_c = 1.14 \omega_D \exp\left[-\frac{1}{N_F V_0}\right] \tag{2.40}$$

Note how the result is proportional to the Debye energy, just as the isotope effect.

Therefore, the physical idea behind the pairing is that the first electron polarizes the medium by attracting positive ions; which in turn attract the second electron, giving rise to an attractive interaction between the electrons. If this attraction is strong enough to overcome the Coulomb interaction between these electrons, then they will have an attractive interaction and superconductivity results. These electrons form a pair now called **Cooper pairs**, after physicist Leon Cooper and his work just prior to the BCS paper [48]. The Cooper pairs, in the superconducting state, are the charge carriers, and since they are now bosons (because they are made of two fermions), they are condensed in the same state and thus can conduct electric currents without scattering and energy loss.

The BCS Ground State

We have now seen that the Fermi sea is unstable against the formation of a bound Cooper pair when there is an attractive interaction, so we must expect pairs to condense until an equilibrium point is achieved. This will happen when the state of the system is so changed from the Fermi sea that the binding energy for an additional pair has gone to zero. To handle this mathematically, John Bardeen, Leon Cooper and John Schrieffer proposed a very interesting mathematical form: the BCS wave function.

The wave function which describes pairs of electrons is more conveniently written using the language of second quantization. We denote the occupied states by creation operators $c^\dagger_{\boldsymbol{k}\uparrow}$, whereas the annihilation operator $c_{\boldsymbol{k}\uparrow}$ empties the corresponding state. The most general N-electron wave function in terms of momentum eigenfunctions and with the Cooper pairing is:

$$\left|\psi_N\right\rangle = \sum g(\boldsymbol{k_i},...\boldsymbol{k_l}) c^\dagger_{\boldsymbol{k_i}\uparrow} c^\dagger_{-\boldsymbol{k_i}\downarrow} ... c^\dagger_{\boldsymbol{k_l}\uparrow} c^\dagger_{-\boldsymbol{k_l}\downarrow} \left|\phi_0\right\rangle \tag{2.41}$$

where $\left|\phi_0\right\rangle$ is the vacuum state with no particles, $\boldsymbol{k_i}$ and $\boldsymbol{k_l}$ are the first and last of the M $\mathbf{k}$ values of the band which are occupied and g is a weighing coefficient with which the product of this set of $N/2$ pairs of creation operators appears.

To simplify the calculations, BCS argued that the occupancy of each state $\boldsymbol{k}$ is dependent only on the average occupancy of other states, instead of summing over all the possible ways of choosing the $N/2$ states for pair occupancy. Essentially, we work with a grand canonical ensemble. Therefore, the ground state for the BCS theory is:

$$\left|\psi_G\right\rangle = \prod_{\boldsymbol{k}=\boldsymbol{k}_1,...,\boldsymbol{k}_M} (u_{\boldsymbol{k}} + v_{\boldsymbol{k}} c^\dagger_{\boldsymbol{k}\uparrow}) c^\dagger_{-\boldsymbol{k}\downarrow} \left|\phi_0\right\rangle \tag{2.42}$$

where $|u_{\boldsymbol{k}}|^2 + |v_{\boldsymbol{k}}|^2 = 1$. The probability of the pair $(\boldsymbol{k}\uparrow, -\boldsymbol{k}\downarrow)$ is $|v_{\boldsymbol{k}}|^2$, whereas the probability of it being unoccupied is $|u_{\boldsymbol{k}}|^2 = 1 - |v_{\boldsymbol{k}}|^2$.

At last, the pairing Hamiltonian is:

$$\hat{\mathscr{H}} = \sum_{\boldsymbol{k}\sigma} \epsilon_{\boldsymbol{k}} n_{\boldsymbol{k}\sigma} + \sum_{\boldsymbol{kl}} V_{\boldsymbol{kl}} c^\dagger_{\boldsymbol{k}\uparrow} c^\dagger_{-\boldsymbol{k}\downarrow} c_{-\boldsymbol{l}\downarrow} c_{\boldsymbol{l}\uparrow} \tag{2.43}$$

where $\epsilon_{\boldsymbol{k}}$ is the energy of an electron and $V_{\boldsymbol{kl}}$ is the attractive interaction between them.

With this Hamiltonian and the ground state wave function, one can define the following quantities:

$$\Delta \equiv -\sum_{\boldsymbol{l}} V_{\boldsymbol{kl}} u_{\boldsymbol{l}} v_{\boldsymbol{l}} \tag{2.44}$$

and

$$E_{\boldsymbol{k}} \equiv (\Delta^2 + \xi^2_{\boldsymbol{k}})^{1/2} \tag{2.45}$$

where $\xi_{\boldsymbol{k}}$ is the single-particle energy. $E_{\boldsymbol{k}}$ is the excitation energy of a quasi-particle of momentum $\hbar\boldsymbol{k}$ and Δ is the minimum excitation energy, or **energy gap**. In the weak coupling limit, $N(0)V \ll 1$, thus:

$$\Delta \approx 2\hbar\omega_D \exp\left(-\frac{1}{N(0)V}\right) \tag{2.46}$$

In the BCS theory, when the electrons pair up and transition to the superconducting state, an energy gap opens up in the Fermi level, given by 2.46. . At first, before the transition, the electrons are unpaired; thus, they behave as fermions (they obey the Fermi-Dirac statistics). After the transition, they form bosons (S = 0) and can move freely in the region of occupied states (there is no restriction in their quantum numbers because they now obey the Bose-Einstein statistics). Hence, the Cooper pairs can conduct electric currents without dissipation.

However, if one provides energy $E > \Delta$, the pairs break and are no longer superconducting. Note that one cannot break one or another pair: the energy one must provides either break all of them ($E > \Delta$) or none of them ($E < \Delta$).

3 NUCLEAR MAGNETIC RESONANCE

This Chapter builds the theoretical foundations to understand the resonance phenomenon in nuclei, and are mostly based on Reference [49]. The goal is to familiarize the reader with this technique using a semi-classical approach of nuclei in a static magnetic field, and to use this knowledge to understand how one measures nuclear resonances in the laboratory.

3.1 Introduction

The phenomenon of nuclear magnetic resonance (NMR) is found in systems which possess both angular and magnetic moments (i.e., when the nuclear spin is nonzero). It was first observed by physicist Isidor Rabi in 1938 [50], while working with molecular beams in the Stern-Gerlach experiment. Felix Bloch and Edward Purcell expanded the technique for both solids and liquids [51, 52] in 1946. What all of them observed is that the nuclei, when inserted in a magnetic field, could absorb energy in the range of radio-frequency (RF) waves; in such situation, the nucleus is said to be in *resonance*. Moreover, for the same magnetic field, the energy absorption happens in different frequencies for different isotopes. Each isotope precesses at an specific value of frequency when in a static magnetic field; this frequency is called *Larmor frequency*. For nuclear spins, this frequency lies in the range of radio-frequency (up to 900 MHz), whilst for electron spins, the frequency range is microwave (up to 300 GHz).

The most prominent feature of this technique is the possibility to single out the magnetic susceptibility of the isotope observed, rather than the total bulk magnetic susceptibility. This allows for complex information to be obtained: in Physics, its relevance lies in gathering information on atomic level not obtainable in other ways [49], whereas in Chemistry, such technique provides information on the molecule composition, such as its atoms and the chemical bonds between them.

3.2 Theory of the Resonance Phenomenon

Our system, composed of many nuclei, possesses a total magnetic moment $\boldsymbol{\mu}$ and a total angular momentum $\mathbf{J}$. Taking both vectors to be parallel:

$$\boldsymbol{\mu} = \gamma \mathbf{J}, \tag{3.1}$$

where $\gamma = \frac{e}{2mc}$ is the gyromagnetic ratio of the isotope.

The application of a magnetic field **H** produces an interaction energy of the nucleus of $-\boldsymbol{\mu}\cdot\mathbf{H}$. Then, the Hamiltonian can be written as:

$$\mathscr{H} = -\boldsymbol{\mu}\cdot\boldsymbol{H} \Rightarrow \mathscr{H} = -\gamma\hbar H_0 I_z, \tag{3.2}$$

where H_0 is the static magnetic field and I_z is the z-component of the nuclear spin.

The allowed energies are the eigenvalues of this Hamiltonian:

$$E_m = -\gamma\hbar H_0 m, \mathrm{m} = \text{-1, ..., 1}, \tag{3.3}$$

i.e., a set of $2m+1$ eigenenergies separated by an energy $\gamma\hbar H_0$.

It is possible to detect the presence of such energy level by spectral absorption. Therefore, it is necessary to have an interaction in the system that can cause transitions between those levels. In order to satisfy conservation of energy, this interaction must be time dependent and of angular frequency ω such that:

$$\hbar\omega = \Delta E = \gamma\hbar H_0 \Rightarrow \tag{3.4}$$

$$\boxed{\omega = \gamma H_0} \tag{3.5}$$

where ΔE is the energy difference between the Zeeman energies. Note that the Planck's constant no longer appears in the resonance condition. That suggests us that a classical approach is quite valid for resonance theory. Therefore, such approach will be introduced shortly, and later on the quantum description will also be explored.

3.3 Dynamics of Spin Populations

3.3.1 Classical Treatment of the Motion of Spins

We aim to analyze the motion of a spin in a time-dependent magnetic field H, which can exert a torque on the spin given by $\boldsymbol{\mu} \times \boldsymbol{H}$. Assuming the field is constant in time and there are no energy losses, the magnetic moment would oscillate around its equilibrium position. Otherwise, if there are energy losses, it would stop oscillating and align with the magnetic field.

Since the spin also possesses angular momentum, it also acts as a gyroscope in this scenario. Therefore, the torque and angular momentum follow the relation:

$$\frac{d\boldsymbol{J}}{dt} = \mu \times \mathbf{H} \tag{3.6}$$

Since $\boldsymbol{\mu} = \gamma\mathbf{J}$, one gets:

$$\frac{d\boldsymbol{\mu}}{dt} = \boldsymbol{\mu} \times (\gamma \boldsymbol{H}) \tag{3.7}$$

Equation 3.7 can be solved using a rotating coordinate system. Consider a vector function of time $F(t)$ which can be written in rectangular coordinates:

$$\boldsymbol{F} = \boldsymbol{i}F_x + \boldsymbol{j}F_y + \boldsymbol{k}F_z$$

Now, we assume vectors $\boldsymbol{i}, \boldsymbol{j}$ and $\boldsymbol{k}$ are of fixed length, but can rotate with angular velocity Ω. Thus:

$$\frac{d\boldsymbol{i}}{dt} = \boldsymbol{\Omega} \times \boldsymbol{i} \tag{3.8}$$

The time derivative of F is:

$$\frac{d\boldsymbol{F}}{dt} = \frac{\delta \boldsymbol{F}}{\delta t} + \boldsymbol{\Omega} \times \boldsymbol{F} \tag{3.9}$$

Applying Equation 3.7 to 3.9:

$$\frac{\delta \boldsymbol{\mu}}{\delta t} + \boldsymbol{\Omega} \times \boldsymbol{\mu} = \boldsymbol{\mu} \times \gamma \boldsymbol{H} \Rightarrow \frac{\delta \boldsymbol{\mu}}{\delta t} = \boldsymbol{\mu} \times (\gamma \boldsymbol{H} + \boldsymbol{\Omega}) \tag{3.10}$$

Note that 3.10 tells us there is an equivalence in the equation of motion for the rotating reference and the laboratory system, as long as the magnetic field is replaced by an effective field H_e:

$$H_e = H + \frac{\Omega}{\gamma} \tag{3.11}$$

Assuming the field is in the z-direction, $\boldsymbol{H} = \boldsymbol{k}H_0$, the equation of motion can be solved by choosing Ω such that $H_e = 0$. Therefore:

$$\boldsymbol{\Omega} = -\gamma H_0 \boldsymbol{k} \tag{3.12}$$

Consequently, the magnetic moment rotates with an angular velocity $\boldsymbol{\Omega}$, as defined in Equation 3.12, relative to the laboratory reference frame. The angular frequency γH_0 is known as the **Larmor frequency**.

3.3.2 Quantum Mechanical Description of a Spin in a Magnetic Field

It was stated previously that the available energies for a spin in a magnetic field are given by Equation 3.4. Denoting the corresponding eigenfunctions of the time- independent Schrödinger equation by $u_{I,m}$, the time-dependent solution for a value of m is:

$$\Psi_{I,m}(t) = u_{I,m} e^{-(i/\hbar)E_m t} \tag{3.13}$$

Therefore, the most general solution is:

$$\Psi(t) = \sum_{m=-I}^{+I} c_m u_{I,m} e^{-(i/\hbar)E_m t} \tag{3.14}$$

where $c_m \in \mathbb{C}$.

We can use $\Psi(t)$ to compute the expectation value of any observable. Let us do it for the x-component of the magnetic moment:

$$\langle \mu_x(t) \rangle = \int \Psi^* \mu_x \Psi(t) \tag{3.15}$$

Using $\mu_x = \gamma\hbar I_x$, we get:

$$\langle \mu_x(t) \rangle = \sum_{m,m'} \gamma\hbar c^*_{m'} C_m (m'|I_x|m) e^{(i/\hbar)(E_{m'}-E_m)t} \tag{3.16}$$

where $(m'|I_x|m) \equiv \int u *_{Im'} I_x u_{Im} d\tau$.

The expectation values will generally be time-dependent with terms that oscillate harmonically with frequencies $(E_{m'} - E_m)/\hbar$, which are simply the absorption or emission of energy between states m and m'.

Since the matrix elements $(m'|I_x|m)$ vanish unless $m' = m \pm 1$, all terms in Equation 3.16 exhibit angular frequencies of $+\gamma H_0$ or $-\gamma H_0$. Consequently, the expectation values $\langle \mu_x(t) \rangle$ and $\langle \mu_y(t) \rangle$ oscillate over time. However, it can be shown that $\langle \mu_z(t) \rangle$ remains constant, implying that $\langle \boldsymbol{\mu} \rangle$ undergoes precession in the x-y plane while maintaining a fixed angle with the z-axis.

To establish the equivalence between classical and quantum descriptions, we employ the equations of motion for the expectation value $\langle \boldsymbol{\mu} \rangle$. Using the Zeeman Hamiltonian (Equation 3.2) and the commutation relation for I, namely $[I_x, I_y] = iI_z$, we obtain the time derivatives of the components of I:

$$\frac{dI_x}{dt} = \gamma H_0 I_y \tag{3.17}$$

$$\frac{dI_y}{dt} = \gamma H_0 I_x \tag{3.18}$$

$$\frac{dI_z}{dt} = 0 \tag{3.19}$$

These are the component equations corresponding to the vector equation of motion:

$$\frac{d\boldsymbol{I}}{dt} = \boldsymbol{I} \times \gamma \boldsymbol{H} \tag{3.20}$$

Since $\boldsymbol{\mu} = \gamma\hbar\boldsymbol{I}$, the expectation value for the magnetization is simply:

$$\frac{d\langle \boldsymbol{\mu} \rangle}{dt} = \langle \boldsymbol{\mu} \rangle \times \gamma \boldsymbol{H} \tag{3.21}$$

This result precisely matches the classical equation, demonstrating that the expectation value of the magnetization follows the classical equation of motion. It is important to emphasize that Equation 3.21 remains valid even for a time-dependent $\boldsymbol{H}$, not just a static field.

3.3.3 Classical Description of the Effects of an Alternating Magnetic Field

For now, we turn our attention to the effects on the motion of spins of an alternating field, and here it will suffice to use the classical approach. Let us begin with the following field:

$$\boldsymbol{H_1} = H_1(\boldsymbol{i}\cos(\omega_z t) + \boldsymbol{j}\sin(\omega_z t)) \tag{3.22}$$

where ω_z is the z-component of ω. Thus, our equation of motion for a spin (under the influence of $\boldsymbol{H_0}$ and $\boldsymbol{H_1}$) becomes:

$$\frac{d\boldsymbol{\mu}}{dt} = \boldsymbol{\mu} \times \gamma[\boldsymbol{H_0} + \boldsymbol{H_1}(t)] \tag{3.23}$$

We can eliminate the time dependence of $\boldsymbol{H_1}$ by switching to a coordinate system that rotates about the z-axis with frequency ω_z. Note that $\boldsymbol{H_0}$ will also be static in this reference frame for it lies along the rotation axis (remember: $\boldsymbol{H_0} = \boldsymbol{k}H_o$). Therefore, Equation 3.23 becomes:

$$\frac{\delta \boldsymbol{\mu}}{\delta t} = \boldsymbol{\mu} \times [\boldsymbol{k}(\omega_z + \gamma H_0) + \boldsymbol{i}\gamma H_1] \tag{3.24}$$

One can rewrite Equation 3.24 to emphasize that, near resonance, $\omega_z \gamma H_0 \cong 0$. Setting $\omega_z = -\omega$ $(\omega > 0)$:

$$\frac{\delta \boldsymbol{\mu}}{\delta t} = \boldsymbol{\mu} \times \gamma \left[\left(H_0 - \frac{\omega}{\gamma} \right) \boldsymbol{k} + H_1 \boldsymbol{i} \right] \tag{3.25}$$

$$= \boldsymbol{\gamma} \times \boldsymbol{H}_{\text{eff}} \tag{3.26}$$

where

$$\boldsymbol{H}_{\text{eff}} = \boldsymbol{k} \left(H_0 - \frac{\omega}{\gamma} \right) + H_1 \boldsymbol{i} \tag{3.27}$$

Physically, this implies that in the rotating frame, the magnetic moment experiences an effective static field $\boldsymbol{H}_{\text{eff}}$ and undergoes precessional motion, tracing a conical path with a fixed angle around the direction of this field. This behavior is depicted in Figure 3.1.

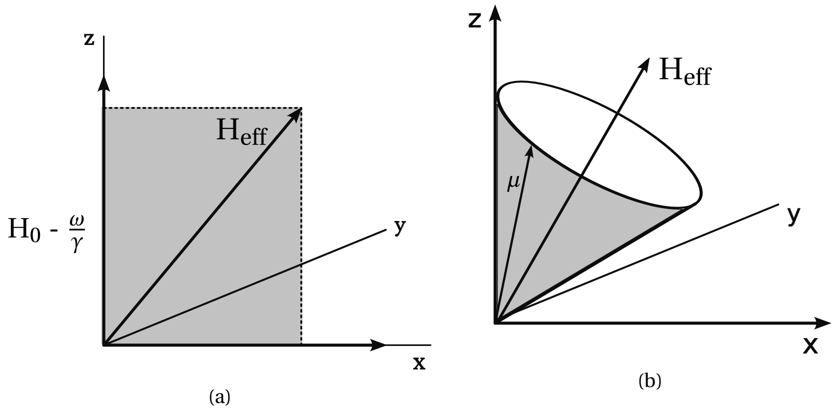

(a) (b)

Figure 3.1: a) Effective field. b) Precessional motion of the magnetic moment μ in the rotating reference frame.

When the resonance condition is met ($\omega = \gamma H_0$), the effective field reduces to $\boldsymbol{i} H_1$. Consequently, a magnetic moment initially aligned with the static field will precess within the y-z plane while remaining perpendicular to H_1. If there is such a situation in which the spin is parallel to the static field (along $\boldsymbol{k}$) and an oscillating field is turned on for short time t_ω, the magnetic moment would then precess at an angle $\theta = \gamma H_1 t_\omega$. If $\theta = \pi/2$, the moment will align with the y-axis, instead of the z-axis, whereas if $\theta = \pi$, the pulse will invert the moment (align with the $-z$-direction). By turning off H_1, the moment would remain at rest in the rotating frame, therefore precess in the lab frame, pointing normal to the static field.

Building on this concept, we can devise a straightforward method for detecting nuclear magnetic resonance. The sample is placed inside a coil whose axis is **perpendicular** to $\boldsymbol{H_0}$. In thermal equilibrium, the magnetic moments align with $\boldsymbol{H_0}$. An alternating magnetic field ($\boldsymbol{H_1} \perp \boldsymbol{H_0}$) is generated by applying an alternating voltage to the coil. By carefully tuning the values of H_1 and ωt, a $\pi/2$ pulse is applied. As a result, the excess magnetization becomes perpendicular to $\boldsymbol{H_0}$ and precesses at an angular frequency γH_0. This precession induces a flux through the coil, generating an electromotive force (emf) that can be detected. This process is illustrated in Figure 3.2.

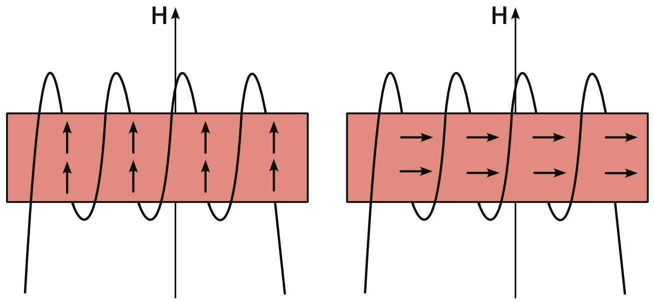

(a) (b)

Figure 3.2: a) Coil containing the sample, where an excess of magnetic moments aligns with H_0 in thermal equilibrium. b) After applying a $\pi/2$ pulse, the magnetic moments precess perpendicular to H_0.

In practice, due to interactions with neighbouring spins, the induced emf decays, which lasts typically 100 μs for solids. Still, the moments will precess for several periods before decay. This technique is called "free induction decay" (or FID), a decay "free" of H_1, and can be very useful for observing resonances.

3.3.4 Bloch Equations and Relaxation Processes

We have seen in that the motion of noninteracting spins have a periodic motion of the magnetization in the rotating frame. However, there are certain interactions of the spins that can alter such behaviour. The Bloch Equations are a set of equations which describe the dynamics of nuclear magnetization in the presence of a magnetic field. By definition, the magnetization of a spin population, each one with magnetic moment $\boldsymbol{\gamma}$ is:

$$\boldsymbol{M} = \frac{1}{V}\sum \boldsymbol{\mu} \tag{3.28}$$

where V is the volume of the system.

For a spin 1/2 system in a static magnetic field H_0, the resulting magnetization arises from the population difference between the energy levels $E \pm \gamma\hbar H$. In thermal equilibrium, the state with energy $-\gamma\hbar H_0$ is the most energetically favorable, hence the magnetization tends to align with the static field. In this case, the magnetization has only one component, $\mathrm{M}_z = \mathrm{M}_0$.

Once the pulse field H_1 is applied (and satisfies the resonance conditions), the system is removed from the equilibrium position. For instance, applying a $\pi/2$ pulse makes the population of the energy levels $E \pm \gamma\hbar H$ become equal, by absorbing the pulse energy. Now, considering a heat reservoir (in our case, it can be either the crystalline lattice or the LHe bath in which the sample lies) to change the sample's temperature, it is reasonable to assume that, after the perturbation, the magnetization will tend to its equilibrium position in a rate proportional to $M_0 - M_z$, i.e.:

$$\frac{dM_z}{dt} = \frac{M_0 - M_z}{T_1} \tag{3.29}$$

where T_1 is the spin-lattice relaxation time and describes how long the $z-$component of the magnetization takes to return to its equilibrium position, parallel to H_0. After a $\pi/2$ pulse, the magnetization is taken to the $x - y$ plane. Then, the $xy-$component starts to lose its intensity, whereas the z-component starts increasing again, until M_0 is again aligned with the static field H_0. This process is called relaxation, hence T_1 is a relaxation time.

Combining 3.29 with the equation for the torque, we finally get:

$$\frac{dM_z}{dt} = \frac{M_0 - M_z}{T_1} + \gamma(\boldsymbol{M} \times \boldsymbol{H}_z) \tag{3.30}$$

Moreover, expressing the fact that the magnetization tends to be parallel to H_0 in thermal equilibrium under a static field. Thus, the $x-$ and $y-$components tend to zero:

$$\frac{dM_x}{dt} = \gamma(\boldsymbol{M} \times \boldsymbol{H})_x - \frac{M_x}{T_2} \tag{3.31a}$$

$$\frac{dM_y}{dt} = \gamma(\boldsymbol{M} \times \boldsymbol{H})_y - \frac{M_y}{T_2} \tag{3.31b}$$

where T_2 is the spin-spin relaxation time, which describes how long it takes for $\mathrm{M_{xy}}$ to return to zero, after $\mathrm{M_0}$ is removed from equilibrium by a $\pi/2$ pulse. Note how the relaxation time for the $x-$ and $y-$components is the same, but it is different to the one for the $z-$component. This is due to the fact that the transverse decay conserves energy in the static field, whereas that is not true for the longitudinal decay.

Equations 3.30 and 3.31b, first published by Felix Bloch in 1946, are commonly referred to as the **Bloch equations** [51].

As an example, we can solve the Bloch equations for low H_1. We begin by transforming to the rotating reference frame at ω_z, aligning H_1 along the x-axis, and denoting $H_0 + (\omega_z/\gamma)$ as h_0. Thus:

$$\frac{dM_z}{dt} = -\gamma M_y H_1 + \frac{M_0 - M_z}{T_1} \tag{3.32a}$$

$$\frac{dM_x}{dt} = \gamma M_y h_0 - \frac{M_x}{T_2} \tag{3.32b}$$

$$\frac{dM_y}{dt} = \gamma(M_z H_1 - M_x h_0) - \frac{M_y}{T_2} \tag{3.32c}$$

Since M_x and M_y must vanish as $H_1 \to 0$, we note from 3.32a that in a steady state, M_z differs from M_0 to order H_1^2. We therefore replace M_z by M_0 in Equation 3.32c.

The solutions to these equations can be written as:

$$M_x = \chi_0(\omega_0 T_2)\frac{(\omega_0 - \omega)T_2}{1 + (\omega - \omega_0)^2 T_2^2} H_1 \tag{3.33a}$$

$$M_y = \chi_0(\omega_0 T_2)\frac{1}{1 + (\omega - \omega_0)^2 T_2^2} H_1 \tag{3.33b}$$

Equation 3.33b demonstrates that the magnetization remains constant in the rotating frame, meaning it rotates at a frequency ω in the laboratory frame. Since the magnetization can be measured by the emf it induces in a fixed coil (in the laboratory frame), one can calculate this emf from the magnetization M_X.

The components of the magnetization in both frames can be related in the following manner (see Figure 3.3):

$$M_X = M_x \cos\omega t + M_y \sin\omega t \tag{3.34}$$

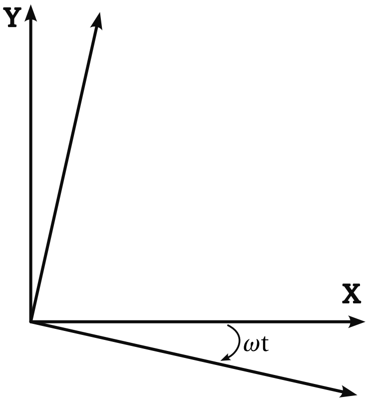

Figure 3.3: Rotating axes x, y relative to laboratory axes X, Y.

Since the magnetic field is linear:

$$H_X(t) = H_{X0}\cos\omega t \tag{3.35a}$$

$$2H_1 = H_{\mathrm{X}0}, \tag{3.35b}$$

one sees that both M$_x$ and M$_y$ are proportional do $H_{\mathrm{X}0}$, thus:

$$M_X(t) = (\chi'\cos\omega t + \chi''\sin\omega t)H_{\mathrm{X}0}, \tag{3.36}$$

where the quantities χ' and χ'' are defined by:

$$\chi' = \frac{\chi_0}{2}\omega_0 T_2 \frac{(\omega_0 = \omega)T_2}{1+(\omega-\omega_0)^2 T_2^2} \tag{3.37}$$

$$\chi'' = \frac{\chi_0}{2}\omega_0 T_2 \frac{1}{1+(\omega-\omega_0)^2 T_2^2} \tag{3.38}$$

Therefore, we can define the complex susceptibility by:

$$\chi = \chi' - i\chi'' \tag{3.39}$$

Both χ' and χ'' are solutions to the Bloch equations. They are shown in Figure 3.4 and are often of the format of a Lorentzian line.

3.4 How do we measure a magnetic resonance?

We have seen in the previous sections the behavior of magnetic moments in a static field H_0, and how they behave once a pulse field H_1 is applied perpendicular to H_0. Such pulse field is generated by a coil, inside of which goes the sample. What happens after

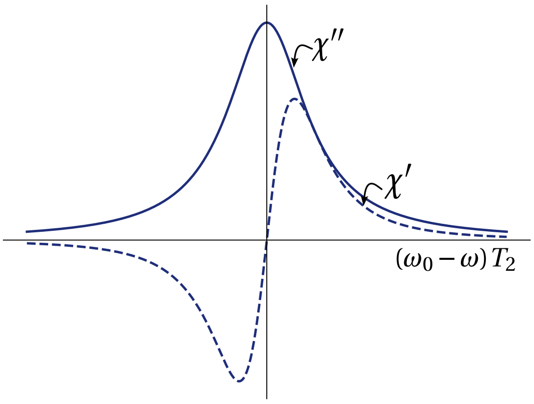

Figure 3.4: χ' and χ'' from the Bloch equations plotted versus $x \equiv (\omega_0 - \omega)T_2$

the pulse is a change in the impedance of the coil due to the resonant absorption of the sample.

If a coil has inductance L_0, after a sample is inserted inside of it, it changes to a new value of:

$$L = L_0[1 + 4\pi\chi(\omega)] \tag{3.40}$$

Since the dynamic susceptibility of the sample is a complex value, not only will there be a change in the magnetude of the flux, but also in its phase. The impedance of the coil can be written as:

$$Z = iL\omega + R \tag{3.41}$$

where R is the resistance of the coil. Substituting Equation 3.40 into 3.41, one gets, after some manipulation:

$$Z = i[L_0\omega(1 + 4\pi\chi'(\omega))] + [R + L_0 4\pi\omega\chi''(\omega)] \tag{3.42}$$

Equation 3.42 shows us that the real part of the susceptibility alters the inductance of the coil, whereas the imaginary part changes its resistance.

Assuming uniform magnetic fields within a volume V, the maximum magnetic energy stored due to an alternating current is:

$$\frac{1}{2}L_0 i_0^2 = \frac{1}{8\pi}H_{X0}^2 V \tag{3.43}$$

where i_0 is the maximum value of the alternating current.

Therefore, the average power dissipated by the nuclei $\overline{P}$ is:

$$\overline{P} = \frac{1}{2} I_0^2 L_0 \omega 4\pi \chi'' \Rightarrow \tag{3.44}$$

$$\overline{P} = \frac{1}{2} \omega H_{X0}^2 \chi'' V \tag{3.45}$$

This gives a simple connection between the power absorbed, χ'', and the intensity of the pulse field H_1.

3.5 Spin echoes

Finally, to end this chapter on the basis of nuclear magnetic resonance, we must explore the notion of **spin echo** (or **Hahn echo**, named after the physicist who discovered the phenomenon), which builds the grounds for the pulse methods in NMR, used in the experiments of this thesis.

Suppose a $\pi/2$ pulse is applied to a group of spins to observe the Free Induction Decay (FID) signal. From the Bloch equations, we know that the FID signal decays exponentially with a time constant T_2. Due to this decay, the resonance line for solids typically has a width of several Gauss. This results from the inhomogeneity within the sample, which causes the spins to precess at different rates, leading to them getting out of phase with one another. Consequently, the FID signal decreases in intensity, as it is the sum of all contributions from different parts of the sample.

Erwin Hahn made the groundbreaking discovery that, if a π pulse is applied at a time τ after the first pulse, a second FID signal appears at a time 2τ after the initial pulse [53]. He named this new signal the "spin echo." The emergence of this signal indicates that the π pulse refocuses the spins, causing them to realign and return to phase. This discovery became a powerful tool for measuring line widths much narrower than those caused by magnetic inhomogeneity, which is particularly useful in solids.

This refocusing pulse is referred to as a $\pi/2-\pi$ pulse and was first introduced by Carr and Purcell in 1954 [54]. Consider a set of spins initially aligned in the z-direction by a static magnetic field $\boldsymbol{H}$ (Figure 3.5a). At time $t = 0$, a rotating magnetic field H_1 is turned on, which must be in resonance with both the static field H_0 and the Larmor frequency of the nuclei (remember the golden rule: $\omega = \gamma H_0$). By adjusting the pulse duration t_p appropriately, the spins are tilted into the $x-y$ plane, generating a $\pi/2$ pulse (Figure 3.5b). Over time, the spins lose coherence and begin to precess at different rates. After a time $t = \tau$, the magnetization δM of a small portion of the sample will shift from the $-y$-direction by an angle θ such that:

$$\theta = \gamma \delta H \tau, \qquad \delta H = H - H_0, \tag{3.46}$$

where δH is the inhomogeneity in H. This is represented in Figure 3.5c. Now, we apply a pulse π at a time $t = \tau$ (Figure 3.5d). Again the magnetization will advance through an angle θ, bringing it to a position aligned with the $y-$axis at $t = 2\tau$ (Figure 3.5e).

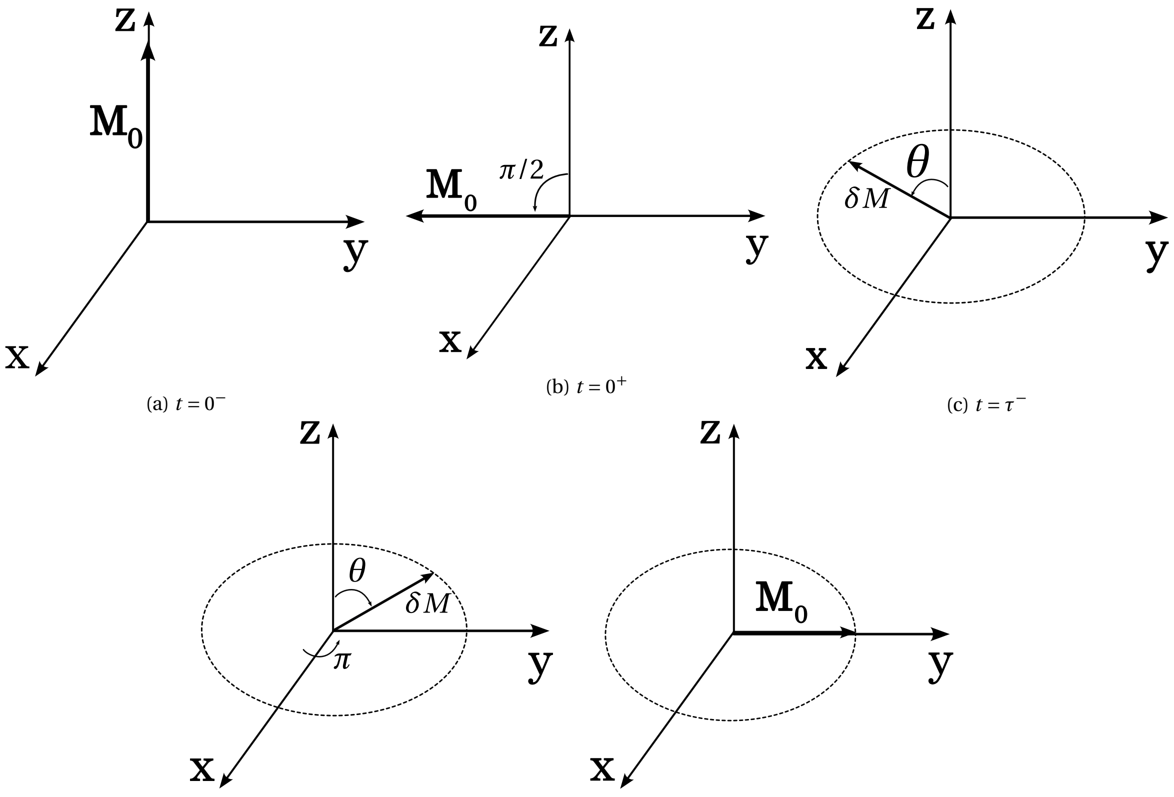

(a) $t = 0^-$ (b) $t = 0^+$ (c) $t = \tau^-$

(d) $t = \tau^+$ (e) $t = 2\tau$

Figure 3.5: The formation of a spin echo using a $\pi/2 - \pi$ pulse sequence, as observed in the rotating reference frame: a) At $t = 0^-$, the magnetization M_0 is in thermal equilibrium and lies along the z-direction. b) Immediately after the $\pi/2$ pulse, the magnetization is rotated into the $x - y$ plane. c) An element of magnetization δM precesses at a different rate due to magnetic field inhomogeneity, resulting in an extra angle θ between different portions of the sample. d) The application of the π pulse refocuses the magnetization by reversing the precession direction, aligning the spins that were out of phase. e) At a time 2τ, all elements of the magnetization have refocused and are aligned along the $+y$-direction.

Although the spins are in phase at this moment, they will gradually get out of phase again due to the field inhomogeneity, causing the free induction signal to decay once more. The final form of the pulse sequence and the resulting echo signal are shown in Figure 3.6. Note how the shape of the echo at $t = 2\tau^+$ is symmetric to its shape at $t = 2\tau^-$.

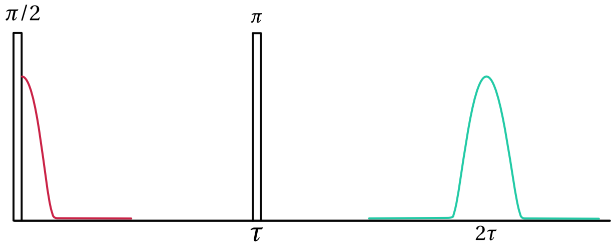

Figure 3.6: The decay of the echo (green) from $t = 2\tau$ onward follows the same time dependence as the free induction decay signal (pink) from $t = 0^+$ onward. It is important to note that the buildup of the echo before $t = 2\tau$ is the mirror image in time of the decay after $t = 2\tau$. Additionally, no FID signal is produced immediately following the π pulse.

3.6 Nuclear Hamiltonian

We end this chapter by exploring the interactions of the nuclei in the case of solids. The complete Hamiltonian can be written as:

$$\hat{\mathscr{H}}_{\text{nuc}} = \hat{\mathscr{H}}_Z + \hat{\mathscr{H}}_{\text{hf}} + \hat{\mathscr{H}}_Q + \hat{\mathscr{H}}_{\text{n-n}} \tag{3.47}$$

This Hamiltonian takes into account both magnetic and electronic interactions in the crystalline lattice.

The first term is the Zeeman interaction, already mentioned in the beginning of the chapter, which arises in the presence of an applied magnetic field. It is defined as:

$$\hat{\mathscr{H}}_Z \equiv g\mu_n \hat{I} \cdot \boldsymbol{H_0}, \tag{3.48}$$

where $g\mu_n \boldsymbol{I} = \boldsymbol{\mu}$ is the magnetic moment of the nucleus.

The second term in Equation 3.47 is the hyperfine interaction between the unpaired electrons and the neighbouring nuclei. Thus:

$$\hat{\mathscr{H}}_{\text{hf}} \equiv \hat{I} \cdot \overleftrightarrow{A}_{\text{hf}} \cdot \hat{S}, \tag{3.49}$$

where $\boldsymbol{I}$ and $\boldsymbol{S}$ are the nuclear and electronic spins, and $\overleftrightarrow{A}_{\text{hf}}$ is the hyperfine coupling constant for their interaction.

3.6.1 Knight shift

It is convenient to rewrite both of these terms as:

$$\begin{aligned}
\hat{\mathscr{H}}_Z + \hat{\mathscr{H}}_{\text{hf}} &= \mu_0 \gamma (1+K) \hat{I} \cdot \boldsymbol{H_0} && (3.50)\\
&= \mu_0 \gamma (1+K) \hat{I} \cdot \boldsymbol{H_0} && (3.51)\\
&= \mu_0 \gamma \hat{I} \cdot \boldsymbol{H}_{\text{eff}} && (3.52)
\end{aligned}$$

where $H_{\text{eff}} = (1+K)H_0$ is an effective field the nuclei experiences and K is the **Knight shift**. It takes into account both the Zeeman effect and the hyperfine interaction. In NMR this is -a relevant and convenient form for this part of the Hamiltonian-, since the Knight shift is measured directly from the NMR lines.

The Knight shift is named after Walter Knight, who first observed it when performing resonance experiments of ^{63}Cu [41]. He noticed the resonance frequency was 0.23% higher than the frequency observed for CuCl at the same static field. Later on, it was discovered to be a common occurrence for all metals. Such frequency displacement can be written as:

$$\omega_m = \Delta\omega + \omega_d, \tag{3.53}$$

where ω_m is the observed resonance frequency in the metal, ω_d is the frequency for a diamagnetic reference, and $\Delta\omega$ is the observed shift.

The Knight shift exhibits four key properties:

1. $\Delta\omega > 0$ (with rare exceptions);
2. If ω_d is changed by altering the static field, the fractional shift $\Delta\omega/\omega_d$ remains constant;
3. The fractional shift is nearly independent of temperature;
4. The fractional shift generally increases with the nuclear charge Z;

The Knight shift arises from the magnetic field experienced by the nucleus due to the interaction with conduction electrons through the s-state hyperfine coupling. Since these electrons can move between atoms, each nucleus senses a magnetic coupling with many electrons. Thus, one must average the coupling to electron spins over the spin orientation of many electrons. When there is no applied magnetic field, the electron spins do not prefer any specific orientation, resulting in no net magnetic coupling. However, when a static field H_0 is applied, it polarizes the electron spins, creating a nonzero average magnetic coupling to the nuclei. As a result, the effective field at the nucleus increases, as the nuclei experience a magnetic field that is parallel to the magnetic moment (since it is an s-state interaction), and the electron moments are aligned with H_0.

Since the frequency shift is proportional to the degree of electron spin polarization, it is also proportional to H_0 (or ω_d). Additionally, because electron polarization is temperature-independent, the shift is also temperature-independent. Finally, the dependence on nuclear charge arises from the fact that the wave function of the electrons is more spatially extended at the position of a higher Z nucleus. From these observations, it is clear that the hyperfine coupling mechanism can fully explain the properties of the Knight shift. In practice, the Knight shift is measured through the following relation:

$$K = \frac{\omega_m}{\gamma H_0} - 1, \tag{3.54}$$

where ω_m is the observed resonance.

3.6.2 Quadrupolar interactions

A relevant interaction worth mentioning is the **quadrupolar interaction**, which arises from interactions between electrons in the crystalline lattice. It arises only in cases of quadrupolar momentum $\boldsymbol{Q} \neq 0$, spin $I > 1/2$ and reduced site symmetry. Under these conditions, there is an Electric Field Gradient (EFG) which acts on the quadrupolar moment and gives rise to the term $\hat{\mathscr{H}}_Q$ in Equation 3.47.

When a nucleus has spin 1/2, it has a spherical charge distribution and therefore the quadrupolar effects cancel out. This is not the case for $I > 1/2$. Suppose the nucleus is elongated, rather than spherical, and under the influence of the charges shown in Figure 3.7. In Figure 3.7b, we have a lower energy configuration, for the positive nuclear charges are closer to the electric external charges. Thus, there is an electrostatic energy that varies with the nuclear orientation, which splits the m_I degeneracy.

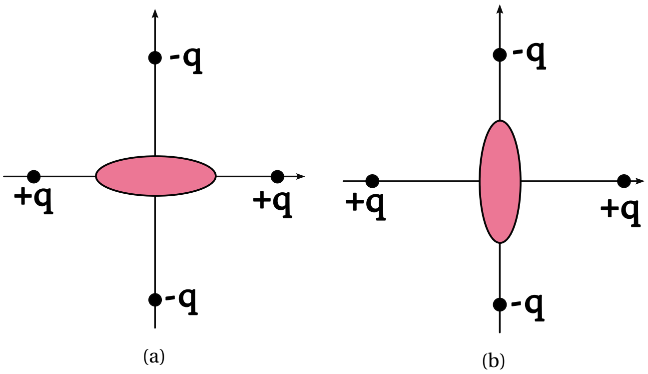

Figure 3.7: a) A cigar-shaped nucleus in the field of four charges, $+q$ on the $x-$axis and $-q$ on the $y-$axis. The configuration of b) is more energetically favorable because it puts the positive charge of the ends of the cigar closer to the negative charges $-q$.

The Nuclear Quadrupolar Hamiltonian can be written as:

$$\hat{\mathscr{H}}_Q = \frac{e^2 qQ}{4I(2I-1)}\left[3I_z^2 - I(I-1) + \frac{\eta}{2}(I_+^2 + I_-^2)\right] \tag{3.55}$$

where the components of the EFG tensor are in the terms $eq = V_{\mathrm{zz}}$ and $\eta = (V_{\mathrm{xx}} - V_{\mathrm{yy}}/V_{\mathrm{zz}})$ and are given by:

$$V_{\alpha\beta} = \frac{\partial^2 V}{\partial x_\alpha \partial x_\beta} \tag{3.56}$$

The term 3.55 is the second order term of the multipolar expansion of the electrostatic interaction between the nuclear charge and the electric charges around the nuclei.

Therefore, in the case of spin $I > 3/2$ nuclei (which is the case for both nuclei studied in this thesis), in the absence of an external static magnetic field, there are two degenerate states available, thus only one transition (i.e., one resonance line), $\pm 3/2 \leftrightarrow \pm 1/2$, is expected. However, in the presence of the Zeeman interaction, there are $2I+1 = 4$ energy levels available, thus three expected transitions: a central resonance transition $(-1/2 \leftrightarrow +1/2)$ and two satellites $(-3/2 \leftrightarrow -1/2$ and $+1/2 \leftrightarrow +3/2)$. Both cases are shown in Figure 3.8.

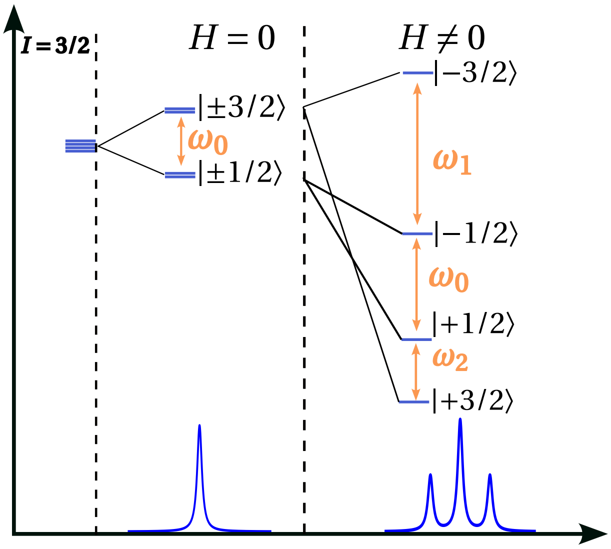

Figure 3.8: The possible transitions for $I = 3/2$. In the first case, $H = 0$, so there is a partial breaking of degeneracy due to the electric field gradient. When the magnetic field is applied, there is the full splitting of the energy into quantum finite energy levels, and all three transitions are observed.

4 EXPERIMENTAL DETAILS

The goal of this chapter is to introduce the reader to the important experimental details regarding the equipments used to acquire the data for this thesis. Before actually performing the NMR experiments, the samples' magnetic properties are studied using SQUID-VSM data, such as magnetic moment as a function of temperature (fixed applied magnetic field) or applied magnetic field (fixed temperature). This is due to the fact that the magnetic susceptibilty (accessible via SQUID) is proportional to the Knight shift (accessible via NMR): $K_{\text{spin}}(T) \propto A_{\text{hf}}\chi_{\text{spin}}(T)$, as well as to give a sense on what is the behavior of the sample especially under high magnetic fields, since that's what we work with in NMR.

4.1 SQUID-VSM

A SQUID-VSM (Superconducting QUantum Interference Device - Vibrating Sample Magnometer) is a device sensible to very low magnetic field changes. It consists of two Josephson junctions, responsible for the signal detection and a superconducting coil to produce very high magnetic fields (up to 7 T). When the sample is in a magnetic field, as weak as it may be, and it is vibrated vertically, this change in magnetic flux is detected by the system, inducing a current in the junctions which is then converted into a measurable voltage and read as electronic signal by the computer. This setup yields extremely sensitive results, up to 10^{-6} emu. Besides, the cryostat allows temperatures from 1.8 K to 400 K. The SQUID-VSM used in our laboratory can be seen in Figure 4.1:

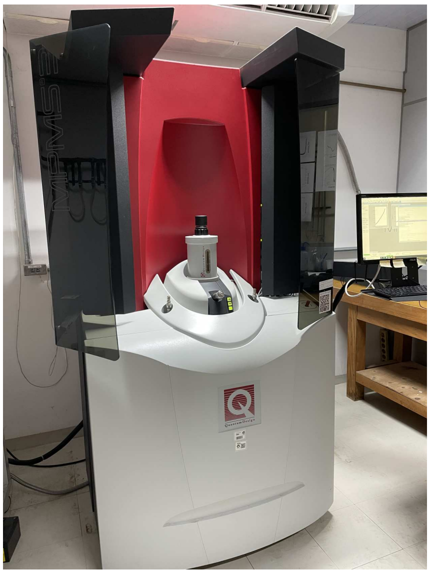

Figure 4.1: SQUID-VSM experimental setup.

The experiments performed in the SQUID-VSM consist of two magnetization curves as a function of temperature (denoted by M *vs.* T or simply M(T)), one in H = 25 Oe and the other in 7 T, as well as a magnetization as a function of applied magnetic field, M(H). With the first two curves, one aims to learn the critical temperature (T_c) of the Superconducting sample, both in "zero field" and in high magnetic field. This allows for more precise and attentive measurements around the transition temperature during the NMR experiments, since most parameters change in this temperature range. From the last curve, one learns about the behavior of the magnetization under different fields, which is of high importance in the case of superconductors.

4.2 NMR Experimental Setup

A typical NMR setup involves a handful of equipments and a complex NMR spectrometer. The aim of this section is to familiarize the reader with the essencial steps that precede the experiment, as well as to unravel details on the NMR spectrometer used.

The full setup involves the following components:

- A Superconducting magnet, capable of producing strong and stable magnetic fields;
- A probe, which allows the coil to produce the RF pulses and receive the signal created by the sample;
- A RF transmitter to produce such pulses;
- A receiver to amplify the NMR signals;
- An ADC to convert the incoming electronic NMR signal into digital form, to be processed by the computer;
- A "pulse programmer" to produce such RF pulses and delays.

The setup used throughout this thesis is available at the Gleb Wataghin Institute of Physics, in the laboratory of Prof. Dr. Ricardo R. Urbano. The setup is shown in Figure 4.2.

In the following pages, these components will be further explored.

4.2.1 The Pick-up Coil

In NMR experiments, one wants to perform spin echoes sequencies and relaxation times measurements. For both of them, it is necessary to align the spin population in a given axis (using an external field H_0) and then tilt them to different axes or planes. This can be achieved by applying, shortly, a perpendicular magnetic field, called H_1, which is generated by passing a current through a pick-up coil, inside of which goes the sample.

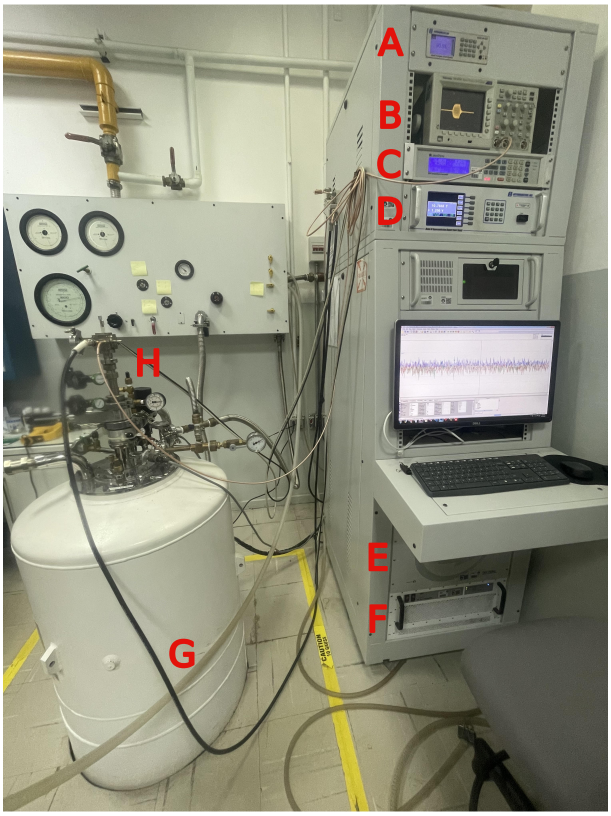

Figure 4.2: NMR system. A: LHe level monitor from the magnet dewar (Cryomagnetics model LM-510). B: Osciloscope (Tektronix, Inc. model TDS3052C). C: Temperature controller (Lakeshore, Inc. modelo 336). D: Magnet current source (Cryomagnetics, Inc. 4G Superconducting Magnet Power Supply). E: NMR spectrometer (TecMag, Inc. Redstone model). F: Power amplifier (Tomco, Inc. Alpha model) G: Cryostat (Janis, Inc.). H: Magnet dewar (Cryomagnetics, Inc.-12 T).

Then, when the spins are going back to their original position, they induce a RF signal in the pick-up coil, which in turn is processed as an electronic signal and read by the computer software.

It is said that NMR experiments begin with the pick-up coil. First of all, each nucleus has a different gyromagnetic ratio; therefore, studying different nuclei requires different pick-up coils for each. (remember the golden rule: $\omega = \gamma H$). Thus, in this preliminary part, one must think of the frequency range or the magnetic field that one is going to work with. There are some relevant parameters of the pick-up coil to bear in mind when making it for the experiment: number of turns, thickness of the wire used (generally, copper wires) and diameter of the coil.

The frequency of the coil is inversely proportional to the number of turns. The thickness of the wire and the coil's diameter are relevant when thinking of the filling factor: the smaller the sample, the smaller the coil should be, in order to make sure H_1 is perfectly aligned with the sample. Additionally, when a large number of turns is required, it is best to work with a thinner wire, so that the coil won't be too long (and the filling factor remains optimal). Moreover, a flat coil is the best form to further increase the filling factor when working with single crystals or extremely small samples.

In this work, two samples were studied: MgB_2 and $BaFe_{1.92}Co_{0.08}As_2$. For both of them, flat coils were used, however different number of turns were made for them:since we probed ^{11}B and ^{75}As nuclei, their gyromagnetic ratios are 13.6552 MHz/T and 7.2919 MHz/T respectively.

For ^{11}B experiments, the coil used is presented in Figure 4.3, as well as the single crystal used. The number of turns used was - , freq - and mag field -

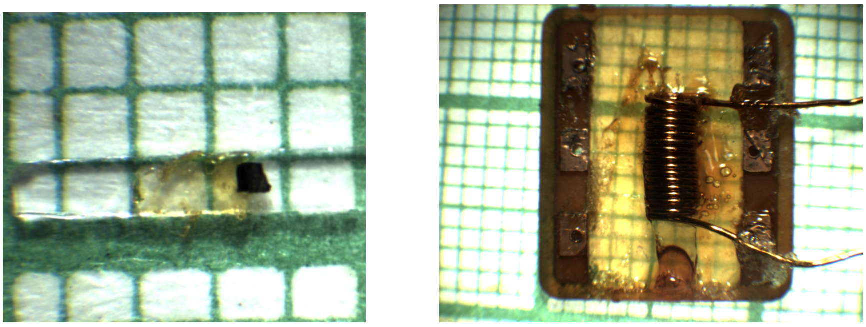

(a) (b)

Figure 4.3: a) MgB_2 single crystal. b) Pick-up coil used in ^{11}B experiments.

For ^{75}As experiments, the coil and the sample are in Figure 4.4. The magnetic field was of 10.78 T and the frequency of the tank circuit was 78.35 MHz.

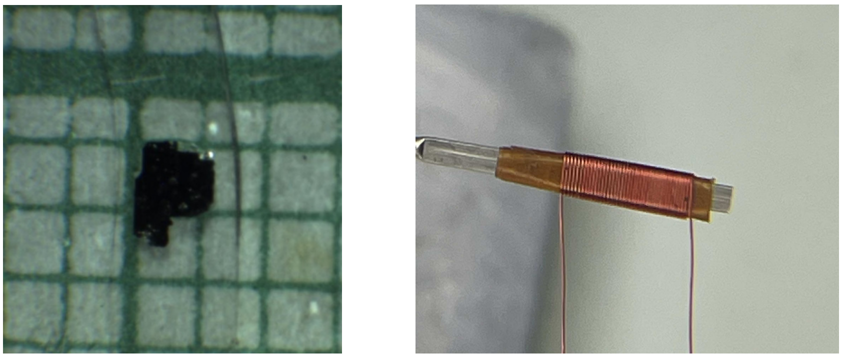

(a) (b)

Figure 4.4: a) $BaFe_{1.91}Co_{0.9}As_2$ single crystal. b) Pick-up coil used in ^{75}As experiments.

4.2.2 The Experimental Setup and its parts

The NMR Probe

The probe used in our equipment consists of two capacitors (one for tuning and one for matching) of variable capacitances and the coil. Together, they form an RLC circuit (Figure 4.5), or tank circuit, whose frequency ω_c has to be the same as the Larmor frequency of the studied nucleus (resonance condition). Thus, one aims at making the coil with the number of turns needed to vary the capacitance as little as possible. This is important when working with low temperatures as it makes the resonance frequency shift considerably. Since we cannot change the number of turns (inductance) of the coil mid-experiment, one must vary the capacitance to make up for the changes in resistivity and inductance induced by low temperatures.

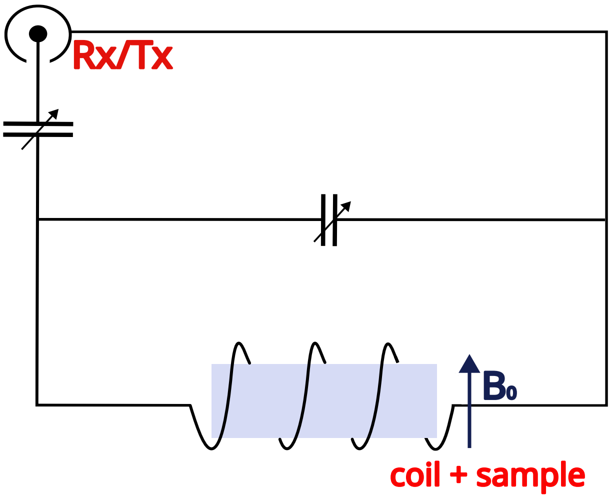

Figure 4.5: Tank circuit of the NMR probe.

After the coil is prepared, its ends are soldered to the probe and properly aligned in regards to the applied magnetic field using a goniometer. A picture of the coil on the probe is in Figure 4.6.

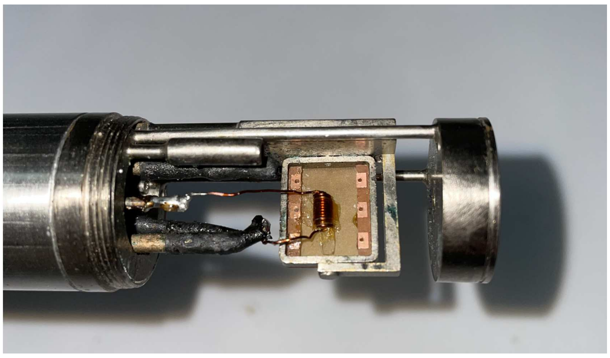

Figure 4.6: NMR coil with the sample inside, soldered to the probe.

Cryostat and Magnet

In Figure 4.2, one can see the NMR setup present in the LaRMNuQ at IFGW, where all the NMR data were acquired.

The cryostat available at IFGW, Unicamp is a JANIS open cycle ^{4}He dewar, combined with a superconducting magnet (made of NbTi) that produces magnetic fields as high as 12.1 T. For the magnet to produce such fields, it is kept in a liquid Helium (LHe) bath.

To change the temperature of the sample, one uses the needle valve which gives access from the helium bath to the sample chamber. The temperature is then controlled with a Lakeshore Temperature Controller, but it is still very important to control the LHe flow with the needle valve: for low temperatures, the flow cannot be too low, whereas for high temperatures, a large flow might cause the temperature to oscillate considerably.

The NMR spectrometer

Figure 4.7 shows the main components of a NMR spectrometer. First of all, a synthesizer is used as a source of RF waves with well-defined frequencies and is capable of making phase shifts, necessary for detection. Since the RF is applied for a short period of time, there is a gate on the output of the synthesizer.

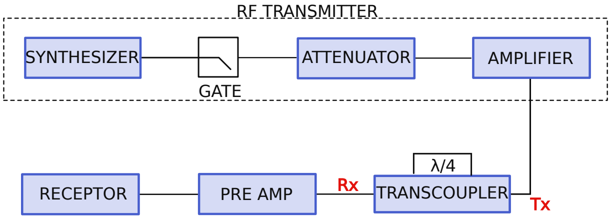

Figure 4.7: Main components of a NMR spectrometer. Image adapted from Ref. [55]

The source produces low power signals (~mW), so it is necessary to amplify them so the H_1 field has a minimal amplitude for detection (~100 W).

On the other hand, when the RF power is applied, a high voltage is generated across the capacitor. It may be high enough to generate a discharg or arc, and this probe arcing can damage the coil and the capacitor. In order to avoid this, an attenuator comes in hand between the synthesizer and the amplifier. It allows for the choice of power of the RF signal sent to the probe.

The NMR signal coming from the coil is rather small ($\sim \mu$V), so one uses a pre amplifier to boost the signal and allow its digitalization. Moreover, the coil needs to generate the H_1 field and to pick up the signal originating from the relaxation of the nuclear magnetic moments. The applied pulse (~10-100 W) cannot be sent to the receptor, which is quite sensitive. Therefore, the separation of these signals is performed by the transcoupler.

Furthermore, an ADC (analogue to digital converter) converts the NMR signal (voltage) in a binary code which can be stored as computer memory. It discretizes the NMR signal in order to have a set of equally-spaced points. The interval between points is called dwell time (denoted by d_t).

One question that arises at this point is how long this interval can be, in order not to miss information of the wave form. The dwell time is the highest frequency which can be represented correctly:

$$f_{max} = \frac{1}{2d_t} \tag{4.1}$$

Moreover, we can distinguish between positive and negative frequencies, so a dwell time of d_t means we can represent correctly frequencies in the range $-f_{max} \leq f \leq f_{max}$.

Another problem that arises at this point is the fact that typical NMR frequencies are of the order of hundreds of MHz. However, there are no available ADC to work fast enough to digitize accurately such a waveform. The solution to this is using a mixer as to mix down to a lower frequency.

The mixer uses an artificially generated signal (local oscillator) and the NMR signal. It sums and substracts them in a way that we are left with a much lower frequency (which is called the *receiver frequency*). One of the inputs of the mixer is generated locally by a synthesizer and is called *local oscillator*. The other input is the NMR signal from the probe. The summed frequency will be much larger than the subtracted frequency, therefore it will be filtered by a low pass filter and only the subtracted one will the passed to the ADC.

Lastly, one needs to separate between the negative and positive frequencies that arrive at the ADC. To achieve this, the method of quadrature detection is used. Figure 4.8 illustrates the problem. In order to be able to distinguish between positive and negative frequencies, one needs to know both the x and y components of the magnetization. One way to detect different components is to have two coils, one in the x axis and the other in the y axis. However, in practice this would be very challenging to achieve, so this calls for an easier alternative: two separate mixers, where the phase of one is shifted by 90 °relative to the other.

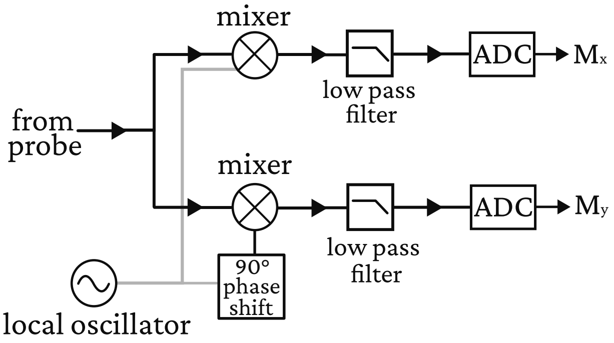

Figure 4.8: Schematic of the arrangement for quadrature detection.

From Figure 4.8, one can see that there is a phase shift before one of the mixers. Suppose that the siginal coming from the probe can be written as $A\cos(\omega_0 t)$, where ω_0 is the Larmor frequency, whereas the local oscillator signal is given by $\cos(\omega_{rx} t)$. Multiplying both signals yields the following output for the upper mixer in Figure 4.8:

$$A\cos(\omega_0 t)\cos(\omega_{rx} t) = \frac{1}{2}A[\cos(\omega_0 + \omega_{rx})t + \cos(\omega_0 - \omega_{rx})t] \tag{4.2}$$

After the low pass filter, only the subtraction term $\cos(\omega_0 - \omega_{rx})t$ survives. Thus, the signal takes the form of a cosine modulation; it is the same as detecting the x component of the magnetization in the rotating frame.

On the other hand, if there is a 90 °before the mixer, this is the same as saying that the local oscillator signal is $-\sin(\omega_{rx} t)$. Thus, the mixer's output is now:

$$A\cos(\omega_0 t) \times -\sin(\omega_{rx} t) = \frac{1}{2} A[-\sin(\omega_0 + \omega_{rx}) t + \sin(\omega_0 - \omega_{rx}) t] \tag{4.3}$$

Note how the difference frequency term is sine modulated at the offset frequency: it is the same as the y component in the rotating frame. Thus, one can distinguish between x and y components of the magnetization in the rotating frame simply by shifting the phase of the local oscillator signal.

5 BCS SUPERCONDUCTOR: MgB_2

In this Chapter, we will present our data for experiments on MgB_2. The first section explores the most interesting features of this superconductor, such as the two-gap superconductivity. Section 2 displays the magnetization data obtained for several values of applied magnetic field and temperature, as well as the NMR results. First, a NMR spectrum is shown for 4.2 K, which is the first novel result of this thesis, and then a study on anisotropy of quadrupolar effects is displayed in comparison as well. The results of Knight shift are presented, where one can see the T_c and an anomalous Knight shift behaviour below T_c. Lastly, the results for T_1 are shown, where different fits were used on our data. The fact that, in the superconducting state, a two-component T_1 fit is the best match is a strong indication of the two-gap superconductivity in MgB_2.

5.1 What is so interesting about Magnesium Diboride?

Magnesium diboride, although a conventional superconductor, is by no means an ordinary material. When it was discovered, its high $T_c \approx 39$ K in regards to the intermetallic compounds known then sparked great interest of the scientific community. First, it was suspected that its high T_c was evidence for unconventional superconductivity. However, it was observed soon after its discovery that the T_c can be increased when ^{10}B is used instead of ^{11}B, thus pointing to isotope effect. This observation made it clear that in MgB_2 the Cooper pairs bind through electron-phonon interaction and that it is the B electrons that form the Cooper pairs (Figure 5.1 for crystal structure). The BCS mechanism was also observed by experimental techniques such as photoemission spectroscopy [13], neutron scattering [15] and scanning tunneling microscopy (STM) [14].

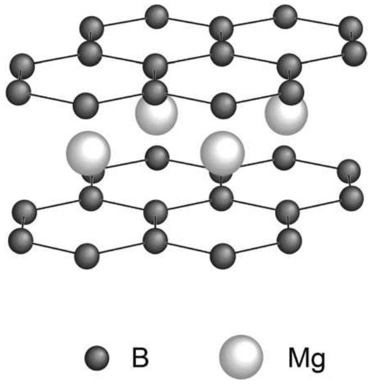

Figure 5.1: Crystal structure of MgB_2.Boron atoms form stacks of honeycomb layers and magnesium atoms are in between the boron layers at the center of the hexagons.

A very interesting aspect of such compound is the presence of two superconducting gap, shown in Figure 5.2. Although such existence was theoretically proposed in 1959 [56], it was not observed until superconductivity was found in magnesium diboride. Normally in a superconductor below T_c, there exists one temperature-dependent energy gap $\Delta(T)$ such that a minimum energy of $2\Delta(T)$ is needed to break a Cooper pair into two quasiparticles. It was observed experimentally that there are two of such gaps in MgB_2, one with $\Delta(0) \simeq 2$ meV and another $\Delta(0) \simeq 7$ meV [57]. Both gaps follow BCS temperature dependency and disappear as the same value of T_c [58], as one can see in Figure 5.2. According to the BCS theory, $2\Delta(0) = 3.53 k_B T_c$, thus making the gaps correspond to two different transition temperatures of 15 K and 45 K, respectively. Nevertheless, the critical temperature of 39 K is due to the finite coupling between these gaps [59].

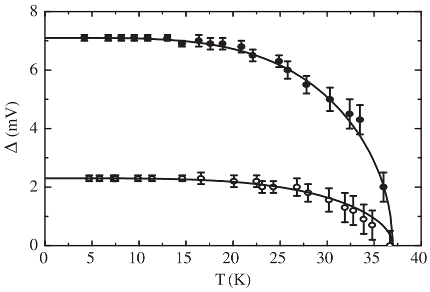

Figure 5.2: Values of the two gaps in MgB_2 extracted from the scanning tunneling spectroscopy as a function of temperature. The lines are the BCS Δ(T). Image extracted from Ref. [58].

The two gaps originate in the σ and π bands of boron electrons [60] (Figure 5.3), and was quickly confirmed experimentally by measurements of specific heat [61], Raman spectroscopy [62], photoemission spectroscopy [63] and STM [64]. Such observation brings a lot of questions to what is known about vortex dynamics in two-band superconductivity. With two coherence lengths and two sets of supercurrents around the vortex core, the concepts of flux pinning, vortex fluctuations and phase diagrams that apply to one-gap superconductors need to be reevaluated.

5.2 Results and Discussions

5.2.1 Magnetization

Initially, we performed magnetization experiments in a SQUID-VSM both as function of temperature ($M \times T$) and applied magnetic field ($M \times H$). The goal was to obtain the critical temperature[1] (for polycrystalline sample, $T_c = 39$ K [65]) before performing the NMR experiments, as well as getting a preview of the single crystals behaviour in higher magnetic fields. The behavior of the MgB_2 single crystal is in Figures 5.4 and 5.6.

---

[1] For both magnetization and Knight shift data, T_c values were obtained by the onset of superconductivity

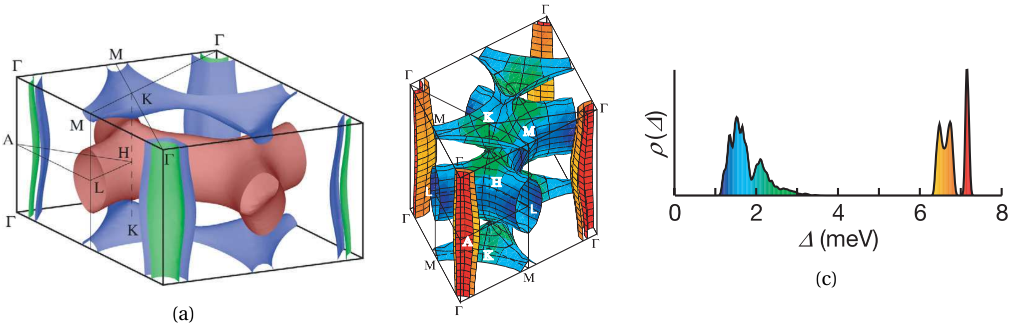

(a)

(b)

(c)

Figure 5.3: a) The Fermi surface of MgB_2 from band structure calculation. Green and blue cylinders (hole-like) are the σ bands, and the blue (hole-like) and the red (electron-like) tubular networks are the π bands. Figure extracted from Ref. [60]. b) The superconducting energy gaps on the Fermi surface for MgB_2 from the band structure calculation. The color scale corresponds to the distribution of gap values shown in c). Figure extracted from Ref. [57].

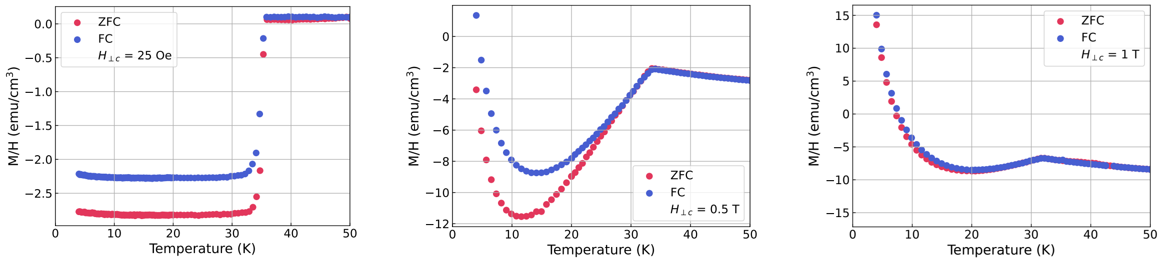

(a) H = 25 Oe

(b) H = 0.5 T

(c) H = 1 T

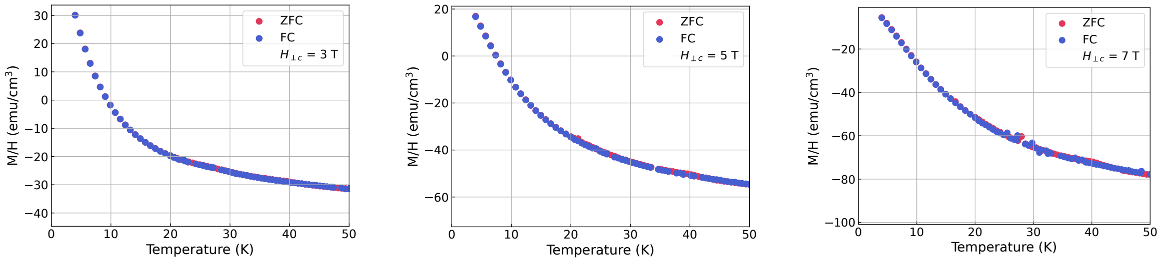

(d) H = 3 T

(e) H = 5 T

(f) H = 7 T

Figure 5.4: Magnetization as function of temperature for several values of applied magnetic field.

For all $M \times T$, it was performed two types of experiments: ZFC and FCC. The zero-field cooling protocol means that the sample was cooled to the lowest temperature (here, 4 K) at zero field, then, the field was turned on and data was acquired as the temperature was swept, up to 50 K (above the critical temperature). On the other hand, the FCC protocol stands for field cooling on cooling: the magnetic field was turned on at 50 K in the normal state, then data acquisition started while sweeping the temperature down to 4 K.

From Figure 5.4, it is clear that $T_c \approx 36$ K at $H = 25$ Oe for our MgB_2 single crystal, quite close to the reported T_c. The small difference between ZFC and FCC lines is a sign of few pinning centers, hence a very clean sample. Once the magnetic field was increased, one can note the arising of a paramagnetic-like effect. With magnetic fields $H = 0.5$ T and $H = 1$ T, one can still see the onset of superconductivity despite de increase of the magnetization below this temperature, but not for $H \geq 3$ T. These values of T_c are plot together in Figure

5.5 with data from Ref. [66], as well as data previously acquired by the author from another batch during her undergraduate studies. We can see that our data are in good agreement with what was published for single crystals, and similar parameters were obtained from the fit for H_{c2}. The following equation was used:

$$H_{c2}(t) = H_{c2}(0)[1-(T/T_c)^{\alpha}]^{\beta} \tag{5.1}$$

where T_c is the critical temperature and $H_{c2}(0)$, α and β are fit parameters. Table 1 presents the parameters for data in Ref. [66] and for our data.

Parameters	**Ref. [66]**	**This work**
$H_{c2}(0)$ (T)	14.3(1)	14.1(3)
α	1.82(4)	1.83(5)
β	1.28(5)	1.35(6)

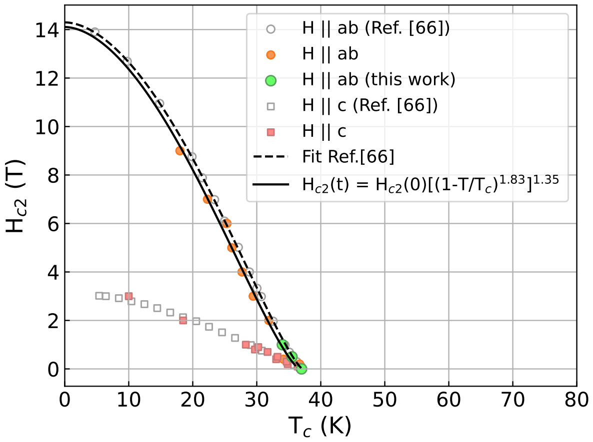

Figure 5.5: Critical fields H_{c2} as function of T_c. The light gray dots are data extracted from Ref. [66], the pink and orange dots are data from the author using another batch (during undergraduate studies) and the green dots are T_c obtained from Figures 5.4.

The same phenomenon was observed for the $M \times H$ curves, presented in Figure 5.6, where the superconducting hysteresis loop is overcome by a magnetic distribution. At 4 K (Figure 5.6b), one can see that for lower fields, there is a superconducting hysteresis loops, with the same shape as Ref. [66] (Figure 5.7). Nevertheless, at 100 K (Figure 5.6c), there is no observable ferromagnetic hysteresis loop that could explain the behaviour observed for higher magnetic fields.

The origin of this unexpected effect at higher magnetic fields could be associated with some contamination of the sample in the process of high pressure synthesis. The sample can contain some elements which are paramagnetic and their response to strong magnetic fields can overcome the superconducting transition, leading to the data observed. On the other hand, a strong piece of evidence against the contamination hypothesis is the similarity in the hysteresis loop observed in Figure 5.6b and previously reported data for

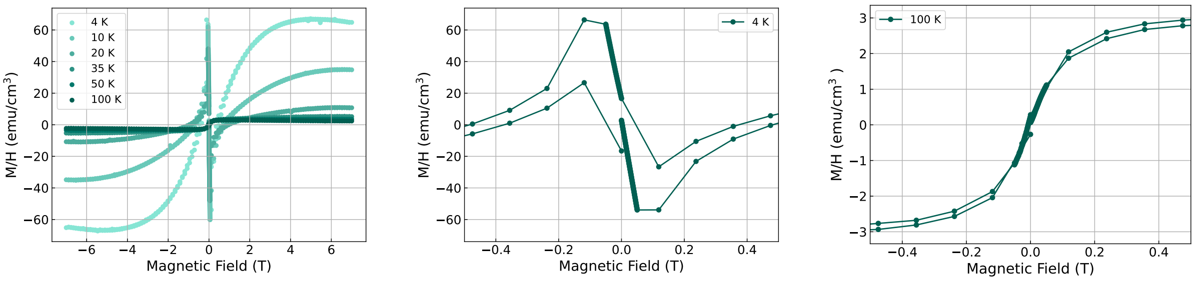

(a) (b) (c)

Figure 5.6: a) Magnetization as a function of magnetic field for several values of temperature. Close-up visualization of magnetization for b) 4 K and c) 100 K, for low values of applied magnetic field.

MgB_2 single crystals (Figure 5.7), which corresponds to samples grown by a different research group. Since these single crystals were produced independently, this consistency strongly suggests that our sample is indeed clean.

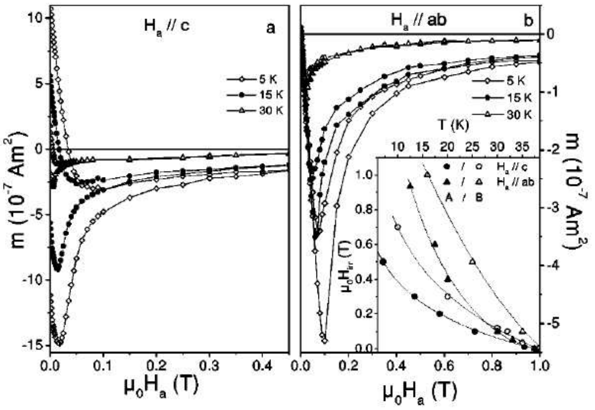

Figure 5.7: Hysteresis loops of sample A for a) H||c and b) H||ab. Inset: Irreversibility line of samples A and B for H||c and H||ab. Figure extracted from Ref. [66]

5.2.2 NMR Results

Starting with the NMR experiments, a full spectrum was obtained for MgB_2 at 4.2 K, the first novel result of this work, presented in Figure 5.8. As stated previously, this is the first observation of the superconducting state by NMR in MgB_2 single crystals. An aspect worth mentioning at this stage is that the lines observed were extremely narrow, which is a strong indication of the high quality of these samples, as defects can alter and broaden the line shape.

The NMR probe used is ^{11}B nuclei, which has spin $I = 3/2$ in hexagonal symmetry (Figure 5.9b). Thus, electric quadrupolar effects arise besides the Zeeman interaction, resulting in two extra resonance lines, which we call satellite lines (SL). Therefore, three transitions are expected, with frequencies given by Equation 5.2:

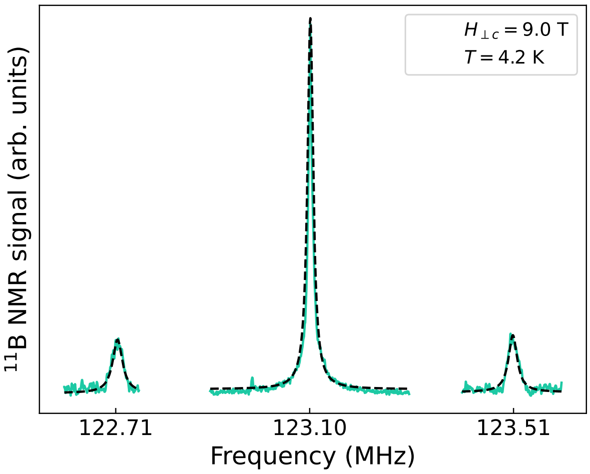

Figure 5.8: Full NMR spectrum for $\theta = \pi/2$ ($H_0^{\perp c} = 9.0$ T). The solid green line is the spectrum, whilst the dashed line is a Lorentz fit using Equation 5.4

$$\nu_{m\leftrightarrow m-1} = ^{11}\gamma(1-K)H_0 + \frac{\nu_{zz}}{2}(m-1/2)(3\cos^2(\theta) - 1 + \eta\sin^2(\theta)\cos(2\phi)) + \mathcal{O}^2 \tag{5.2}$$

where the first term is the effective magnetic field H_{eff} and K is the Knight shift. The second term is the first order quadrupolar shift for the allowed transitions ($\Delta m \pm 1$), η is the asymmetry parameter of the electric field gradient (EFG). Since it is an hexagonal lattice (C6 symmetry), $\eta = 0$.

By plotting both spectra in different orientations and fitting $\nu_{m\leftrightarrow m-1}$ in Equation 5.2, we get the quadrupolar frequency: $\nu_{zz} = \nu_Q = 0.825(5) MHz$, which is the frequency difference between the CL and the SL when $\theta = 0$ (Figure 5.9). This difference is exactly half for $\theta = \pi/2$, just as expected, and confirms the aligning of the single crystal with the magnetic field. This value of quadrupole frequency has also been observed in a work by Strässle et al. [67], which performed a study on the normal phase of MgB$_2$ single crystals. Both results on single crystals are also in good agreement with ^{11}B NMR experiments performed on powder samples [68–72]. Moreover, the fact that the quadrupolar frequency in our superconducting samples is the same as the one found in normal state samples, we can conclude that there no significant changes in the lattice parameters in the superconducting state.

Since the quadrupolar frequency is a footprint of the interactions of the probing nuclei with the surrounding electrons and external magnetic field, any significant changes in the sample structure, such as defects, would induce major changes in the NMR spectrum. The fact that our quadrupole frequency agrees well with the data on polycrystalline and single crystals makes it safe to assume there is no contamination in the sample.

After full spectra in both orientations were obtained, a detailed measurement spanning from 4.2 K to 50 K was performed. This way, one can clearly see the superconducting transition from both the resonance frequency shift (the Knight shift explained in

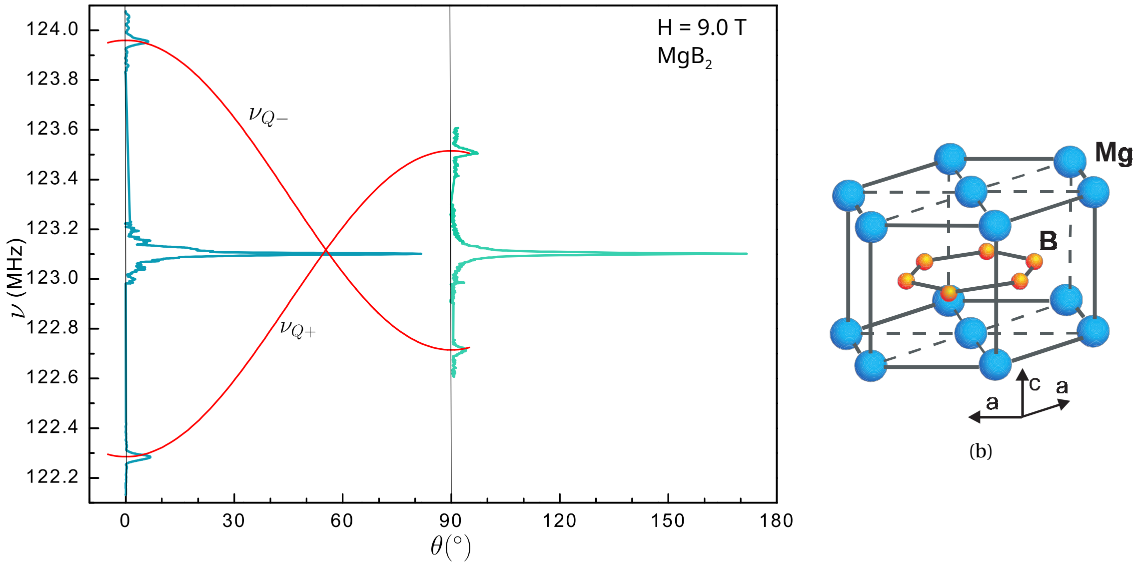

(a)

(b)

Figure 5.9: a) Joint plot of NMR spectra for both H||c ($\theta = 0$) and H⊥c ($\theta = \pi/2$), at 4 K. The red lines are the functions for Eq. 5.2, where ν_{Q-} is $\nu_{m\leftrightarrow m-1}$ for m = -1/2 and ν_{Q+} is $\nu_{m\leftrightarrow m-1}$ for m = +1/2. b) Crystal structure of MgB$_2$. Image adapted from [73]

Chapter 3), as well as the NMR line width broadening. For this purpose, only the central line (CL, transition $-1/2 \leftrightarrow 1/2$) was measured. Both ZFC and FCC procedures were performed, to compare to the SQUID-VSM data. For this part of the experiment, the field is always perpendicular to the c-axis, H⊥ c, due to the fact the upper critical field H_{c2} is greater in this orientation than in the other. For MgB$_2$, the anisotropy factor is: $\gamma = H_{c2}^{\perp c}/H_{c2}^{||c} = 4.6$ [66]. Therefore, working in the perpendicular direction allows us to apply higher magnetic field and still remain in the interval $H_{c1} < H_0 < H_{c2}$.

The Knight shift is calculated from the resonance frequency ω and the static magnetic field H_0:

$$K = \frac{\omega}{\gamma H_0} - 1 \tag{5.3}$$

Since the Knight shift is proportional to the magnetic susceptibility, $K \propto A_{\mathrm{hf}}\chi_s(0)$, the nucleus frequency must follow the same behaviour as the spin susceptibility (and the magnetization). The Knight shift data are in Figure 5.10a.

At this point, we want to obtain the critical temperature by measuring the Knight shift through the transition. From Ref. [66], we know that $T_c \approx 18K$ for a magnetic field $H_0^{\perp c} = 9.0$ T. Thus, around this value, the temperature step was of 2 K, whereas in the normal phase it was 5 or 10 K. Through Figure 5.10a, we see the onset of the Knight shift at 18 K. Nonetheless, the Knight shift increases below this temperature, instead of decreasing as would be expected for a superconducting transition. Still, this transition is much sharper and clearer than in the SQUID-VSM experiments. This is one of the advantages of NMR technique: by probing the specific nuclear susceptibility rather than the bulk susceptibility, one

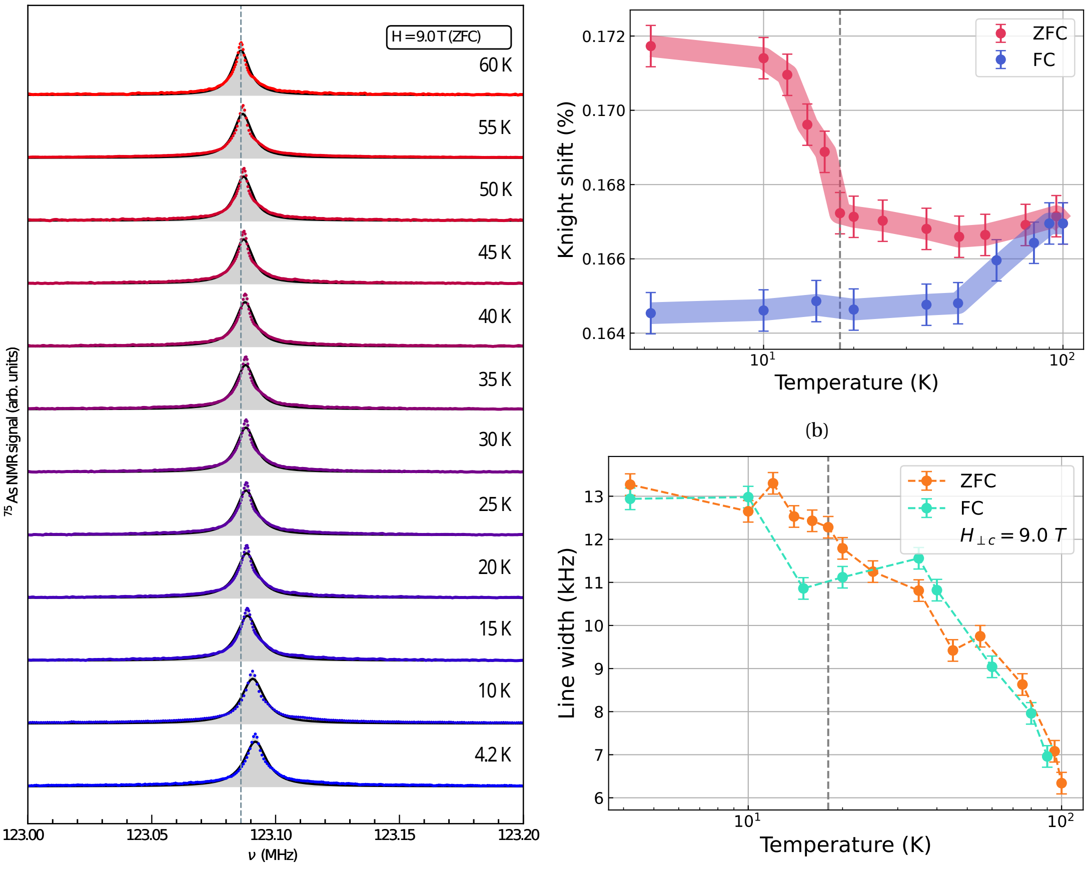

(a)

(b)

(c)

Figure 5.10: a) Central line Knight shift (ZFC), at $H_0^{\perp c} = 9.0$ T, from 4.5 K to 60 K. The dashed line is the resonance frequency for the normal state, 60 K. The black line is a Lorentzian fit, whereas the coloured dots are the NMR data. b) Knight shift as a function of temperature. The onset of K marks a transition. The dashed line at 45 K represents another possible transition. c) Line width w (obtained from Equation 5.4) as a function of temperature.

can gather more precise and detailed information about the nuclei.

Moreover, the Knight shift for 60 K (normal state) and 4.5 K (SC state) present a slight difference, as one can see in Figure 5.10a. For 4.5 K, $\omega = 123.0918$ MHz, whereas for 60 K, $\omega = 123.086$ MHz. Besides the change in the frequency, one can see that the line at 4.5 K is broader than the line at 60 K: the first is 13 kHz, whereas the latter is 8 kHz. In order to obtain such parameters, a Lorentzian fit was performed for the central line for each temperature:

$$y(x) = \frac{2A}{\pi} \frac{w}{4(x - x_c)^2 + w^2}, \tag{5.4}$$

where A is the area under the curve, w is the full width at half maximum and x_c is the resonance frequency.

The line broadening (Figure 5.10c) can be explained by the internal magnetic field distribution. As explained in Chapter 3, in the mixed state of type-II superconductors, the magnetic field is able to penetrate the material through quantum flux, arranged in a triangular pattern (in most cases). Therefore, the vortices can change the line shape and width, which can be seen in NMR experiments and the Knight shift. This is one of the objectives of this project.

Although there was a line broadening throughout the transition, there was no significant line distortion as usually is observed for superconductors. This is an indication of extremely clean sample, where there aren't many defects to act as pinning centers for the vortices. Thus, the vortices are moving, in a flux flow regime, which accounts for the very narrow NMR lines and low intensity magnetic field distribution. This also leads to low critical currents, which explains why the superconducting loop wasn't that pronounced in Figure 5.6.

Lastly, the spin-lattice relaxation rate experiments are presented in Figure 5.11. Each point in Figure 5.11b was obtained through saturation recovery experiments, meaning that a saturation pulse ($\pi/2$) was applied prior to the spin-echo pulse sequence. Between them, there is a new time variable called T_1, and by varying this time (between 1 s and 2400 s in the case of Figure 5.11), one obtains the curve from such Figure.

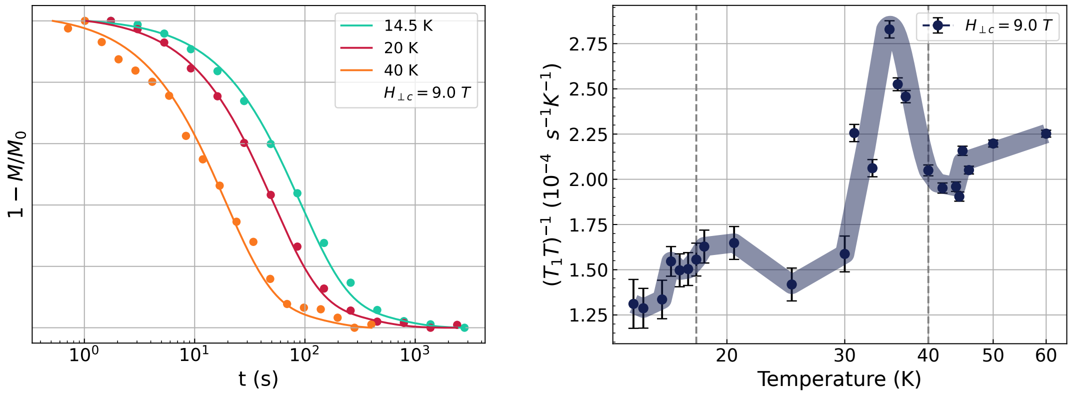

(a)

(b)

Figure 5.11: Normalized nuclear magnetization curves of ^{11}B for MgB_2 our single crystal at 14.5 K, 20 K and 40 K a) Example of $1 - M/M_0$ × t obtained through saturation recovery procedure. This way, one can see how well the single-component fit (Equation 5.5) matches the data. b) $(T_1T)^{-1} \times T$ to verify the Hebel-Slichter peak.

The following function is used to fit T_1 for $I = 3/2$:

$$M(t) = (1 - f)\left[0.1\exp(-t/T_1) + 0.9\exp(-6t/T_1)\right] \tag{5.5}$$

where $f = 1 - M_\infty/M_0$, M_∞ is the maximum value of the magnetization and M_0 is the lowest value [74].

The first aspect that stands out from these data is the extremely long T_1 values observed in our single crystals. Whereas for published data on polycrystalline samples, $(T_1T)^{-1}$ was of the order of 1 $s^{-1}K^{-1}$ [71, 75], for our sample it is of the order of 10^{-4} $s^{-1}K^{-1}$. This is another indication that our samples are extremely clean, have few defects and few pinning centers, leading to few relaxation mechanisms that make the spins return to the equilibrium position.

Furthermore, this is the first observation of T_1 for MgB_2 single crystals in both normal and superconducting phases. For polycrystalline samples, a tiny coherence peak in the SC state was observed [75]. However, performing such experiment on powder samples may not lead to such observation [76], precisely due to the powder's random orientation with regards to the applied field and the strong critical field anisotropy. Therefore, our results show clearly the high quality of the single crystals and a well defined transition followed by the Hebel-Slichter peak.

Moreover, there are two anomalies observed in the spin-lattice relaxation rate, $(T_1\mathrm{T})^1$. The more pronounced one occurs below 40 K, which is exactly the critical temperature for zero field. The less pronounced one appears around 20 K, which is near the critical temperature for $H_0^{\perp c} = 9.0$ T, the applied magnetic field for T_1 measurements. Therefore, we conclude that this is an observation of the Hebel-Slichter peak expected for a BCS Superconductor.

Another possibility that arises in this scenario is that T_1 experiments performed on a high-quality single crystal could probe both the superconducting gaps present in MgB_2. From STM experiments, such gaps are of energies $\Delta(0) \approx 2$ meV and $\Delta(0) \approx 7$ meV. Therefore, there are two distinct T_c of 15 K and 45 K, respectively [77]. The finite coupling between the two gaps results in a single T_c of 40 K [59]. Following these steps, it is likely that both superconducting gaps and their transitions were probed through spin-lattice relaxation rates.

In light of the observation of two different energy scales, associated with both superconducting gaps, the $M_z(t)$ curves were reanalyzed due to the fact that both gaps could each have its own T_1, as nuclear spins interacting with electrons subjected to different gaps can relax at different rates. Therefore, besides Equation 5.5, two other equations were used:

$$M(t) = (1-f)\left[0.1\exp(-t/T_1)^{\beta} + 0.9\exp(-6t/T_1)^{\beta}\right] \tag{5.6}$$

which is called a **stretched fit** (β is a stretching factor), and:

$$M(t) = (1-f)\big(\left[0.1\exp(-t/T_{1S}) + 0.9\exp(-6t/T_{1S})\right] + \tag{5.7}$$

$$\left[0.1\exp(-t/T_{1L}) + 0.9\exp(-6t/T_{1L})\right]\big) \tag{5.8}$$

where T_{1S} and T_{1L} are short and long T_1 components, respectively. This accounts for two different relaxation mechanisms involved in the materials, whereas the stretched fit comes in hand when other effects (such as magnetic fluctuations) are responsible for a distribution of T_1.

In order to verify and compare such fits, instead of plotting $M_z \times t$, we opt for plotting $1 - M/M_0$, where $M_0 = M_z(t=0)$: this gives a much clearer visualization on regions of large t and M_∞ and whether the fit is actually suitable for the entire range of t or not. Two examples are seen in Figure 5.12.

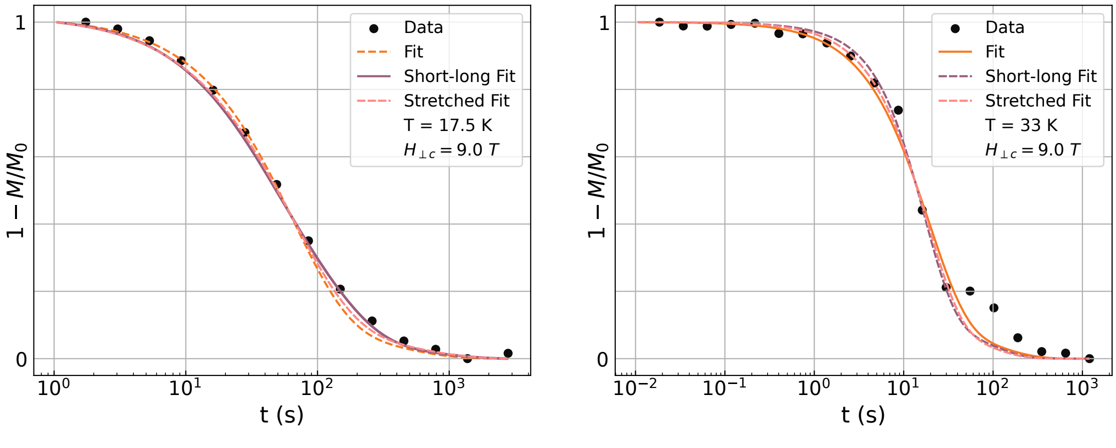

(a) (b)

Figure 5.12: $(1 - M/M_0)$ of ^{11}B for our MgB_2 single crystal at a) 17.5 K and b) 33 K. The orange line is the single-component fit, Equation 5.5; the purple, two-component fit, Equation 5.8 and the pink is the stretched fit, Equation 5.6.

For larger t, one can see in Figure 5.12a that the best fit is indeed a two-component T_1. This was observed for all $T \leq 18$ K, the critical temperature for $H = 9$ T, indicating that at this point, both SC gaps are present. Although this is a negligible difference, it is still noticeable to the point that it is not observed for higher temperatures. Note how for $T = 33$ K (Figure 5.12b), it is the single component fit that most closely fits the data points for larger t. This means that one of the superconducting gaps is not present at that temperature range, only below T_c.

Using these new fit, the new $(T_1 T)^{-1} \times T$ data are presented in Figure 5.13.

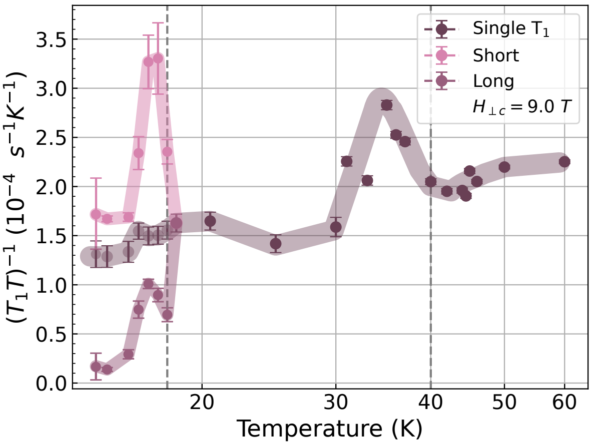

Figure 5.13: $(T_1 T)^{-1} \times T$ for ^{11}B of MgB_2, now with short and long components of T_1. $T_c = 18$ K is marked by a dashed line: for $T \leq 18$ K, a two-component fit was used (Equation 5.8), and both components are plotted, with the short component being the lightest colour and the long being the intermediate shade of purple. The darkest shade represents T_1 obtained through the single-component fit.

Furthermore, note how there is a clear peak right below 18 K for both short and long components, meaning that this is the Hebel-Slichter peak expected for BCS superconductors. On the other hand, the peak at 35 K is a peak directly related to the transition, but not a coherence Hebel-Slichter peak. In that sense, we can infer that this is a time-resolved observation of the Hebel-Slichter peak in a BCS superconductor, and the first observation of the two superconducting gaps of MgB_2 using relaxation processes.

One noteworthy aspect is that the long component of T_1 is closer to the T_1 obtained from a single-component fit than the short component. This can be understood considering that the long component is linked to the higher superconducting gap, originating from the σ bands of B, while the short component corresponds to the lower superconducting gap associated with the π bands. For the highest SC gap, $T_c = 35$ K and the BCS gap is $\Delta(0) \approx 5.31$ meV; for the lowest SC gap, $T_c = 18$ K and the BCS gap is $\Delta(0) \approx 2.73$ meV.

5.3 Partial Conclusions

For this part of the work, very intriguing results were obtained. It is exciting that this is the first observation of NMR signal of ^{11}B in MgB_2 single crystals, as there are no reported data on this phase and in this type of samples despite being a widely studied material. The fact that the Knight shift increases rather than decreases in the superconducting state is still an open question.

As for the quadrupolar frequency, $\nu_Q = 0.825(5)$ MHz is in good agreement with data already published for both single and polycrystalline samples. This means that there are no accentuated variation of the lattice parameters in the superconducting state, as expected for MgB_2.

Further measurements can be performed in the future as to completely characterize the sample, such as specific heat, WDS/EDS (Wavelength/energy-dispersive X-ray spectroscopy) and resistivity. This can shed further light in the question of contamination of the sample and its superconducting state. Besides not being in the scope of the studies of this work, which focused on NMR, they are most likely not feasible on such small samples, and therefore these experiments were not performed to further study the sample.

Lastly, this is the first observation of two peaks in the spin-lattice relaxation rates, most likely due to the two superconducting gaps σ and π. This is quite fascinating, since not all papers published on $(T_1 T)^{-1}$ have observed a coherence peak in polycrystalline samples, and this reveals that using a single crystal allows one a clearer observation of such peaks associated with both superconducting gaps. The fact that there are two components of for $T \leq 18$ K leads to the conclusion that this is the first time-resolved observation of two superconducting gaps using NMR and relaxation processes. One of the peaks observed is indeed a coherence Hebel-Slichter peak, for it happens exactly below T_c for the applied magnetic field, whereas the other peak is an indication of the opening of the higher energy SC gap (originating from the σ bands), whereas the π bands open the SC gap at T_c.

6 SUPERCONDUCTIVITY IN FE-BASED COMPOUNDS

In this Chapter, the results for the Fe-based superconductor are presented. We begin with a theoretical introduction to these compounds and their unconventional superconductivity, phase diagram and crystal structure. The first data presented are for bulk magnetization, as function of applied magnetic field and temperature. We were able to obtain the critical temperature in different magnetic fields and a superconducting hysteresis loop, as well as its critical current for a field of 4 T. For NMR data, we were able to observe the Knight shift change as the temperature lowered and could extract the critical temperature of 14 K at 10.78 T. Finally, we present our T_1 data and compared to already published results for these compounds.

6.1 Introduction

The Fe-based superconductors form an interesting set of materials that changed the scientific community views of unconventional superconductivity. First discovered by Kamihara et al in 2008 [8], the LaFeAs($O_{1-x}F_x$) has a critical temperature of 26 K. This is a remarkable discovery since Fe is a strong magnetic ion, and magnetism does not get along with superconductivity. Soon after this, more Fe-based compounds were found wil progressively higher T_c values, yielding this class of materials the title of "high T_c superconductors".

There is large evidence to this day that de Fe-based superconductors (FeSCs) are in fact unconventional, meaning the Cooper pairs are not formed through phonon interactions [18–22]. Furthermore, they defy our understanding of the Cooper pairs even in unconventional SC. Before their discovery, it was believed that Cooper pairs had non-zero angular momentum and gap nodes, which give rise to the d-wave superconductivity in cuprates [78]. However, there is strong evidence have zero angular momentum and the unconventional superconductivity arise from the different phases they take in different bands [19, 20].

In addition, the normal state of FeSC is quite unusual. The electron-electron interactions play an important role in shaping their phase diagram, and due to the multiorbital characer of these compounds, it is the Hund's interaction that possibly has the strongest role in this state [24]. Since the electronic correlation is mostly described by this interaction, this new metal, called Hund metal [25], exhibit a mixture of itinerant (conducting) and localized (strongly correlated) electron behavior. At intermediate temperatures, charge and orbital degrees of freedom seem itinerant, whereas spin degrees of freedom appear localized [79]. This same interaction is also responsible for the so called oribital differentiation:

even though different Fe orbitals are under the same interactions, they experience different degrees of correlation [25–30].

It is precisely from this Hund metal phase that superconductivity and other ordered states arise. Most FeSCs exhibit magnetic order, with $BaFe_2As_2$ exhibiting an stripe-type antiferromagnetic phase below 134 K (Figure 6.1a). In superconducting compounds, magnetic fluctuations at the stripe-order wavevectors are frequently observed. Additionally, neutron scattering reveals a resonance peak in the magnetic spectrum at this wavevector, which is interpreted as evidence for a sign-changing superconducting gap. This also points in the direction of magnetic fluctuations playing a crucial role in the pairing mechanism of superconducting electrons.

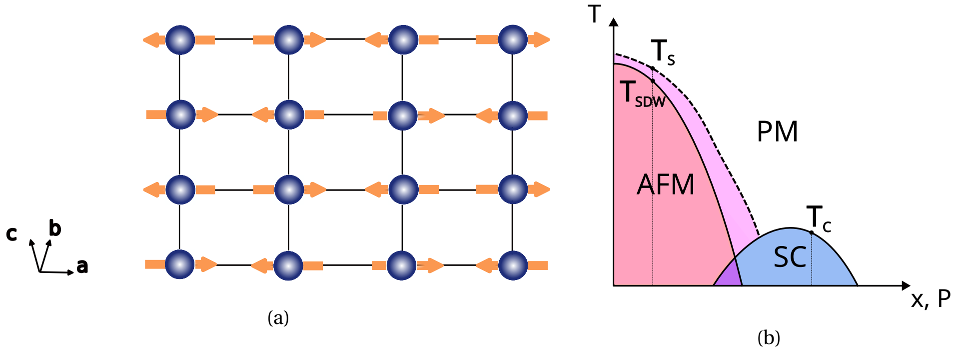

(a) (b)

Figure 6.1: a) M Single stripe-type configuration of de Fe spins, realized in most FeSCs. b) Phase diagram for most FeSC. T_S is the temperature of the tetragonal-orthorhombic transition, T_{SDW} is the temperature of the AFM transition (PM-SDW) and T_C is the critical transition (PM-SC).

The structure of these FeSCs consists of one layer of FePn, where Pn is a pnictide or a chalcogen. In this layer, the Fe^{+2} ions form a square lattice and conjugate tetrahedrally with Pn ions (see Figure 6.2). This arrange, locally, causes the Fe^{+2} ions to sense a crystalline field that can either be of tetragonal symmetry, where the orbitals t_{2g} (d_{xy}, d_{xz} and d_{yz}), are of lowest energies, or tetrahedral, where the orbitals e_g ($d_{x^2-y^2}$ and $d_{3z^2-r^2}$) possess the lowest energies. In this intermediate configuration, all five d orbitals of Fe^{+2} ($3d^6$) are relevant for the physical description of this superconductor class.

The 122 family, in particular, crystallizes in the tetragonal $ThCr_2Si_2$-type structure ($I4/mmm$) and undergoes a structural distortion closely linked to the SDW transition. Notably, this SDW phase can be driven toward a SC state through both substitution (isovalent or "electron/hole") and applied pressure, indicating that structural tuning plays a role similar to that in heavy-fermion systems. Furthermore, theoretical calculations based on a supercell approach within density functional theory (DFT) suggest that these substitutions act as chemical pressure rather than effective doping [80].

Furthermore, there is a compelling relation between the structure of these compounds and the emergence of superconductivity. As the SDW phase is suppressed due to changes in structural parameters, the 3d electrons tend to localize within the Fe-As plane, regardless of the specific transition metal substitution. When the Fe-As distances decrease,

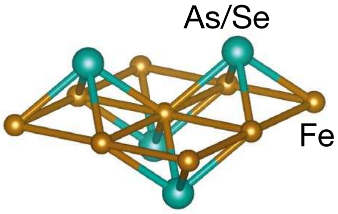

Figure 6.2: Crystal structure for 122 compound family. Figure adapted from [23].

either through chemical substitution or hydrostatic pressure, the crystal field splittings are modified, significantly enhancing the planar ($xy/x^2–y^2$) orbital character of the Fe 3d bands at the Fermi level. These effects, along with the resulting orbital differentiation, contribute to the suppression of the itinerant SDW magnetic order and the subsequent emergence of magnetically mediated superconductivity in these materials [81].

6.2 Phase Diagram of FeSC

A compelling aspect of this class of superconductors is the phase diagram they present under chemical substitution and pressure. An example is shown in Figure 6.1b. Similar to cuprates, the FeSCs also present superconductivity in the vicinity of a magnetic phase [82]. At high temperatures, they exhibit tetragonal structure and Pauli paramagnetism. On the left-most part of the diagram (low x or P), these compounds present both a structural transition to orthorrombic (with loss of C_4 symmetry) and a magnetic one when the temperature is low enough. Nowadays, this new magnetic phase is believed to be antiferromagnetic spin-density wave (SDW) type [26], where the spin density oscillates periodically as a function of space. One can see from the diagram of Figure 6.1b that superconductivity is achieved by suppressing such magnetic state [31].

Besides the structural and magnetic transitions, there is also a nematic phase arising from electron doping, in which interactions among electronic degrees of freedom break the discrete rotational symmetry without affecting the translational symmetry. Since nematic fluctuations has been observed in the phase diagram, one must ask what is the role of nematicity in these materials and its relation to superconductivity.

Thus, the proximity and coexistence [83–86] between these phases makes a compelling argument for the scientific community to believe that the superconducting pairing is mediated by spin fluctuations. It is mostly believed that the superconducting gap symmetry is given by an order parameter of type $s_\pm$ (singlet) [22, 87, 88], with inversion of signal associated with hole pockets and electrons in the Fermi surface [87] (see Figure 6.3).

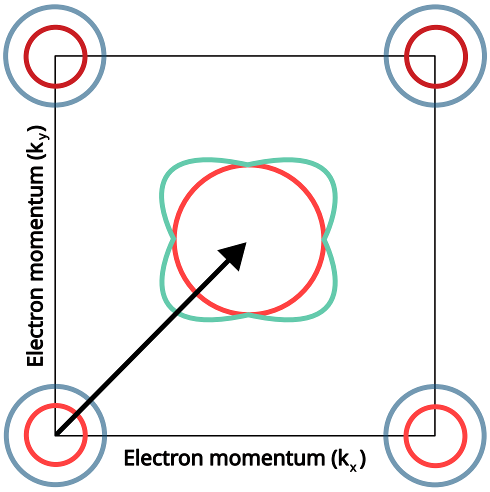

Figure 6.3: Typical Fermi surface for iron-based superconductor. The Fermi surface (projected onto k_x-k_y plane, where k is the electron moment) is calculated for LaFeAsO with 10% electronic doping, considering the tetragonal structure with one Fe atom per unit cell. In the vertices of the k_x-k_y plane are the hole pockets, whereas the electron pockets are in the center of the plane. The moment vector that connects the electron and hole pockets is represented by the black arrow. Magnetic fluctuations with this moment are predicted and experimentally observed.

6.3 Unconventional Superconductivity

The FeSCs show a wide range of critical temperatures, as shown in Figure 6.4a. The largest, $T_c \approx 65$ K is observed in monolayer of FeSe grown on $SrTiO_3$. There are undoped compounds which naturally display superconductivity, such as FeSe, LiFeAs and $CaKFe_4As_4$. For other families, such as $BaFe_2As_2$ and LaFeAsO, the magnetic and nematic orders need to be suppressed in order to achieve superconductivity, via doping, chemical substitution or pressure.

As the DFT (Dynamic Field Theory)-calculated electron-phonon coupling cannot explain the T_c observed for these compounds, an electronic mechanism has been proposed [18,21,22]. Nevertheless, this does not fully exclude the role of phonons in the pairing mechanism, as they can be enhanced by electronic correlations, as was proposed for monolayer FeSe [89]. Generally, electronic repulsion forces the gap function to change sign in real or momentum space. For multiple small Fermi pockets, as in FeSCs, the gap can remain nearly isotropic around each Fermi surface, as long as it acquires different phases (i.e., signs) on different pockets. Any gap that satisfies this criterion is referred to as $s_\pm$-wave. In FeSCs, a strong repulsive pairing interaction is believed to be promoted by magnetic correlations associated with the nearby stripe magnetic state [23].

As for the gap structures, there are many configurations possible for the $s_\pm$-wave, depending on the Fermi surface and orbital degrees of freedom. Some of these gap structures in the Fe Brillouin zone are illustrated in Figure 6.4. These are motivated by theoretical considerations and consistent with ARPES, STM and neutron scattering measurements. One question that arises in this diverse scenario, with so many different families of FeSCs and a wide range of gap structures, is whether there is a common pairing mechanism between all FeSCs. An argument in favour of that is the dimensionless ratio $2\Delta_{max}/(k_B T_c)$, where Δ_{max} is the zero-temperature value of the largest gap: this ratio is between 6.0 and 8.5 for many FeSCs, in contrast to the 3.5 - 4.5 range observed for BCS superconductors (Figure 6.5).

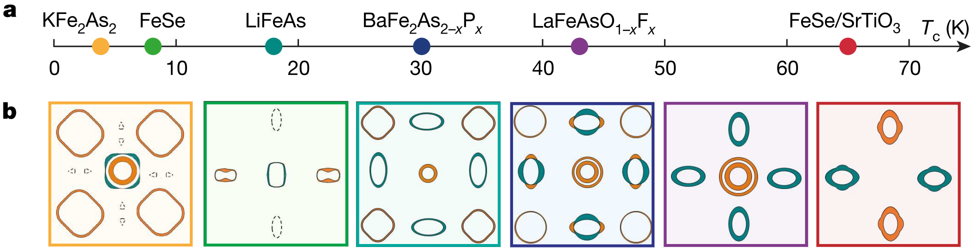

Figure 6.4: a) Superconducting critical temperatures, Tc, of six canonical Fe-based superconductors. b)Schematic gap structures for Fe-based superconductors in the 1-Fe Brillouin zone (borders coloured according to **a)**) based on weak-coupling calculations, ARPES and STM experiments. The line thickness represents the magnitude of the gap, and the different colours denote different signs. Figure adapted from [23].

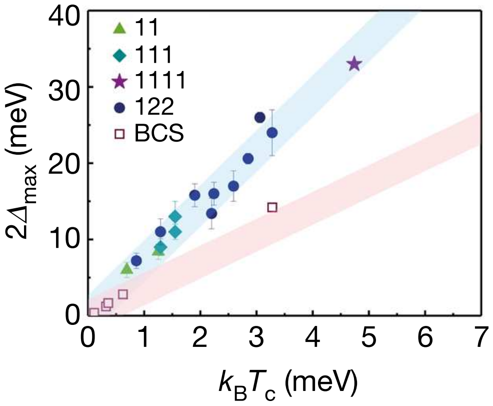

Figure 6.5: Ratio between $2\Delta_{max}$, based on ARPES data, and $k_b T_c$ of FeSCs compared with that of conventional superconductors. Figure adapted from [23].

6.4 Results and Discussions

For this part of the project, the chosen sample was $BaFe_{1.91}Co_{0.09}As_2$, an optimally doped superconductor. It is expected to completely suppress the magnetic ordering state and provide a direct transition between normal and superconducting states. The single crystals were grown using solid state techniques with In flux, where there is no incorporation of In to the crystal.

The same procedure as MgB_2 was adopted: first, a bulk magnetization experiment was performed to calculate its T_c for higher magnetic fields, as well as to observe the magnetic hysteresis typical of superconductors when cycling through different intensities of magnetic field.

6.4.1 Magnetization experiments

The results for FeSC single crystals is in Figure 6.6. In Figure 6.6a, one can see that, for H ⊥ c = 25 Oe, there is a strong diamagnetic response, which persists for H ⊥ c = 7 T (Figure 6.6b). This is a good indication that the sample is becoming indeed superconducting at low temperatures. From the onset of superconductivity, one can extract the critical temperatures of 26 K and 22 K, respectively. The T_c for zero field is in good agreement with data already published [90].

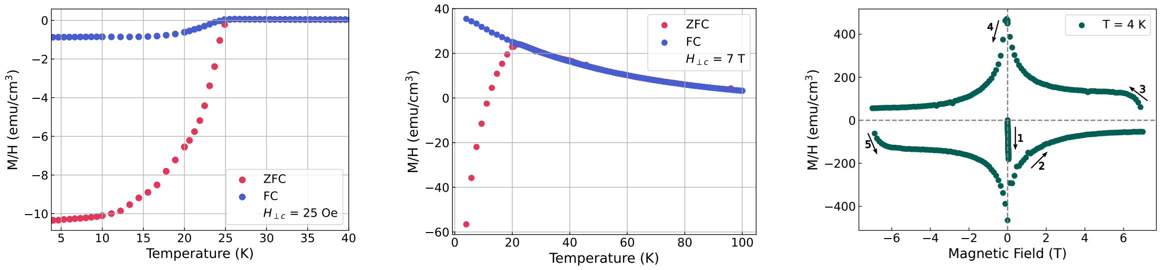

(a)

(b)

(c)

Figure 6.6: Magnetization as function of temperature for applied magnetic field a) 25 Oe and b) 7 T. c) Magnetization as function of applied magnetic field at 4 K. The arrows indicate the sequence of the magnetic field application.

Moreover, the superconducting hysteresis loop in seen clearly in Figure 6.6c: as the magnetic field first increases and $T < T_c$, there is a strong diamagnetic response to it, which peaks at $H_{c1} \approx 600$ Oe. Above this intensity of magnetic field, the sample is in its mixed phase, thus the magnetic field is able to penetrate it in the form of quantum flux vortice. The higher the magnetic field, the bigger the vortice become, so that the normal state regions increase and the superconducting regions decrease, which decreases the diamagnetic response seen by the magnetic moments. This happens until $H = H_{c2}$, where superconductivity is broken and the sample is completely in the normal state. This is not observed here because the maximum magnetic field (7 T) is much smaller than the H_{c2} for this sample, which is around 40 T for iron-arsenide compounds.

By performing the sequence of 0 T → 7 T → 0 T → - 7 T → 0 T, it is clear that the magnetic moments are not zero by the end of it. Instead, they are quite large in intensity. This happens due to flux pinning, caused by imperfections in the sample that act as pinning centers for vortices. Therefore, even if the magnetic field is again zero, there is still some remanant magnetization.

Moreover, one can calculate the supercurrent density using the Bean's formula [91]:

$$J_c = \frac{2\Delta M}{w\left(1 - \frac{w}{3b}\right)} \tag{6.1}$$

where ΔM is the difference in magnetization for the same magnetic field and w and b are the width and base of a parallelepiped [92]. For our sample, and H = 4 T, the supercurrent density is $J_c \approx 60,9\ \mathrm{A/cm^2}$.

6.4.2 NMR experiments

For NMR experiments, the choice of H_0 was of 10.78 T ($\nu \approx 78.95$ MHz), which is intermediate between H_{c1} and H_{c2}, thus allowing us to probe the mixed phase of this superconductor. Spin echo sequences were performed in temperatures spanning from 4.5 K to 40 K in order to observe both the line broadening and the frequency shift of the central line. Such results are in Figure 6.7. The resonance peaks were fit using a Lorentzian function (Equation 5.4).

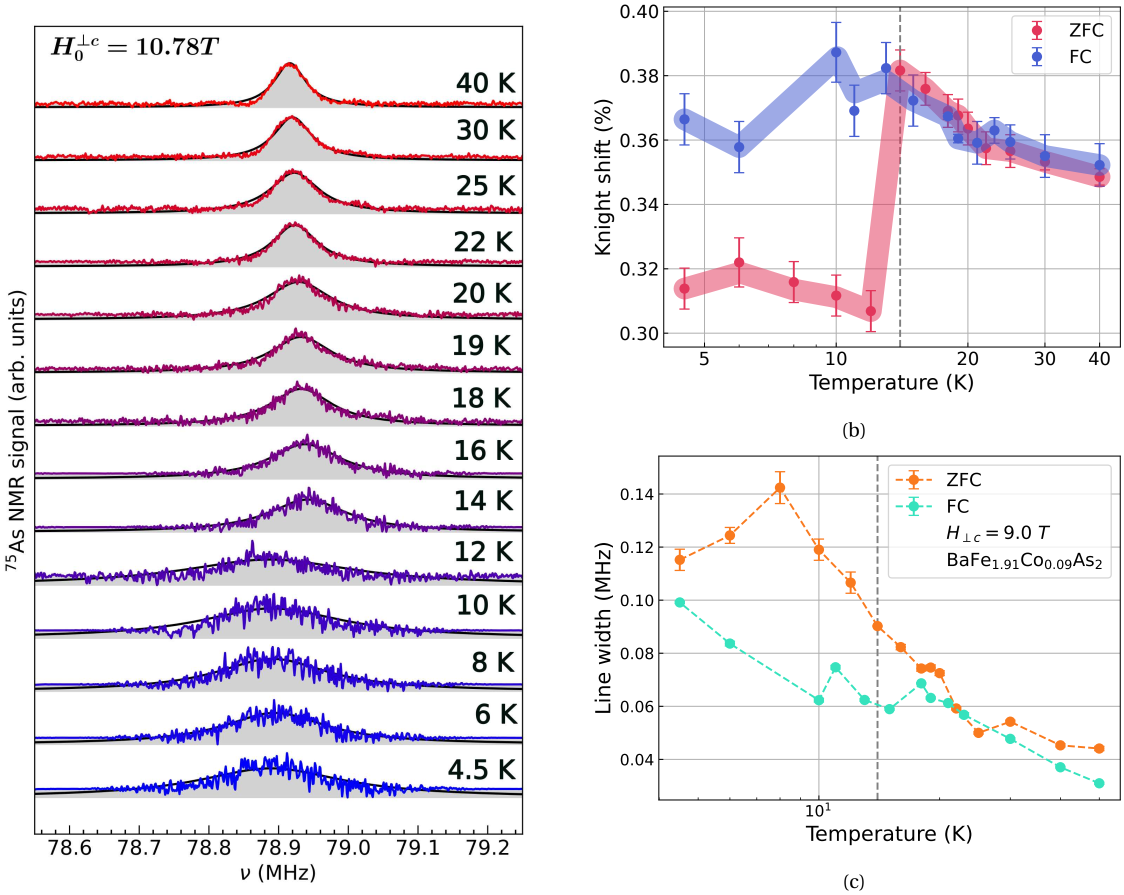

(b)

(c)

(a)

Figure 6.7: a) Central line Knight shift (ZFC), at $H_0^{\perp c} = 10.78$ T, from 4.5 K to 40 K for $BaFe_{1.91}Co_{0.09}As_2$. The black line is a Lorentzian fit, whereas the coloured lines are the NMR data. b) Knight shift K as a function of temperature. The dashed line marks the onset of superconductivity. c) Line broadening, where the line width is the parameter w in Equation 5.4.

From Figures 6.7a and 6.7c, the broadening of line due to the quantum flux vortices is clear: the full width at half maximum at 40 K is 37.04(3) kHz, whereas it is 99.1(4) kHz at 4.5 K. Moreover, the clear shift in frequency was observed: whereas in normal state, the resonance frequency is $\nu = 78.9868(2)$ MHz, is it $\nu = 78.885(2)$ MHz in the mixed state.

This extreme line broadening near and below 20 K could also reveal a coexistence between antiferromagnetic and superconducting states. Although it is not expected for this Co doping level, it has already been reported for a slightly higher doping, [93], and this NMR study reveals similar observations as our study. This overall broadening of all transitions can be attributed to an incommensurate SDW phase, where the periodicity of the spin-density wave does not match that of the lattice. This is in contrast to what happens in the parent compound $\mathrm{BaFe_2As_2}$, where commensurate SDW presents itself through NMR by two very distinct and narrow lines.

Furthermore, the line broadens in a homogeneous fashion, which points to the fact that frozen moments develop on all Fe atoms of the sample. Had it developed only in a fraction of these atoms, the line shape would rather be a narrow peak surrounded by a broad line distribution.

The coexistance of incommensurate SDW and SC can be understood in an itinerant picture. In the parent compound, the commensurate nesting between electron and hole pockets leads to a commensurate SDW order. When doping with Co (electron doping), one increases the size of the electronic pockets, thus deteriorating the nesting and decreasing T_{SDW} and the moments, which leads to icommensurability. At intermediate dopings, Vorontsov *et al.* proved that this SDW may coexist with SC if T_{SDW}/T_c is rather large and if SDW is incommensurate [94]. This is further supported by the fact that the hole doped $\mathrm{Ba_{1-x}K_xFe_2As_2}$ does not display coexistence and smaller T_{SDW}/T_c ratio.

Furthermore, the Knight shift was calculated using Equation 5.3, and its plot as a function of temperature can be seen in Figure 6.7b. From the onset of superconductivity, it can be seen that $T_c = 14$ K. The shift towards lower frequencies is the expected behavior for a superconductor, since the Knight shift is proportional to the spin susceptibility by a factor A_{hf}, which is the hyperfine coupling and the susceptibility lowers below T_c (see Figure **??**).

Lastly, the results for spin-lattice relaxation rate $(T_1T)^{-1}$ are in Figure 6.8a. The values above T_c are relatively close, and at T = 13 K the value of $(T_1T)^{-1}$ is smaller than the others. It is expected for there to be a peak exactly at T_c due to the transition, but not below it, since this is an unconventional superconductor. Naturally, for this analysis, more data need to be acquired around this temperature.

The values found for $(T_1T)^{-1}$ are on average five times smaller than values already published for this level of Co doping [93, 95]. What was also observed in Ref. [93] (Figure 6.8b) is an increase at T ~ 31 K of $(T_1T)^{-1}$, forming a broad peak around this temperature due to the SDW transition. This was not observed in our data for T ~ 31 K, but rather at 40 K. Moreover, a peak just below T_c was observed in Ref. [93] which is also not the case for our data: the only data point below T_c ($T = 13K$) is smaller than the points just above it. By com-

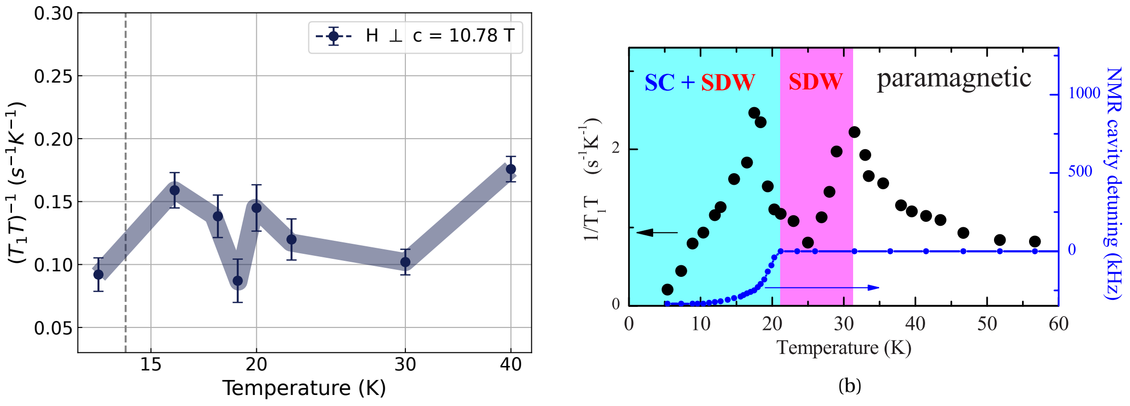

(a)

(b)

Figure 6.8: a) Spin-lattice relaxation rate $(T_1T)^{-1}$ as a function of temperature. The dashed line marks the estimated T_c obtained through Knight shift data. b) $1/(T_1T)$ measured for H||ab (left axis) shows two peaks at both SC and SDW transitions, while detuning of the NMR cavity (right axis) demonstrates the apparition of SC. Figure extracted from Ref. [93].

paring to our data, one could say the SDW transition observed in Ref. [93] at 30 K is the same we observed at 20 K, and the SDW + SC transition at 17 K is also observed in our data at 16 K. The lowest point between these two temperatures, in our data, is at 19 K, whereas in Ref. [93] it is at 25 K. The difference in these temperatures can be explained by different actual doping levels of Co in our samples.

Another set of $(T_1T)^{-1}$ for this level of doping is published in Ref. [95]. They have not observed any peaks above T_c, instead $(T_1T)^{-1}$ increases monotonically as T lowers ($T > T_c$) in the same temperature range as our experiment. This increase is not observed in our data.

It is worth mentioning that for this sample, it was necessary to fit it with another function for $M_z(t)$, Equation 5.6. The difference between this and the function used for MgB_2 (Equation 5.5) is that an exponent β is now present; this is called a stretched fit. This means that T_1 for this sample is not single component, but rather it has a distribution of values for the same temperature. The factor β accounts for this distribution. One can see a comparison between non-stretched ($\beta = 1$) and stretched ($\beta \neq 1$) fits in Figure 6.9.

An interesting feature of such factor is the fact that it showed a dependency on temperature (see Figure 6.10). Around 20 K, the NMR line lost most of its intensity and became broader as well, and it's around this temperature that β also starts to increase, meaning this could be another indication of the SDW phase present in this sample, besides the increase in $(T_1T)^{-1}$ observed in Figure 6.8a. The lowest value for β is also at 19 K, as it is for $(T_1T)^{-1}$. Furthermore, the increase in β below 19 K points towards the presence of the superconducting transition, as well as the SDW phase. Thus, one can assume that, at this level of Co doping, there is a coexistence of superconductivity and spin-density wave phases.

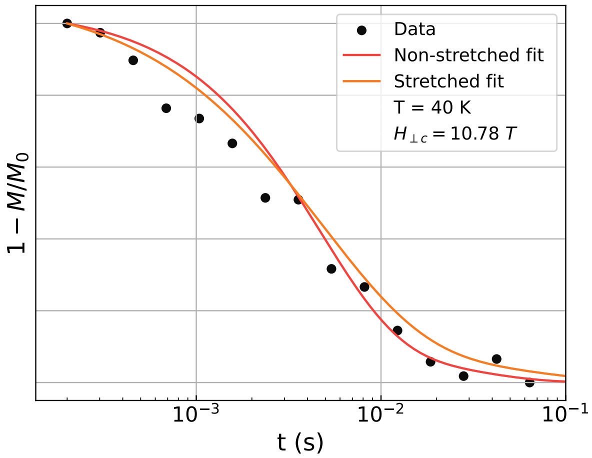

Figure 6.9: Comparison between a non stretched fit (using Equation 5.5) and a stretched fit (using Equation 5.6). The latter fits better on the region for smaller t.

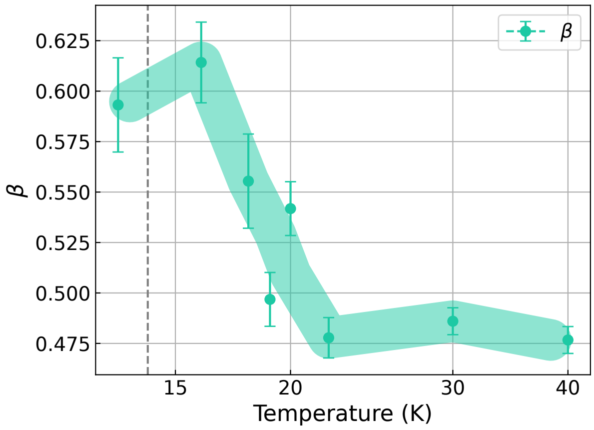

Figure 6.10: β stretching factor as a function of temperature. The dashed line marks the estimated critical temperature of 14 K for $H_0 = 10.78$ T.

6.5 Partial Conclusions

For this part of the thesis, we obtained in general expected results for a superconductor, both in magnetization and in NMR experiments. First of all, we could get a well-defined T_c in magnetization experiments, indicating the presence of the diamagnetic shielding characteristic of superconductor. There was also a hysteresis loop in the M *vs.* H experiments, consistent with the superconducting hysteresis loop.

Moreover, from the spectral analysis in NMR experiments, the superconducting transition was observed through the Knight shift behaviour in lower temperatures. A signature aspect of such state is the broadening of the NMR line due to the quantum vortice lattice in the mixed phase, which was also present in our set of results. As for the Knight shift, since $K \propto \chi_{\text{spin}}$, the same behavior of K was observed for the magnetization as a function of temperature, and from that and the onset of superconductivity, we could estimate $T_c \approx 14$ K.

Finally, from the spin-lattice relaxation rate data, although more data points would be necessary, one can see that two peaks were observed, just as it was reported in Ref. [93]

for a quite similar doping level. The both peaks indicating a SDW transition as well as a SDW+SC state matches our observations from Knight shift and $(T_1 T)^{-1}$: the SDW transition starts at ≈ 20 K, observed from the extreme broadening and the loss of features from the NMR line. This is where the first peak in $(T_1 T)^{-1}$ happens. Moreover, a decrease in $(T_1 T)^{-1}$ at 19 K matches the one observed in 25 K in Ref. [93]. Below this temperature, another peak is observed at 16 K (and 17 K for Ref. [93]) which marks the onset of superconductivity and, therefore, the coexistence of SC and SDW below this temperature. Such observations are consistent with the behaviour of the stretching factor β, indicating the presence of an antiferromagnetic phase.

7 CONCLUSION AND FUTURE PERSPECTIVES

As for general conclusions of this work, the past two years were quite productive and enlightened me in the use of NMR for studying superconductors. In spite of using different type of superconductors in my studies, some similarities have been observed using NMR: changes in the NMR resonance line due to the superconducting state, such as change in the Knight shift and line broadening due to the diamagnetic shielding. One can also estimate T_c throught the onset of superconductivity using Knight shift data as function of temperature.

Some of the differences between both superconductors is the absence of coherence peaks in $(T_1 T)^{-1}$ data for an unconventional superconductor. The most striking difference is that, for MgB_2, T_1 was found to be quite long and single component ($\beta = 1$), whereas for $BaFe_{1.91}Co_{0.09}As_2$, a stretched magnetization recovery behavior was discovered even in the normal state, indicating a distribution of T_1 given by β, a signature of inhomogeneity. This multicomponent aspect of T_1 may indicate magnetic fluctuations associated with the SDW phase.

As for future perspectives, some further experiments could be performed. For instance, in order to confirm the origin of the two anomalies observed in spin-lattice relaxation data, one could measure the specific heat of MgB_2 single crystals to compare both data. As for the contamination hypothesis, due to the discrepancy observed in expected magnetization behaviour, this could be verified by XRD or WDS experiments. What makes these experiments unfeasible is the micro size of the samples, which might not provide enough response to the equipments if one uses only one single crystal.

Naturally, more data would be needed for spin-lattice relaxation rate for Co-doped FeSC in order to verify the observed peaks and the absence of the Hebel-Slichter peak below T_c. However, the extreme line broadening below 20 K (a wipe-out effect probably associated with faster T_2) made it impossible to acquire T_1 data at this temperature range. This suggests that strong magnetic fluctuations must remain even in the optimally doped $BaFe_2As_2$.

BIBLIOGRAPHY

[1] Kamerlingh Onnes, H. The resistance of pure mercury at helium temperatures. *Commun. Phys. Lab. Univ. Leiden, b* **120** (1911).

[2] Meissner, W. & Ochsenfeld, R. Ein neuer effekt bei eintritt der supraleitfähigkeit. *Naturwissenschaften* **21**, 787–788 (1933).

[3] London, H. & London, F. The electromagnetic equations of the supraconductor. *Proceedings of the Royal Society A* **149**, 71–88 (1935).

[4] Ginzburg, V. & Landau, L. On the theory of superconductivity. *Zhurnal Eksperimentalnoi i Teoreticheskoi Fiziki* **20** (1950).

[5] Bardeen, J., Cooper, L. N. & Schrieffer, J. R. Microscopic theory of superconductivity. *Phys. Rev.* **106**, 162–164 (1957).

[6] Steglich, F. *et al.* Superconductivity in the presence of strong Pauli paramagnetism: $CeCu_2Si_2$. *Physical Review Letters* **43**, 1892 (1979).

[7] Bednorz, J. G. & Müller, K. A. Possible high T_c superconductivity in the Ba-La-Cu-O system. *Zeitschrift für Physik B Condensed Matter* **64**, 189–193 (1986).

[8] Kamihara, Y., Watanabe, T., Hirano, M. & Hosono, H. Iron-based layered superconductor $La[O_{1-x}F_x]FeAs$ (x= 0.05-0.12) with T_c= 26 K. *Journal of the American Chemical Society* **130**, 3296–3297 (2008).

[9] Schilling, A., Cantoni, M., Guo, J. & Ott, H. Superconductivity above 130 k in the hg–ba–ca–cu–o system. *Nature* **363**, 56–58 (1993).

[10] Drozdov, A. *et al.* Superconductivity at 250 k in lanthanum hydride under high pressures. *Nature* **569**, 528–531 (2019).

[11] Bud'ko, S. L. *et al.* Boron isotope effect in superconducting MgB_2. *Physical Review Letters* **86**, 1877 (2001).

[12] Hinks, D., Claus, H. & Jorgensen, J. The complex nature of superconductivity in MgB_2 as revealed by the reduced total isotope effect. *Nature* **411**, 457–460 (2001).

[13] Takahashi, T., Sato, T., Souma, S., Muranaka, T. & Akimitsu, J. High-resolution photoemission study of MgB_2. *Physical review letters* **86**, 4915 (2001).

[14] Karapetrov, G., Iavarone, M., Kwok, W., Crabtree, G. & Hinks, D. Scanning tunneling spectroscopy in MgB_2. *Physical review letters* **86**, 4374 (2001).

[15] Osborn, R., Goremychkin, E., Kolesnikov, A. & Hinks, D. Phonon density of states in MgB_2. *Physical Review Letters* **87**, 017005 (2001).

[16] Canfield, P. C. & Crabtree, G. W. Magnesium diboride: better late than never. *Physics Today* **56**, 34–40 (2003).

[17] Karpinski, J. *et al.* MgB_2 single crystals: high pressure growth and physical properties. *Superconductor Science and Technology* **16**, 221 (2003).

[18] Wang, F. & Lee, D.-H. The electron-pairing mechanism of iron-based superconductors. *Science* **332**, 200–204 (2011).

[19] Mazin, I., Singh, D. J., Johannes, M. & Du, M.-H. Unconventional superconductivity with a sign reversal in the order parameter of $LaFeAsO_{1-x}F_x$. *Physical Review Letters* **101**, 057003 (2008).

[20] Kuroki, K., Usui, H., Onari, S., Arita, R. & Aoki, H. Pnictogen height as a possible switch between high-T_c nodeless and low-T_c nodal pairings in the iron-based superconductors. *Physical Review B—Condensed Matter and Materials Physics* **79**, 224511 (2009).

[21] Hirschfeld, P., Korshunov, M. & Mazin, I. Gap symmetry and structure of Fe-based superconductors. *Reports on progress in physics* **74**, 124508 (2011).

[22] Chubukov, A. Pairing mechanism in Fe-based superconductors. *Annu. Rev. Condens. Matter Phys.* **3**, 57–92 (2012).

[23] Fernandes, R. M. *et al.* Iron pnictides and chalcogenides: a new paradigm for superconductivity. *Nature* **601**, 35–44 (2022).

[24] Haule, K. & Kotliar, G. Coherence-incoherence crossover in the normal state of iron oxypnictides and importance of hund's rule coupling. *New journal of physics* **11**, 025021 (2009).

[25] Yin, Z., Haule, K. & Kotliar, G. Kinetic frustration and the nature of the magnetic and paramagnetic states in iron pnictides and iron chalcogenides. *Nature materials* **10**, 932–935 (2011).

[26] de'Medici, L., Hassan, S. R., Capone, M. & Dai, X. Orbital-selective Mott transition out of band degeneracy lifting. *Physical review letters* **102**, 126401 (2009).

[27] Bascones, E., Valenzuela, B. & Calderon, M. J. Orbital differentiation and the role of orbital ordering in the magnetic state of Fe superconductors. *Physical Review B—Condensed Matter and Materials Physics* **86**, 174508 (2012).

[28] Yu, R. & Si, Q. Orbital-selective Mott phase in multiorbital models for alkaline iron selenides $K_{1-x}Fe_{2-y}Se_2$. *Physical Review Letters* **110**, 146402 (2013).

[29] de'Medici, L., Giovannetti, G. & Capone, M. Selective Mott physics as a key to iron superconductors. *Physical review letters* **112**, 177001 (2014).

[30] Georges, A., Medici, L. d. & Mravlje, J. Strong correlations from Hund's coupling. *Annu. Rev. Condens. Matter Phys.* **4**, 137–178 (2013).

[31] Paglione, J. & Greene, R. L. High-temperature superconductivity in iron-based materials. *Nature physics* **6**, 645–658 (2010).

[32] Maxwell, E. Isotope effect in the superconductivity of mercury. *Phys. Rev.* **78**, 477–477 (1950).

[33] Reynolds, C. A., Serin, B., Wright, W. H. & Nesbitt, L. B. Superconductivity of isotopes of mercury. *Phys. Rev.* **78**, 487–487 (1950).

[34] Abrikosov, A. A. The magnetic properties of sperconducting alloys. *Journal of Physics and Chemistry of Solids* **2**, 199–208. (1957).

[35] Slichter, C. P. Magnetic resonance and superconductivity: Some history, ancient and in the making. *Journal of superconductivity and novel magnetism* **19**, 159–166 (2006).

[36] Stromberg, T. & Swenson, C. Negative surface free-energy effects in superconducting niobium. *Physical Review Letters* **9**, 370 (1962).

[37] Swartz, P. S. Evidence for the negative surface energy models of superconductivity in Nb_3Sn, Nb_3Al, V_3Ga, and V_3Si. *Physical Review Letters* **9**, 448 (1962).

[38] Curro, N., Milling, C., Haase, J. & Slichter, C. Local-field dependence of the ^{17}O spin-lattice relaxation and echo decay rates in the mixed state of $YBa_2Cu_3O_7$. *Physical Review B* **62**, 3473 (2000).

[39] Kakuyanagi, K., Kumagai, K.-i., Matsuda, Y. & Hasegawa, M. Antiferromagnetic vortex core in $Tl_2Ba_2CuO_{6+\delta}$ studied by nuclear magnetic resonance. *Physical review letters* **90**, 197003 (2003).

[40] Scalapino, D. J. The case for $d_{x^2-y^2}$ pairing in the cuprate superconductors. *Physics Reports* **250**, 329–365 (1995).

[41] Knight, W. D. Nuclear magnetic resonance shift in metals. *Physical Review* **76**, 1259 (1949).

[42] Leggett, A. J. A theoretical description of the new phases of liquid ^3He. *Reviews of Modern Physics* **47**, 331 (1975).

[43] Curro, N. *et al.* Unconventional superconductivity in PuCoGa$_5$. *Nature* **434**, 622–625 (2005).

[44] Tinkham, M. *Introduction to Superconductivity*. International series in pure and applied physics (McGraw-Hill, Inc., 1996).

[45] London, F. *Superfluids: Microscopic theory of superconductivity*, vol. 1 (Wiley, 1950).

[46] Fröhlich, H. Theory of the superconducting state. I. the ground state at the absolute zero of temperature. *Physical Review* **79**, 845 (1950).

[47] Mahan, G. D. *Many-particle physics* (Springer Science & Business Media, 2013).

[48] Cooper, L. N. Bound electron pairs in a degenerate fermi gas. *Phys. Rev.* **104**, 1189–1190 (1956).

[49] Slichter, C. P. *Principles of magnetic resonance*, vol. 1 (Springer Science & Business Media, 2013).

[50] Rabi, I. I., Zacharias, J. R., Millman, S. & Kusch, P. A new method of measuring nuclear magnetic moment. *Physical review* **53**, 318 (1938).

[51] Bloch, F. Nuclear induction. *Physical review* **70**, 460 (1946).

[52] Purcell, E. M., Torrey, H. C. & Pound, R. V. Resonance absorption by nuclear magnetic moments in a solid. *Physical review* **69**, 37 (1946).

[53] Hahn, E. L. Spin echoes. *Physical review* **80**, 580 (1950).

[54] Carr, H. Y. & Purcell, E. M. Effects of diffusion on free precession in nuclear magnetic resonance experiments. *Physical review* **94**, 630 (1954).

[55] Keeler, J. Understanding nmr spectroscopy. URL `http://www-keeler.ch.cam.ac.uk/lectures/Irvine/`.

[56] Suhl, H., Matthias, B. & Walker, L. Bardeen-cooper-schrieffer theory of superconductivity in the case of overlapping bands. *Physical Review Letters* **3**, 552 (1959).

[57] Choi, H. J., Roundy, D., Sun, H., Cohen, M. L. & Louie, S. G. The origin of the anomalous superconducting properties of MgB$_2$. *Nature* **418**, 758–760 (2002).

[58] Iavarone, M. *et al.* Two-band superconductivity in MgB$_2$. *Physical review letters* **89**, 187002 (2002).

[59] Xi, X. Two-band superconductor magnesium diboride. *Reports on Progress in Physics* **71**, 116501 (2008).

[60] Kortus, J., Mazin, I., Belashchenko, K. D., Antropov, V. P. & Boyer, L. Superconductivity of metallic boron in MgB_2. *Physical Review Letters* **86**, 4656 (2001).

[61] Wang, Y., Plackowski, T. & Junod, A. Specific heat in the superconducting and normal state (2-300 k, 0-16 t), and magnetic susceptibility of the 38 k superconductor MgB_2: evidence for a multicomponent gap. *Physica C: Superconductivity* **355**, 179–193 (2001).

[62] Chen, X., Konstantinović, M., Irwin, J., Lawrie, D. & Franck, J. Evidence for two superconducting gaps in MgB_2. *Physical review letters* **87**, 157002 (2001).

[63] Tsuda, S. *et al.* Evidence for a multiple superconducting gap in MgB_2 from high-resolution photoemission spectroscopy. *Physical review letters* **87**, 177006 (2001).

[64] Giubileo, F. *et al.* Two-gap state density in MgB_2: a true bulk property or a proximity effect? *Physical review letters* **87**, 177008 (2001).

[65] Nagamatsu, J., Nakagawa, N., Muranaka, T., Zenitani, Y. & Akimitsu, J. Superconductivity at 39 k in magnesium diboride. *nature* **410**, 63–64 (2001).

[66] Zehetmayer, M. *et al.* Mixed-state properties of superconducting MgB_2 single crystals. *Physical Review B* **66**, 052505 (2002).

[67] Strässle, S., Roos, J., Mali, M., Keller, H. & Karpinski, J. ^{11}B NMR study of single-crystal MgB_2 in the normal conducting phase. *Physica C: Superconductivity* **466**, 168–173 (2007).

[68] Lee, K., Kang, K., Mean, B., Lee, M. & Cho, B. Penetration depth and Hc_2 anisotropy of MgB_2 by ^{11}B NMR. *Journal of magnetism and magnetic materials* **272**, 165–166 (2004).

[69] Gerashenko, A. *et al.* Electronic states of boron in superconducting MgB_2 studied by ^{11}B NMR. *Applied Magnetic Resonance* **21**, 157–163 (2001).

[70] Yamaji, T., Murakami, M., Fukazawa, J., Shimizu, T. & Takegoshi, K. Analysis of ^{11}B NMR powder lineshape of MgB_2 in the normal conductive phase. *Journal of the Physical Society of Japan* **77**, 044711 (2008).

[71] Baek, S. *et al.* NMR spectroscopy of the normal and superconducting states of MgB_2 and comparison to $AlgB_2$. *Physical Review B* **66**, 104510 (2002).

[72] Papavassiliou, G., Pissas, M., Fardis, M., Karayanni, M. & Christides, C. ^{11}B NMR detection of the magnetic field distribution in the mixed superconducting state of MgB_2. *Physical Review B* **65**, 012510 (2001).

[73] Buzea, C. & Yamashita, T. Review of the superconducting properties of mgb_2. *Superconductor Science and Technology* **14**, R115 (2001).

[74] Andrew, E. & Tunstall, D. Spin-lattice relaxation in imperfect cubic crystals and in non-cubic crystals. *Proceedings of the Physical Society* **78**, 1 (1961).

[75] Kotegawa, H., Ishida, K., Kitaoka, Y., Muranaka, T. & Akimitsu, J. Evidence for strong-coupling s-wave superconductivity in MgB_2: ^{11}B NMR study. *Physical Review Letters* **87**, 127001 (2001).

[76] Jung, J. *et al.* ^{11}B NMR and relaxation in the MgB_2 superconductor. *Physical Review B* **64**, 012514 (2001).

[77] Pickett, W. Mind the double gap. *Nature* **418**, 733–734 (2002).

[78] Keimer, B., Kivelson, S. A., Norman, M. R., Uchida, S. & Zaanen, J. From quantum matter to high-temperature superconductivity in copper oxides. *Nature* **518**, 179–186 (2015).

[79] Stadler, K., Yin, Z., Von Delft, J., Kotliar, G. & Weichselbaum, A. Dynamical mean-field theory plus numerical renormalization-group study of spin-orbital separation in a three-band Hund metal. *Physical review letters* **115**, 136401 (2015).

[80] Wadati, H., Elfimov, I. & Sawatzky, G. Where are the extra d electrons in transition-metal-substituted iron pnictides? *Physical review letters* **105**, 157004 (2010).

[81] Rosa, P. *et al.* Site specific spin dynamics in bafe 2 as 2. In *APS March Meeting Abstracts*, vol. 2014, C1–098 (2014).

[82] Maple, M. B. High-temperature superconductivity. *Journal of Magnetism and Magnetic Materials* **177**, 18–30 (1998).

[83] Christianson, A. D. *et al.* Static and dynamic magnetism in underdoped superconductor $BaFe_{1.92}Co_{0.08}As_2$. *Physical review letters* **103**, 087002 (2009).

[84] Pratt, D. *et al.* Coexistence of competing antiferromagnetic and superconducting phases in the underdoped $Ba(Fe_{0.953}Co_{0.047})_2As_2$ compound using X-ray and neutron scattering techniques. *Physical Review Letters* **103**, 087001 (2009).

[85] Zhang, Q. *et al.* Neutron-scattering measurements of spin excitations in LaFeAsO and $Ba(Fe_{0.953}Co_{0.047})_2As_2$: Evidence for a sharp enhancement of spin fluctuations by nematic order. *Physical review letters* **114**, 057001 (2015).

[86] Wang, M. *et al.* Magnetic field effect on static antiferromagnetic order and spin excitations in the underdoped iron arsenide superconductor $BaFe_{1.92}Ni_{0.08}As_2$. *Physical Review B—Condensed Matter and Materials Physics* **83**, 094516 (2011).

[87] Mazin, I. & Schmalian, J. Pairing symmetry and pairing state in ferropnictides: Theoretical overview. *Physica C: Superconductivity* **469**, 614–627 (2009).

[88] Bang, Y. & Stewart, G. Superconducting properties of the s±-wave state: Fe-based superconductors. *Journal of Physics: Condensed Matter* **29**, 123003 (2017).

[89] Lee, J. *et al.* Interfacial mode coupling as the origin of the enhancement of T_c in FeSe films on $SrTiO_3$. *Nature* **515**, 245–248 (2014).

[90] Garitezi, T. M. *et al.* Synthesis and characterization of $BaFe_2As_2$ single crystals grown by In-flux technique. *Brazilian journal of physics* **43**, 223–229 (2013).

[91] Bean, C. P. Magnetization of hard superconductors. *Physical review letters* **8**, 250 (1962).

[92] Poole, C. P., Farach, H. A., Creswick, R. J. & Prozorov, R. *Superconductivity* (Elsevier, 2014).

[93] Laplace, Y., Bobroff, J., Rullier-Albenque, F., Colson, D. & Forget, A. Atomic coexistence of superconductivity and incommensurate magnetic order in the pnictide $Ba(Fe_{1-x}Co_x)_2As_2$. *Physical Review B—Condensed Matter and Materials Physics* **80**, 140501 (2009).

[94] Vorontsov, A., Vavilov, M. & Chubukov, A. Interplay between magnetism and superconductivity in the iron pnictides. *Physical Review B—Condensed Matter and Materials Physics* **79**, 060508 (2009).

[95] Ning, F. *et al.* Contrasting spin dynamics between underdoped and overdoped $Ba(Fe_{1-x}Co_x)_2As_2$. *Physical review letters* **104**, 037001 (2010).